ABSTRACT

Title of dissertation: TOWARDS SHOT NOISE-LIMITED
                           DETECTION OF A
                           SINGLE-ELECTRON TRANSISTOR

                           Benedetta Camarota
                           Doctor of Philosophy, 2007

Dissertation directed by: Professor Keith C. Schwab
                           Adjunct Professor, Physics Dept., UMD
                           and
                           Associate Professor, Cornell University

A Single-Electron Transistor (SET) is a highly sensitive charge amplifier based

on the Coulomb blockade that can operate near the quantum limit: amplification

can be accomplished with a back-action close to that required by the uncertainty

principle.

Its charge sensitivity is ultimately limited to about $1\mu e/\sqrt{Hz}$ by the shot noise in

the source-drain current. Despite the fact that such sensitivity has been approached

by some, the shot-noise limit has yet to be reached for either the SET and its RF

version, the RF-SET.

A scheme is proposed and realized in this thesis for the shot noise-limited detection

of a Single-Electron Transistor, based on a DC-SQUID impedance-matched with a

DC-biased SET. SQUIDs can operate at the quantum limit, and a microstrip SQUID

amplifier has already been demonstrated to operate at almost twice the quantum-

limited noise temperature at about 500MHz by M. Muck and collaborators, with a sensitivity sufficient to resolve the SET shot noise.

The device has been fabricated and characterized. A $50K\Omega$ resistor has been used as a noise source at low temperature and the measured noise levels have been estimated.

Moreover, the detection noise temperature of $T_N \approx 110mK$ was derived corresponding to a current sensitivity of about $8fA/\sqrt{Hz}$ for the detection of a $100K\Omega$ resistor.

TOWARDS SHOT NOISE-LIMTED DETECTION OF A SINGLE ELECTRON TRANSISTOR

by

Benedetta Camarota

Dissertation submitted to the Faculty of the Graduate School of the
University of Maryland, College Park in partial fulfillment
of the requirements for the degree of
Doctor of Philosophy
2007

Advisory Committee:
Professor James R. Anderson, Chair
Professor Keith C. Schwab, Co-Chair
Professor Alex J. Dragt
Professor Luis A. Orozco
Professor Raymond J. Phaneuf
Professor Ichiro Takeuchi

Dedication

To my family:

my late dad Peppe. We miss you

my mom Penny. Here but drifting away

my sister Francesca Romana "Tata". The other, better part of me

I keep you all warm in my heart.

Acknowledgments

This thesis - and the path that led to it - is dedicated to my family: *Papa',
Mamma e Tata.* They are the roots I came from, and the place I belong and always
return to. *Grazie di tutto. Vi voglio bene.*

Working with Prof. Keith Schwab has been one of these years most formative
experiences. He gave me two chances for which I am most grateful: first when he
hired me in 2001, then - few years later - when he suggested to continue my studies
while working with him.

Keith is a passionate physicist, a source of ideas, a driving force and a very dear
friend. I learned from his professional example, I enjoyed his intelligence and his
company, and I thank him for all this.

I was also very fortunate to share this experience with the bright and talented young
researchers within Schwab's Nanomechanics group: Emrah Altunkaya, Dr. Olivier
Buu, Dr. Harish Bhaskaran, Jared Hertzberg, Dr. Alex Hutchinson, Dr. Matt La-
Haye, Dr. Akshay Naik and Dr. Patrick Truitt. I cherish them for their friendship,
the many conversations and discussions about (not just) Physics, the balanced en-
vironment they contributed to, and for making my days easier (and often funnier)

than they could have been. In particular I would like to thank Akshay for his help at the beginning of this project, and Matt, for being ... *Matt.* Also, Akshay and Matt critically revised some parts of this manuscript.

To Jared and Patrick, my partners of *resistance* during the last year at LPS: thanks! For the SQUID devices utilized in this thesis I would like to acknowledge Dr. Mark Ketchen and collaborators from IBM Research Labs, who fabricated them in the early 1990s.

I would like to express my gratitude to the members of the dissertation committee: Professor Bob Anderson, Professor Keith Schwab, Professor Alex Dragt, Professor Luis Orozco, Professor Raymond Phaneuf and Professor Ichiro Takeuchi, for kindly and patiently replying to my many emails, accommodating to my neurotic schedule, reading through the manuscript and suggesting improvements.

I also would like to acknowledge the help and support I(/we) received in the darkest times from Professor Drew Baden, Professor Greg Sullivan, Professor Nicholas Chant and Professor Jordan Goodman. A very special *thank-you* to Professor Michael Fisher, for the academic concern, delicate attention and generous involvement in our matters.

Many many thanks to the people who work "behind the scenes" and interfaced me with the "world". Ms. Jane Hessing and Ms. Margaret Lukomska were indispensable for the timely completion of official academic requirements, purchases and administrative steps.

I am also grateful to Professor Bob Anderson, Ms. Belta Pollard and Mr. Musharraf Nazir for setting up a desk and printing facilities at the Department in the days

"Yeah, well. The Dude abides." (The Big Lebowski, 1998)

Table of Contents

List of Tables

List of Figures

List of Abbreviations

β_C	Stewart McCumber parameter
β_L	Modulation parameter
η	Mismatch factor
λ	Superconducting penetration depth
μ_o	Permeability of the vacuum:
	$4\pi \text{x} 10^{-7}$ NA^{-2}
ν	Frequency in Hz
ν_j	Josephson frequency in Hz;
	$\nu_j = V/\Phi_o = V\text{x}483.6 MHz/\mu V$
ω	Frequency in rad/s
Φ	Magnetic flux
Φ_o	Magnetic flux quantum
	$(2e/h) = \approx 2.07 x 10^{-15}$ Wb
Al	Aluminum
AlO_x	Aluminum Oxide
Au	Gold
C_p	Parasitic capacitance from input coil
Cu	Copper
d	Size of the SQUID washer hole
DC	Direct Current
e	Electron charge: $1.6 x 10^{-19} C$
E_J	Josephson coupling energy
	$E_J = I_o \Phi_o / 2\pi$
G	Power gain
G_V	Voltage gain
k	Coupling coefficient between SQUID and input circuit
k_e	Effective coupling coefficient between SQUID and input circuit
I_C	SQUID critical current
I_C^{max}	SQUID maximum critical current
I_o	Josephson junction critical current
I_{mod}	Modulation coil current
$(\mathcal{I}_\phi^{mod})_{DC}$	modulation coil DC current-to-flux
	transfer coefficient
$\mathcal{I}_\phi^{modRF}$	Modulation coil current-to-flux
	transfer coefficient

I-V	Current-Voltage characteristics
L	Inductance of the SQUID washer
$\mathcal{L}$	SQUID dynamic inductance
$\mathcal{Z}^r$	SQUID dynamic *reduced* inductance
L_h	Inductance of the SQUID washer hole
L_i	Input coil inductance
L_{jp}	Parasitic junction inductance
L_p	Pickup coil inductance
L^r	SQUID resuced inductance
L_s	Stray inductance
L_{sl}	Inductance of the SQUID washer slit
L_{sl}^l	Inductance per unit-length of the SQUID washer slit
M_i	Mutual inductance between SQUID loop and input coil
n	Number of turns in the input coil
N.A.	Network Analyzer
Nb	Niobium
NOP	Negative-Postitive-Zero
NSA	National Security Agency
PMMA	Poly-Methyl Methacrylate
Q	Resonance quality factor
$\mathcal{R}$	SQUID dynamic resistance
RBW	Resolution Bandwidth of a measurement
RCSJ	Resistively and capacitively shunted junction
R_{dyn}	SQUID dynamic output resistance
RF	Radio Frequency
RF-SET	Radio Frequency-Single-Electron-Transitor
rms	root-mean-square
$\mathcal{R}^r$	SQUID dynamic *reduced* resistance
R_S	SQUID shunt resistor
R_{SET}	SET resistance
R_{SET}''	Transformed (equivalent) SET resistance
R_{input}^{SQUID}	SQUID input resistance
S.A.	Spectrum Analyzer
SET	Single Electron Transistor
S_I	Current noise spectral density
S_Φ	Flux noise spectral density
S_V	Voltage noise spectral density

SQUID	Superconducting Quantum Interference Device
SSET	Superconducting Single-Electron Transistor
STM	Scanning Tunnelling Microscope
T_N	Noise temperature
$(\mathcal{V}_\phi^{mod})_{DC}$	modulation coil DC voltage-to-flux transfer coefficient
$(\mathcal{V}_\phi^{mod})_{RF}$	modulation coil RF (rms) voltage-to-flux transfer coefficient
$(V_\phi^{SQUID})_{DC}$	SQUID flux-to-DC output voltage transfer coefficient related to a frequency ν
$(V_\phi^{SQUID})_{RF}$	SQUID flux-to-(rms) output voltage transfer coefficient related to a frequency ν
V_{device}^{output}	Device output voltage
V_{SQUID}^{output}	SQUID output voltage
$\mathcal{Z}$	SQUID dynamic input impedance
Z_o	Matching network equivalent impedance at frequency ω_o
Z_c	Matching network characteristic impedance
Z_T	Uncoupled input circuit impedance
Z_T^*	Coupled input circuit impedance
W	Size of the SQUID washer
w	Width of the SQUID washer

1.1 Introduction: statement of the problem

During the past years the shot noise-limited detection limit of a Single-Electron Transistor (SET) has been pursued by many groups in quest of sensitive and non-destructive measurement schemes for electric charge. A Single-Electron Transistor (SET) as a nearly quantum-limited charge amplifier was an obvious candidate for the read-out of charge states of a Cooper-Pair Box (CPB). It was in fact estimated that an optimized RF-SET might be able to read-out a charge qubit in a single-shot measurement [1]. Impressive progress has recently been achieved in improving the charge sensitivity, reporting $\approx 1 \times 10^{-6} e/\sqrt{Hz}$ at $40mK$ [2], but the shot noise-limit has not been reached yet. At the same time, single-shot detection of a CPB by an RF-SET proved to be rather difficult with the detector perturbing the lifetime of the excited states, while other successful readout have been developed.

This thesis proposes a new detection scheme based on a DC-SQUID, used as a low-impedance amplifier and coupled to an input circuit, impedance-matched with a DC-biased SET. The SQUID sub-flux quantum sensitivity would allow one to resolve the SET *intrinsic* noise. Furthermore the scheme, because no microwave drive would be applied to the SET, would suit those experiments where the usual RF operation of the SET imposes sensitivity limits on the detection [25].

1.2 Structure of the thesis

The thesis is structured as follows:

Chapter 2 presents an overview on shot noise in double tunnel junction systems and Single-Electron Transistors, also introducing Single-Electron Transistors sensitivity limits. Some recent results toward SET shot noise-limited charge detection are then presented, framed also by a review of some recent experiments performed in Keith Schwab's Nanomechanics group. The chapter concludes with a section introducing the motivations for the proposed detection scheme that will be detailed in the following chapter.

Chapter 3 starts with a section dedicated to the DC-SQUID principles of operation through the definition of some of the parameters that are used in the course of this work, followed by a section dedicated to a review of some important experiments studying DC-SQUIDS as RF amplifiers. Then the engineering of the proposed detection scheme is presented in detail.

Chapter4 describes the SQUID chip, the device, the ^{3}He refrigerator, its wiring and the measurement apparatus.

Chapter5 is dedicated to the experimental results: device characterization, sensitivity and noise temperature.

Appendix A describes the SET bias circuit.

Appendix B describes flux noise measurements on an uncoupled SQUID.

Chapter 2

Motivation

This chapter provides the motivation for the work presented in this thesis. After having introduced the shot noise in tunnel junctions and single-electron transistors, a short overview on SET and RF-SET sensitivity limits is presented, together with some recent results to illustrate shot noise-limited detection progress for such systems. Further motivation and background are also provided in the context of some recent experiments performed in Schwab's Nanomechanics group. The chapter is then concluded by introducing the proposed detection scheme that will be described in detail in Chapter 3.

2.1   Shot noise in tunnel junctions

Shot noise is a manifestation of the discreteness of the charge, i.e. of the *quantum randomness of the time intervals between tunnel events* [1]. For a tunnel junction, shot noise spectral density S_I can be derived from the difference of the tunneling rates from one energy level on one side of the junction to the other side [3, 4]. In the low frequency limit of a single tunnel junction with low transmission coefficient this reduces to [5]:

$$S_I = 2eI coth\left(\frac{eV}{2k_BT}\right) \tag{2.1}$$

where I is the tunnel current, V the voltage across the junction, and T its

temperature.

Two limits set the boundaries in the previous expression:

A. $|V| >> k_B T/e$: the shot noise *Shottky* [6] relation $S_I = 2eI$ is recovered, characteristic of Poissonian, uncorrelated charge transfer of independent units of e.

B. $|V| << k_B T/e$: the equilibrium, Nyquist-Johnson noise ($S_I \approx 4k_B T/R_T$) is obtained, where R_T is the junction tunnel resistance.

In this section the topic of shot noise in tunnel junctions is introduced empirically through the results obtained from scanning tunneling microscope (STM) experiments performed in 1995 by Birk and collaborators (Figures 2.1 and 2.2, reproduced from Ref. [7]).

Figure 2.1 [7] illustrates the STM current noise data (S_I) of a single tunnel junction as a function of the current I. Samples consisted of a mica substrate where a layer of epitaxial Au(111) had first been deposited, followed by a thin Zr-oxide insulating layer, and then by a discontinuous gold film (grain average size $\approx 5nm$). Single barrier tunnel junctions were realized by positioning the microscope tip above the insulating layer, acting as a tunnel barrier, while double-barrier tunnel junctions were formed when the tip was placed above one of the metal particles. In the experimental set-up the current noise of the junction was measured simultaneously with the current I using a series resistor and a field effect transistor placed in proximity with the tip.

Data shows a temperature dependent crossover in the current noise characteristics from thermal to shot noise, with the metallic junction displaying a full classical shot noise in the limit $|V| >> k_B T/e$.
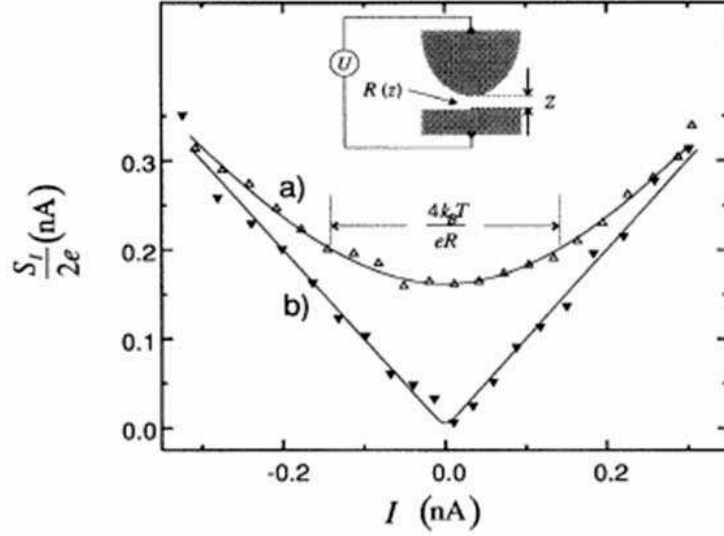
Figure 2.1: Current noise of a single tunnel junction measured at (a) $T = 300K$ (open triangles)) and (b) $T = 77K$ (solid triangles). Inset shows schematic of the tip, sample and current preamplifier. Reproduced from Ref. [7].

When a number N of tunnel junctions is connected in series, the shot noise assumes a reduced expression [8], [5] that for N=2 is given by:

$$S_I = 2eI \left(\frac{1}{N}\right) coth \left(\frac{eV}{2Nk_BT}\right) = eI coth \left(\frac{eV}{4k_BT}\right) \qquad (2.2)$$

Figure 2.2 refers to analog measurements taken on a single and (nearly symmetric) double barrier tunnel junction, at $T = 4.2K$. As a consequence of the smallness of the island formed by the two interconnected middle electrodes in the

double tunnel junction [1], the tunnel junction I-V characteristic [2] manifests Coulomb blockade effects, briefly described in the following (curve (b) in Fig. 2.2 inset). When a small bias voltage (smaller than the Coulomb blockade onset) is applied to the electrodes, the current through the double junction system is blocked by the energy barrier related to the island charging energy. For larger applied voltages, the blockade is overcome and a tunneling current can flow.

The main result in Fig. 2.2 is the suppression of the measured shot noise by a factor 0.6 compared to the full-Poissonian, single barrier junction shot noise measured values.

While suppression of the shot noise could be interpreted as the classical superposition of two independent noise sources [7, 13], deviations from the classical behavior due to Coulomb interactions were not experimentally accessible for the symmetric double barrier tunnel junction system. Indeed, the same measurement was repeated for a strongly asymmetric double barrier tunnel junction and is presented in Fig. 2.3 [7].

As in fact explained by the conventional theory of tunneling [10, 12], when $k_B T$ is smaller than the Coulomb energy, and the junction resistances are larger than the quantum of resistance $R_K \approx 26k\Omega$, the addition of charges to the central electrode by thermal or quantum fluctuations is suppressed, and the island may be considered confined to a discrete set of charge states. In this framework the tunnel-

---

[1]The island charging energy is $E_C = e^2/(C_1 + C_2) >> k_B T$, with $C_{1,2}$ the junctions capacitances.

[2]Referred as I-U curves in Figures 2.1 and 2.2 from [7].
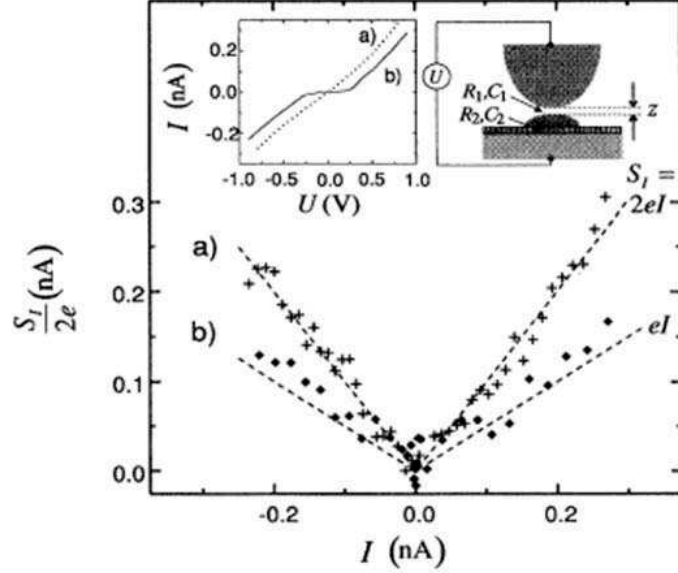
Figure 2.2: Current noise measured at $T = 4K$ of (a) a single tunnel junction (crosses) and (b) double tunnel junction (diamonds). Inset shows current-voltage characteristics for both devices. Reproduced from Ref. [7].

ing events in the junctions are mutually correlated [12].

Correlation can explain the different features present in IV characteristics, in particular their extreme sensitivity to background charge in the central electrode. Moreover, *correlations* in electron transmission can suppress the shot noise from the Poisson limit[3].

---

[3]Another source of correlations is the Pauli exclusion principle, responsible for example for the
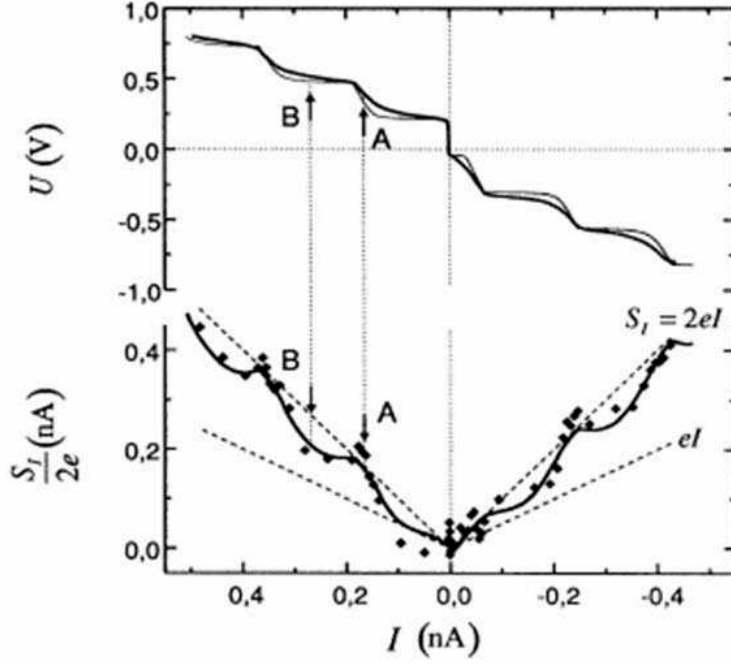
Figure 2.3: Upper curve: Coulomb staircase for a strongly asymmetric double barrier tunnel junction: measured (thick curve) and simulated (thin curve). Lower curve: measured current noise (diamonds) and theoretical curve (line). Letters A and B mark the plateaux/steps in the current-voltage characteristics, corresponding to maximum (minimum) shot noise. T=4.2K. Reproduced from Ref. [7].

Figure 2.3 illustrates a pronounced Coulomb staircase (upper curve), whose steps correspond to a number of excess electrons on the island increased or decreased by one. The corresponding noise signal (data points in Fig. 2.3) oscillates between the full ($2eI$) and suppressed shot noise level, in correlation with the plateaux (steps) in the current-voltage characteristic curve. In fact, by considering only two possible charge states on the island, current plateaux of strongly asymmetric double tunnel junctions represent uncorrelated tunneling events. On the contrary, current steps,

suppression of the shot noise in a quantum point contact [4, 9].

8

for which charge states are degenerated in energy, present a suppression of the shot noise due to correlations between tunnneling events in the two junctions [7, 13].

A *Fano factor F* can be introduced, defined by the ratio of the shot noise to the shot noise in the Poisson limit:

$$F = \frac{S_I(\omega)}{2eI}, \tag{2.3}$$

The Fano factor can be less than, greater than or equal to unity, and, specifically, can give information about how tunnel events are correlated.

The two junction system is the building block of the Single-Electron Transistor (SET). When the island of a double tunnel junction with capacitances $C_{1,2} \approx 0.1 - 10fF$ is electrostatically coupled to a gate electrode, an external electric field can be applied from the gate to the island, and a polarizing charge is induced, modifying the background charge level on the island. As a consequence the Coulomb blockade can be detuned and current flows across the junctions. The most striking features of the Single-Electron Transistor are the modulation of the current by the voltage applied to the gate and its very high sensitivity to the charge on the island. The SET ultimate sensitivity is limited by its *intrinsic* noise given by the shot noise in the drain-source current [10, 12]. In the framework of the conventional theory of sequential tunneling, SET *intrinsic* noise was derived by Korotkov [10, 12] and independently by Hershfield et al. [13] in the low frequency range [4].

Analytic shot noise forms could be found for some regions of the normal-state SET $I_{drain-source} - V_{drain-source} - V_{gate}$ map [10] [12] [13] and will be presented in the

---

[4]$\omega << (R_i C_i)^{-1}$, system charging frequency, where $R_i(C_i)$ are the junctions resistances (capacitances), $i = 1, 2$.

following without derivation [5]. If V is the SET bias voltage, these regions can be defined by the following boundaries [13]:

Zero voltage regime (V=0): The SET produces only thermal noise.

Thermally activated regime ($E_C >> e\,|V| >> k_B T$): The voltage does not provide enough energy to overcome the charging energy, but still there is thermal activation. By neglecting degeneracies [13] and considering only one charge state occupied, conduction happens through uncorrelated Poissonian events, and shot noise recovers the standard relation: $S_I = 2eI$.

Two state regime ($|V| > E_C >> k_B T$): Since the voltage is larger than the charging energy, current flows. The island can be in two charge states, so two tunneling rates can be defined for $I > 0$: Γ^L (Γ^R) decreasing (increasing) the number of electrons by tunneling through the left (right) junction, both rates depending on the voltage. The noise spectral density is then:

$$S_I = 2eI \frac{(\Gamma^R)^2 + (\Gamma^L)^2}{(\Gamma^R + \Gamma^L)^2}|_V \tag{2.4}$$

High voltage regime ($e\,|V| >> E_C$): The SET shot noise is asymptotically

---

[5]Shot noise in superconducting SETs has also been studied, adding coherence effects into current fluctuations. See for exemple Ref.[14]. In this chapter only an introduction to the shot noise predictions in normal-state SET is provided, to illustrate the complexity of the SET shot noise map, still unexplored in the SET limits of detection.

equivalent to a system with two noise sources:

$$S_I = 2eI \frac{R_L^{-2} + R_R^{-2}}{(R_L^{-1} + R_R^{-1})^2} \tag{2.5}$$

2.2 (DC/RF)-SET sensitivity limits

Intrinsic noise calculations have been utilized to determine SET charge sensitivity [12]. When coupled through the gate to a (charge) signal source $\partial Q(\omega)$, the device charge resolution was obtained by equating the output signal ∂I to the system rms current fluctuations $[S_I(\omega)\Delta f]^{1/2}$, with Δf the device output bandwidth. In the case of source-drain voltages below the blockade gap and for low frequencies (as specified above), Devoret and Schoelkopf [1] determined the optimum value for the charge sensitivity of a SET:

$$\partial Q_{opt} \leq 1.7 \times 10^{-6} \frac{e}{\sqrt{Hz}} \tag{2.6}$$

Also, by expressing the SET as a linear voltage amplifier [1], the *noise energy* (E_N) can be introduced as $E_N = \sqrt{S_V^{ampl} S_I^{ampl}} \geq \hbar\omega/2$, whose lower limit comes from quantum mechanical considerations after applying the Heisenberg principle to continuous measurements [15].

The spectral densities $S_V^{ampl}(\omega)$ and $S_I^{ampl}(\omega)$ belong to two noise sources V_N and I_N describing the fluctuations introduced by the amplifier. $V_N(\omega)$ represents the voltage noise added by the amplifier at its output but referred to the input, while

the current noise term $I_N(\omega)$ is the current noise describing the back-action of the amplifier into the input circuit.

Devoret and Shoelkopf [1] found that, in the framework of the conventional theory of sequential tunneling, and neglecting thermal fluctuations, the following relation holds for an *optimized* SET:

$$E_N^{opt} \leq 2.2\hbar\omega \tag{2.7}$$

and for source-drain voltages below the Coulomb gap and at low frequencies on the tunnel rate scale.

The value of E_N^{opt} shows that the SET is a nearly quantum-limited amplifier: amplification can be realized with back-action close to what is predicted by the uncertainty principle. An improved SET detection scheme, with the SET output power noise dominating the noise of the following amplifier, would allow to utilize this potential to its fullness [1].

On the other hand, despite the excellent sensitivity prospects, the SET suffers from an operational drawback: its direct read-out bandwidth is limited to few hundreds of kHz because of the resistance-capacitance product of the SET resistance $(50 - 200K\Omega)$ and the parasitic leads capacitance $(\approx 0.1 - 1nF)$.

In order to overcome this limitation the RF-SET scheme was developed [16, 17], consisting of a SET embedded in an LC tank circuit, transforming the SET impedance close to that of a 50Ω transmission line.

A microwave carrier is sent into the device and reflected back by the combined impedance SET+tank circuit. As changes in the SET gate charge cause changes in

SET differential resistance, these are carried in turn by amplitude modulations of the reflected wave.

The ultimate charge sensitivity for the RF-SET operated in the pure RF mode [6] has been calculated by Korotkov and Paalanen [11] to be about 1.4 times worse than for conventional SETs. Hence, for both the best SETs and RF-SETs, charge sensitivity limits set by the intrinsic (shot) noise should be placed around $1\mu e/\sqrt{Hz}$.

Motivated by the growing interest in sensitive measurements applications such as, for example, solid state quantum bits and quantum gates, a series of experiments performed in the past few years has shown steady progress in improving the performance and the charge sensitivity of RF-SETs [2, 18, 19, 20, 21]. In particular one of the most recent technological improvements has been achieved by Brenning and collaborators [2]. By using low oxidation pressures during the fabrication of the SET, higher charging energies were reached, improving both charge sensitivity [11] and the operating temperature, while keeping the SET's ohmic tunnel resistance relatively low ($25K\Omega$). While excellent (and record-to-date) charge sensitivities were measured ($\approx 1.0\mu e/\sqrt{Hz}$ at $40mK$ and $\approx 2\mu e/\sqrt{Hz}$ at $4K$ for both superconducting and normal-state SETs), shot noise-limited detection was not achieved. When measuring the device output noise power, the high drain-source (I_{DS}) current shot noise asymptotes intersected at the amplifier noise contribution ($\approx 10K$), higher than the amplifier noise temperature itself ($2K$), probably because of unaccounted losses or possibly overheating of the electrons in the island.

Lastly, a very recent result has been obtained by realizing an on-chip superconduct-

_____

[6]Large RF amplitude, no source - drain voltage applied to the SET.

ing LC matching network [21], for which a charge sensitivity in the superconducting state was measured of about $2.4-3.1 \times 10^{-6} \mu e/\sqrt{Hz}$. Again, the first stage low-noise HEMT [7] amplifier proved to limit the noise temperature of the detection scheme, as a consequence noise-limited detection of the Single-Electron Transistor could not be achieved, and uncoupled energy sensitivity was in fact derived to be $1.9 - 3.1\hbar$.

2.3   Nanomechanics experiments and detection limits

The experiments performed in Keith Schwab's group in the past few years have aimed at the study of collective quantum behavior of nanomechanical resonators equivalent in mass to about 10^{12} hydrogen atoms. The quantum limit has been approached by exploring position detection ultimate limits and by the observation of low quantum numbers through successful cooling resonators to about $50mK$. Figure 2.4 illustrates the layout of the experiments.

The measurement scheme included an RF-SET, with a nanomechanical beam capacitively coupled to the gate of the SET island, schematically presented in Fig. 2.4(a) (reproduced from Ref.[22]). The in-plane movement of the beam modulated the polarization charge on the SET island, changing the SET impedance, and thus affecting the modulation of the amplitude of the reflected wave.

Figure 2.4(c) shows, for the LaHaye experiment summarized in the following [22][8],

---

[7]High Electron Mobiliy Transistor

[8]Author contribution to Ref.[22]: B. Camarota participated in the project and was responsible for the development of a successful recipe for the chip layout, membrane, tank circuit design and fabrication. For more detail, see Ref.[23].

the on-chip superconducting tank circuit inductor and capacitor, fabricated on $500\mu m$ thick (100) Silicon wafers, coated on both sides by $0.1\mu m$ of low-stress, amorphous silicon nitride (Si_3N_4) deposited by LPCVD (Low-Pressure-Chemical-Vapor-Deposition).

The inductors for the LC resonator were defined by e-beam lithography and by evaporation (and subsequent lift-off) of a $0.1\mu m$ layer of aluminum.

The contact pads and capacitors were defined by optical lithography and by e-beam evaporation (and lift-off) of a tri-layer of metals $(0.2\mu m(Al)/0.02\mu m(Ti)/0.02\mu m(Au))$, superconducting below 0.8K.

Figure 2.4(b) shows a blow-up of the free-standing beam separated by a $\approx 600nm$ gap from the SET island. The nanomechanical resonator, coated with $700nm$ of Au, was defined on a Si_3N_4 membrane obtained through KOH wet etching at the center of the chip.

The Al SET was fabricated using e-beam lithography and the bi-layer/double-angle evaporation technique. Finally the nanomechanical resonator was freed from the surrounding Si_3N_4 membrane through a dry-RIE (Reactive Ion Etching) step process.

LaHaye's experiment was engineered to optimize displacement sensitivity. In particular the forward coupling SET-beam was studied, where the contribution of the detector (SET) to the displacement noise was inversely proportional to the capacitive coupling with a $\approx 20MHz$ nanomechanical resonator [22, 23].

The SSET (Superconducting Single-Electron Transistor) was kept at its maximun charge sensitivity ($\approx 10\mu e/\sqrt{Hz}$), and the beam-SET coupling voltage was re-
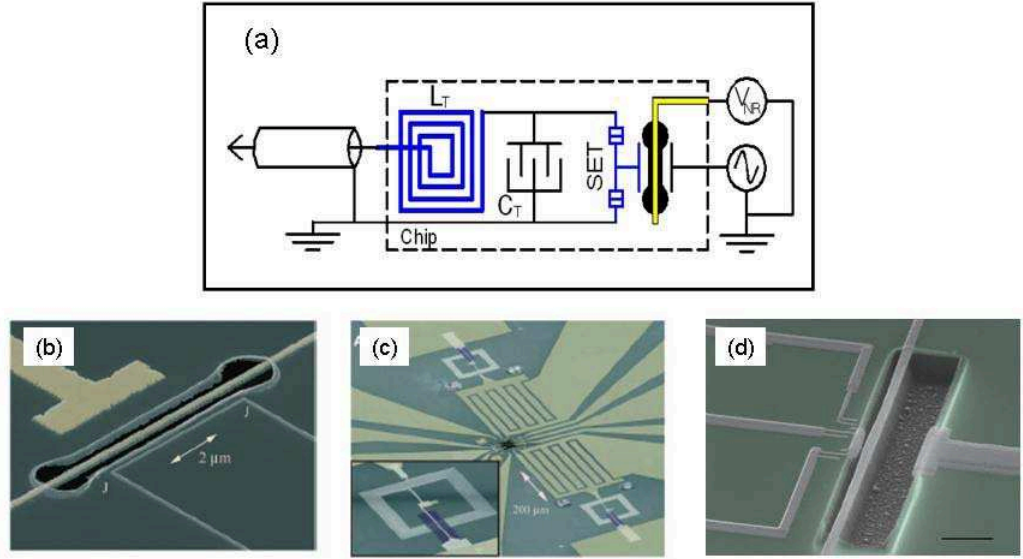
Figure 2.4: (a) Schematic of the experiments described in Ref.[22] and [25]. (b) LaHaye's beam and SET island. (c) On-chip tank circuit. (d) Naik's beam and SET. Reproduced and adapted from [22] and [25].

stricted to a region where the detection resolution, improving with increasing coupling, was limited by the shot noise through the SET. Integrated charge noise power data around the mechanical resonance were collected and the detection scheme noise temperature was determined, from which, through the application of the equipartition theorem, a displacement sensitivity $\sqrt{S_x} = 3.8 fm/\sqrt{Hz}$ was found, translating into a position resolution a factor of 4.3 above the quantum limit.

Yet, because of losses in the detection circuit, characteristics of the tanks circuit,

and a contribution from the following HEMT, shot noise-limited detection was not

achieved. Figure 2.5 [22] illustrates a position resolution versus coupling plot. The

black line represents the expected shot noise-limited displacement resolution calcu-

lated from the experimental parameters, while the dots represent the experimental

data and the dashed line is the expected sensitivity derived from the SSET charge

sensitivity.
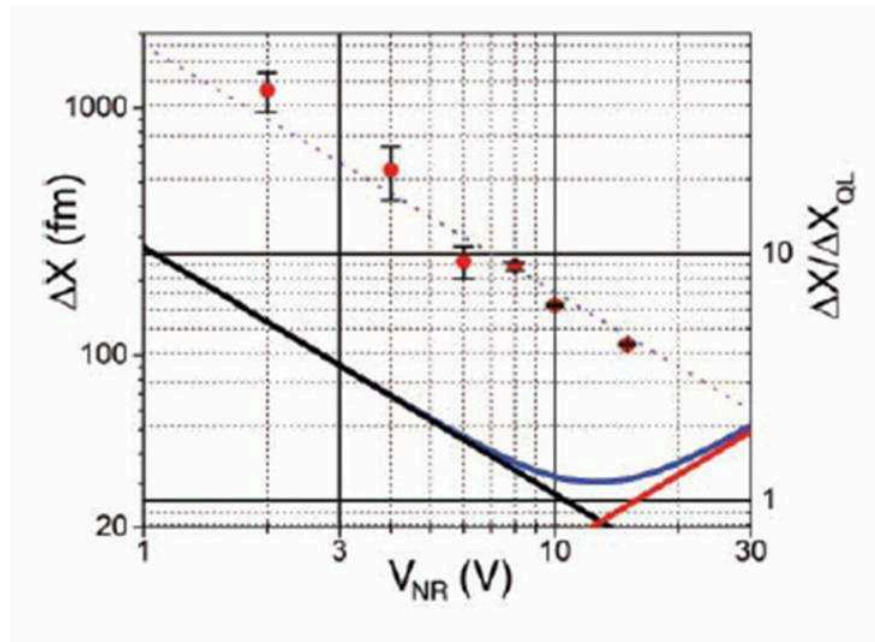
Figure 2.5: LaHaye experiment. Position resolution versus coupling plot.
Reproduced from [22].

The red line represents the back-action noise.

In fact, by increasing the coupling with the nanomechanical resonator, back-action

17

- due to voltage fluctuations in the SET island - contributes to the displacement noise. Optimal position sensitivity is located at the sweet spot between these two regimes.

Figure 2.4(d) shows a detail of Akshay Naik's device [24, 25], where the gap between the $22MHz$ nanoresonator and the SET island was reduced to about $100nm$, shifting the onset of the back-action branch towards low coupling voltages.

It was thus possible to explore the back-action regime for a SSET. Figure 2.6 [25][9] shows the displacement resolution *versus* coupling voltage plot referring to one of the devices used by A. Naik and collaborators [24, 25].

The horizontal red line represents the quantum limit in the detection. Dashed lines are the forward coupling and the back-action contributions to displacement resolution. The black curve represents the calculated ultimate resolution assuming the read-out at the shot noise limit. The blue curve was calculated for an RF-SET bias point giving a charge sensitivity of about $10\mu e/\sqrt{Hz}$. Its sensitivity results limited by the amplifier. The green curve refers to the same SSET operated at a $170\mu e/\sqrt{Hz}$ charge sensitivity. The dots are the experiment data points.

The dramatic change in SSET charge sensitivity was related to the different bias and working conditions the SSET was operated at. Backaction studies were performed around some features in the SSET map peculiar to the superconducting state and involving the additional effect of coherent tunneling of Cooper pairs (the *Josephson quasiparticle* resonances, *JQP*) [67, 68].

---

[9]Online Supplementary Information:

http://www.nature.com/nature/journal/v443/n7108/full/nature05027.html.
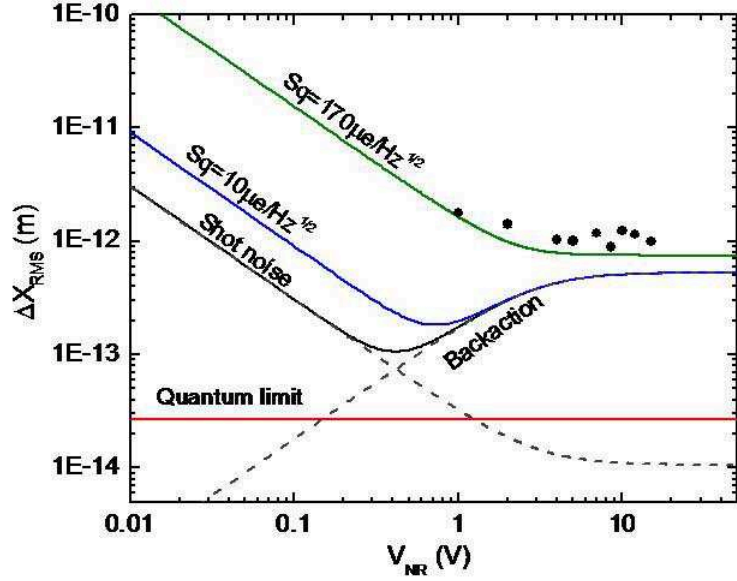
Figure 2.6: Backaction experiments, displacement resolution *versus* coupling voltage plot. Reproduced from [25].

The back-action effects proved to be strongly dependent on the exact bias conditions of the transistor [69], and a reduced microwave amplitude was necessary to explore the different regions (Fig. 2.7, from [24]). Ultimately, the price to pay was a reduced signal-to-noise ratio, a degraded charge sensitivity ($170\mu e/\sqrt{Hz}$) and as a consequence a worse displacement resolution. It is in fact known that SSET optimum charge sensitivity is achieved for an RF signal amplitude comparable to the Coulomb blockade voltage [18].

19
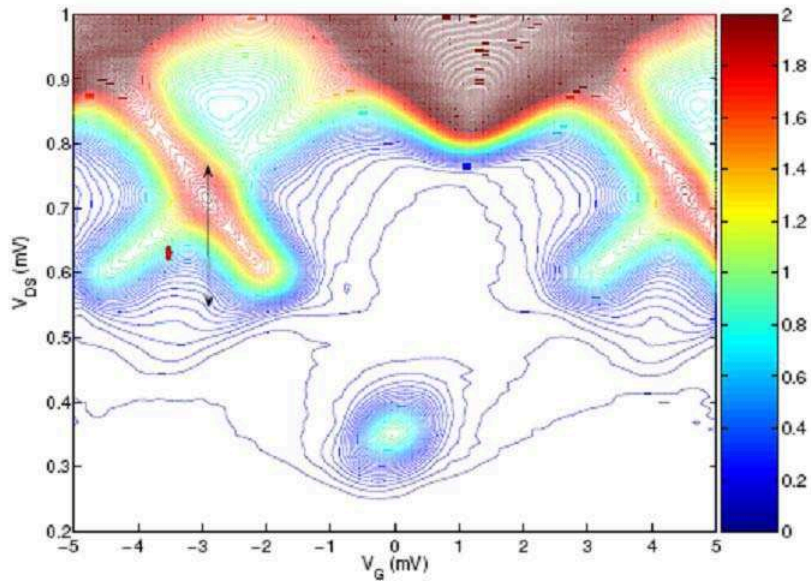
Figure 2.7: Microwave amplitude for optimal position detection (arrow) and optimal backaction bias (red dot). Map $I - V_G - V_{DS}$ of a SSET. Reproduced from [24].

2.4 What about SQUIDs?

Shot noise-limited detection of (SETs or) RF-SETs can be approached as a fabrication challenge [2] or as a quest to improve existing detection schemes [21]. In the detection schemes here presented the detection bottleneck was nevertheless mainly represented by the noise floor set by the second amplifier stage. In particular, by borrowing an exemplifying scheme from Roschier et al. [20] (Fig. 2.8 (a)), the RF-SET detection scheme can be viewed as a cascade of two amplifiers

(of gain $G_{1,2}$ and noise $N_{1,2},$), where the state-of-the-art cryogenic HEMT limits the detection sensitivity. One could think [1] [20] thus to replace/precede the HEMT by a low impedance amplifier such as a Superconducting-Quantum-Interference-Device (SQUID): in particular, a SQUID with a microstrip input line demonstrated to have a noise temperature $T_N \approx 0.12K$ at $438MHz$, i.e. $k_B T_N \approx 5\hbar\omega$ [26] was proposed. An estimate [23] was performed by Matt LaHaye in his PhD thesis, with the hypothesis of using such a SQUID -followed by a HEMT- for the read-out of the RF-SET in the detection scheme used in his experiment. By assuming a gain of $20dB$ and a noise temperature of $100mK$ for the microstrip SQUID, and inserting a $5dB$ loss in the circuit, a detection noise temperature $T_N^{det} \approx 250mK$ was derived, that would allow a reduction of the charge sensitivity to the ultimate shot noise limit for the same SET parameters used in the experiment of LaHaye and collaborators. On the other side though, concern was raised [23] about the level of reflected power from the RF-SET (as high as $100pW$ for certain bias conditions) that could wash-out the improvements hoped with the use of a SQUID amplifier.

A new detection scheme has been proposed and engineered in this work (see Chapter 3), based on a DC-SQUID impedance-matched with a DC-biased SET (Fig. 2.8 (b)). Because of the SQUID sensitivity, the fundamental noise of the SET could be resolved. Moreover, since the SET would be DC-biased, the scheme would present the advantage of overcoming the limitations in the read-out of a Single-Electron Transistor briefly reviewed in the previous section, in particular for experiments requiring a fixed SET bias point.

Figure 2.9 is a simplified schematic of the detection scheme. A DC-SQUID is coupled
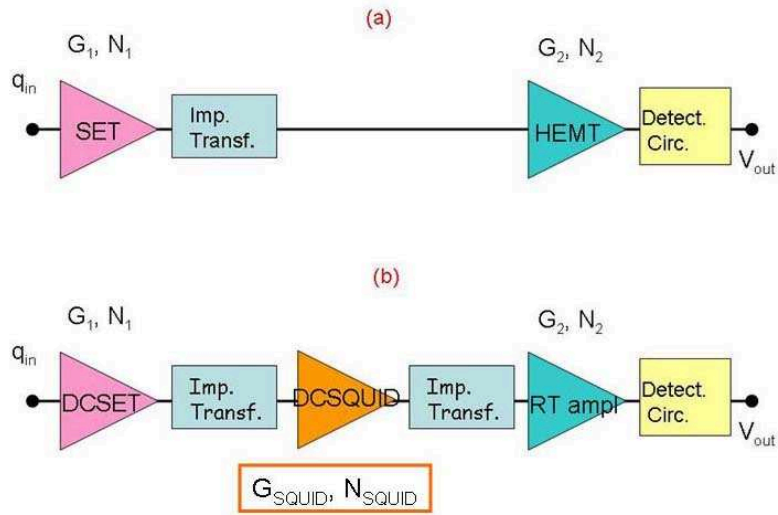
Figure 2.8: (a) Conventional RF-SET scheme represented as cascade of two amplifiers. (b) Proposed detection scheme of this thesis: a DC-biased SET, impedance matched with a DC-SQUID. Adapted from Ref. [20].

to the DC-biased SET through an input coil and an impedance matching circuit. The output of the SQUID is connected to a detection matching circuit. Both matching circuits are engineered to resonate around $10MHz$ [10]. The bias of the SET (here not shown) is described in Appendix A.

---

[10]In the frequency range of the resonances of the nanomechanical resonators studied in Schwab's group.
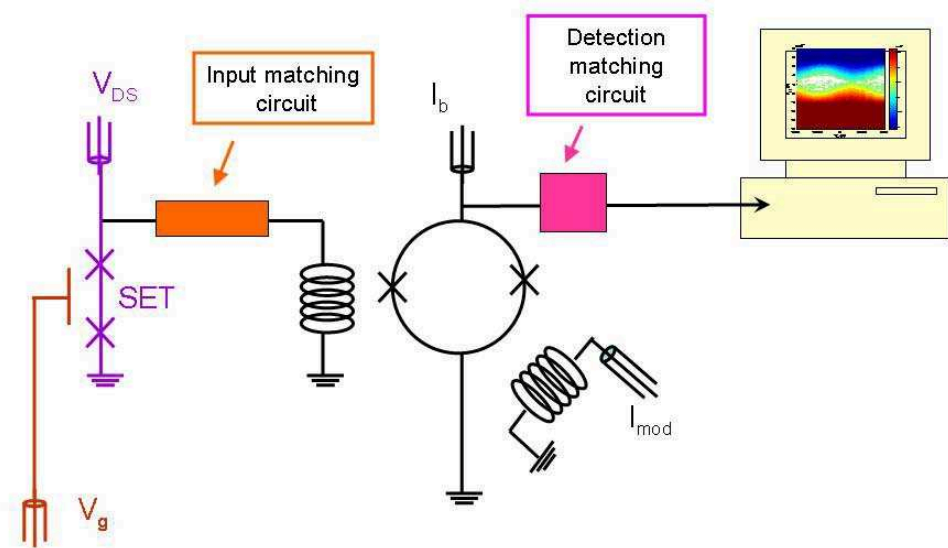
Figure 2.9: Detection scheme of this thesis.

Chapter 3

Detecting a SET with a DC-SQUID: engineering the detection

scheme

The proposed detection scheme is presented in the present chapter in Section

3.3, introduced by a concise review of DC-SQUIDs principles of operation (Section

3.1) and by a section dedicated to DC-SQUIDs as RF amplifiers (Section 3.2).

3.1   DC-SQUID: principles of operation

A DC-SQUID consists of two Josephson junctions connected in parallel by a

superconducting loop. Its principles of operation are based on two physical phenom-

ena: Josephson tunneling [27, 28] and flux quantization in a closed superconducting

loop [29][1].

Figure 3.1(a) [2] illustrates the schematic for a DC-SQUID of loop inductance L,

where the Josephson junctions have been represented by their lumped equivalent

circuit, i.e. an idealized Josephson element of critical current I_o, the junction (self-)

capacitance C, and an ohmic resistor R, all in parallel.

To analyze the system's behavior it is possible to write the junctions equa-

tion of motion in absence of noise in the framework of the RCSJ (*resistively-*

---

[1]Φ_o is the flux quantum: $\Phi_o = h/2e \approx 2\text{x}10^{-15}Wb$.

[2]reproduced from Ref.[30]
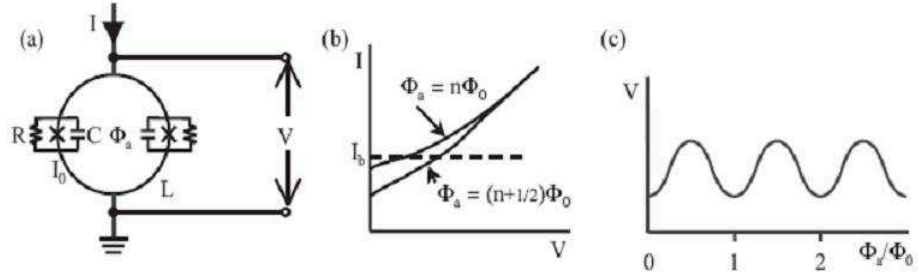
Figure 3.1: (a) SQUID schematic; (b) I-V characteristics; (c) SQUID voltage *versus* Φ/Φ_o. Reproduced from Ref.[30].

and capacitively- shunted junction) model [32] [30]. A useful parameter (*Stewart-McCumber* parameter, β_c) can be introduced as:

$$\beta_c = \frac{2\pi I_o R^2 C}{\Phi_o} \tag{3.1}$$

in two limiting cases: $\beta_c >> 1$ (strongly *underdamped* limit) and $\beta_c << 1$ (strongly *overdamped* limit).

These limits are better understood when looking at the analogy with the equivalent mechanical *tilted washboard* model. The model describes a pointlike particle of mass

m, sliding down a tilted washboard. In the washboard-SQUID analogy, the spatial coordinate is replaced by the superconducting phase difference δ. Moreover the mass m is proportional to the capacitor C, 1/R is related to the friction coefficient, and the external force has its analogue in the bias current I.

If the force (applied current) tilts the slope less than a critical angle (critical current), the particle is trapped in one of the washboard potential minima (i.e. the phase difference oscillates at the plasma frequency [3]).

When the slope exceeds the critical inclination, the particle starts rolling, i.e. the phase difference starts evolving in time, and a voltage develops across the junction according to the ac-Josephson relation:

$$\frac{d\delta}{dt} = \frac{2eV}{\hbar} = \frac{2\pi V}{\Phi_o} \qquad (3.2)$$

where V is the time-averaged voltage across the Josephson Junction. The Josephson frequency (ω_j) is defined by[4]:

$$\omega_j = \frac{2\pi V}{\Phi_o} \qquad (3.3)$$

When the tilting force (the current) is reduced from above its critical value, the particle is trapped back into one of the washboard minima for a value of the force (current) related to the inertial term (capacitance):

1) for a negligible inertial term (strongly overdamped limit, $\beta_c << 1$) the particle is trapped in one of the minima as soon as the force (current) reaches the critical value, resulting in non-hysteretic characteristics;

2) in the opposite limit (strongly underdamped limit, $\beta_c >> 1$) the particle traps

---

[3]$\omega_p = \sqrt{2\pi I_o/\Phi_o C}$.

[4]$\nu_j = \omega_j/2\pi = V \times 483.6 MHz/\mu V$.

for a slope lower than the critical one, resulting in a hysteretic dynamic behavior. In the underdamped limit[5] SQUID I-V characteristics are hysteretic. In practical low-T_C SQUIDs the hysteresis is usually removed by adding a metallic film strip as a shunt (few Ω) resistor such that $\beta_c << 1$.

Moreover, when current-biasing the SQUID at $I > I_C$ [6], the modulation of the junctions critical current - resulting from quantum interference of the wave functions in the superconducting loop - translates into modulation of the SQUID voltage output in units of Φ_o [31](Fig. 3.1(c)). The SQUID voltage swings, with period Φ_o in Fig. 3.1, are optimized through a *screening* parameter $\beta_L \leq 1$ defined by the following equation:

$$\beta_L = \frac{2LI_o}{\Phi_o} \tag{3.4}$$

When fluctuations are taken into account [30], simulations show in fact that the critical current modulates with the optimum ratio of about $I_C^{max}/2$ for $\beta_L = 1$, where I_C^{max} is the maximum supercurrent. In addition to the conditions $\beta_C \leq 1$ and $\beta_L = 1$, SQUID parameters are bound to two additional constraints to avoid the suppression of macroscopic quantum interference in presence of thermal fluctuations:

1) phase fluctuations need to be smaller than the coupling energy E_J:

$E_J = \hbar I_o/2e \geq k_B T$;

2) by equating the fluctuation amplitude of the total flux to the average energy of an harmonic oscillator, an upper limit on the SQUID inductance is set by [7]:

---

[5]Usually the case for low-T_C Josephson junctions.

[6]I_C is the SQUID critical current, with $I_C = 2I_o |cos(\pi\Phi/\Phi_o)|$.

[7]A more quantitative estimate can be found in Ref.[32].

$L \leq \Phi_o^2/4k_BT$.

From the SQUID voltage-flux $(V-\Phi)$ curve it is possible to define the *flux-to-voltage transfer coefficient* $(V_\Phi = |\partial V/\partial \Phi|)$:

$$\frac{\partial V}{\partial \Phi} = \frac{-2\pi \left(\frac{I_oR}{\Phi_o}\right) \left(I_o sin(\frac{\pi\Phi}{\Phi_o})cos(\frac{\pi\Phi}{\Phi_o})\right)}{(I^2 - I_C^2)^{1/2}} \tag{3.5}$$

The maximum of V_Φ defines the SQUID working point when operated in the small-signal mode [30]. While in the absence of thermal fluctuations the previous expression (Eq. 3.5) diverges for $I = I_C$, numerical simulations performed in the case of nonzero temperature [30] show that the divergence in Eq. 3.5 is removed, thus $V_\Phi = |\partial V/\partial \Phi|$ can be determined for all currents.

At $T \neq 0$ Nyquist noise from the junction shunts introduces a white voltage noise spectral density:

$$S_V = 4k_BTR. \tag{3.6}$$

Hence a partially correlated circulating current noise S_J [8], introducing a voltage noise in any input circuit coupled to the SQUID (see Section 3.2 in the following), can be expressed as:

$$S_J = \frac{4k_BT}{R}. \tag{3.7}$$

As a consequence the flux noise spectral density is given by:

$$S_\Phi = \frac{S_V}{V_\Phi^2}. \tag{3.8}$$

Optimized expressions of V_Φ, $\sqrt{S_V}$ and $\sqrt{S_\Phi}$ have been obtained from numerical simulations in the regime of small thermal fluctuations and for $\beta_L = 1$ and

_____

[8]With S_{VJ} the current and voltage noise correlation term, for which an expression will be given in Eq. 3.9.

$\Phi = (2n + 1)\Phi_o/4$ [9]:

$$V_\Phi \approx \frac{R}{L};$$

$$S_V \approx 16k_B TR;$$

$$S_\Phi \approx \frac{16k_B TL^2}{R};$$

$$S_J \approx \frac{11k_B T}{R};$$

$$S_{VJ} \approx 12k_B T. \tag{3.9}$$

In order to characterize the white flux noise in a DC SQUID a parameter (*noise energy*, Eq. 3.10) can also be introduced:

$$\epsilon(\nu) = \frac{S_\Phi(\nu)}{2L}. \tag{3.10}$$

In the hypothesis that the SQUID flux noise is generated by the Nyquist noise in its shunt resistors, noise energy takes the form expressed in Eq. 3.11.

$$\epsilon(\nu) = \frac{16k_B TL}{R}. \tag{3.11}$$

It has to be stressed though that, when a SQUID is coupled to an input circuit, such definition does not fully characterize the SQUID noise properties, since it does not account for the SQUID current noise interaction with the input circuit. So, although expressed in units of $\hbar$, noise energy is not bound by rigorous limits set by quantum mechanics as indeed is the noise temperature T_N [10] of a SQUID as an amplifier [33].

The temperature dependence of noise energy was investigated for a series of SQUIDs

---

[9]See Ref. [30] for a series of references.

[10]That will be introduced in the following of this chapter, Eq. 3.21

cooled to low temperatures and detected by a second SQUID as a preamplifier stage [33, 34]. The noise energy was found to scale with temperature (as in Eq. 3.11) down to about an effective electron temperature $T_e \approx 150mK$, and to saturate for lower temperatures. The saturation was connected to the hot-electron effect [35] in the resistive shunts [34]. By connecting the resistive shunts to large volume cooling fins, the electron gas was cooled more efficiently because of the increased electron-phonon reaction volume, and the effective electron temperature was successfully reduced to about 50mK, corresponding to a noise energy of about $5\hbar$, meaning a reduction by a factor ≈ 3 compared to the fin-less case. The hot-electron effect is supposed to play a role for typical SQUIDs cooled down below 100-200mK, while it is not expected to contribute at temperatures above this range.

3.2   DC-SQUIDs as RF amplifiers

An isolated DC-SQUID behaves as a flux-to-voltage transducer when in the current bias mode, i.e. when a constant current flows through the SQUID and its output voltage is recorded. On the other hand, the study of a DC-SQUID as RF amplifier developed by several authors [36, 37, 38, 39, 40, 41, 42, 43] concerned in first instance the analysis of a SQUID inductively coupled to an input circuit. When the SQUID is strongly coupled to the input circuit, both the SQUID properties and the input circuit impedance are expected to be affected, respectively by the presence of the input circuit and by the nonlinear impedance and voltage noise reflected back from the SQUID [37, 38, 39, 40, 42, 43, 44].

Depending on the SQUID and input coil structure, together with the SQUID bias and operating conditions, a *weak coupling* case can also occur, where the the SQUID parameters are unaffected by the presence of the input circuit [41, 42]. Ultimately, a real SQUID might even sit in between the two extreme coupling cases. This section briefly presents the main theoretical and experimental results for the strong coupling case.

3.2.1   DC-SQUID/input circuit interaction

Figure 3.2(a)[11] illustrates the schematic of a SQUID coupled to a tuned input circuit as studied by Hilbert and Clarke [37, 38, 39, 40].

The SQUID is represented by its *bare* parameters (loop inductance L, junction resistance R and capacitance C, bias and circulating current I and J, as well as its output voltage V). The input circuit is shown with a source voltage V_i, input inductance L_i [12], resistor R_i and capacitor C_i. Coupling between the SQUID and the input circuit is achieved via the mutual inductance M_i defined by

$$M_i = k\sqrt{LL_i} \tag{3.12}$$

with k the *coupling coefficient*. In reality the presence of the input circuit affects the SQUID inductance: because the characteristic times of the input circuit ($\tau_i = L_i/R_i$) are long compared to the Josephson period ($\tau_j = 1/\nu_j$) [13], currents induced from the SQUID into the input circuit persist over many Josephson oscillations and effectively

---

[11]Reproduced from Ref.[37].

[12]Stray and pickup coil inductances (L_s and L_p) can also be present in the input circuit.

[13]$L_i/R_i \approx 100ns$ and $\tau_j \approx 0.01ns$ for the SQUID used in this work
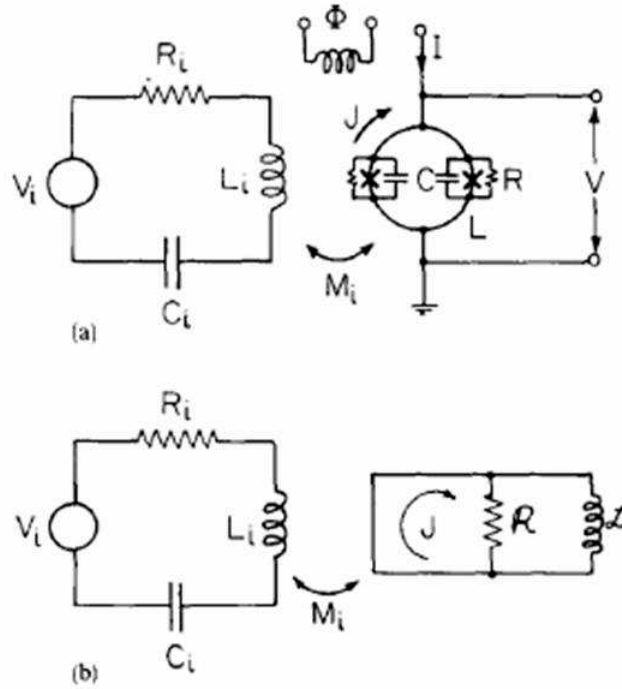
Figure 3.2: (a) SQUID plus tuned input circuit. (b) Dynamic SQUID input impedance. Reproduced from Ref.[37].

screen the SQUID inductance L to a *reduced* value [39, 44]:

$$L^r = (1 - k_e^2)L \qquad (3.13)$$

where k_e (*effective* coupling coefficient) can be defined - when stray (L_s) and pickup (L_p) inductances are also present - by the following expression:

$$k_e = k \left(\frac{L_i + L_s + L_p}{L_i} \right)^{-1/2} \qquad (3.14)$$

In the same strong coupling approximation (effective screening from the input circuit), the output SQUID voltage behaves in time as the output of an isolated

SQUID with an effective *quasistatic* bias flux Φ_e depending on the input circuit

currents maintained by the voltage source V_i, the input noise source, and the voltage

induced in the input by changes in the SQUID circulating current [44].

Figure 3.2(b) illustrates the SQUID dynamic input impedance $\mathcal{Z}$ expressed through

a dynamic inductance $\mathcal{L}$ and resistance $\mathcal{R}$ and defining the response current J to

an applied flux Φ [14]. Both $\mathcal{L}$ and $\mathcal{R}$ - in general different from the *bare* R and the

SQUID geometric L - depend on the SQUID bias current and flux and are moreover

also modified by the presence of the input circuit to their *reduced* values $\mathcal{L}^r$ and $\mathcal{R}^r$.

At the same time, while the total impedance of the *uncoupled* input circuit can

easily be expressed, in presence of a stray inductance L_s, as:

$$Z_T(\omega) = R_i + j\omega(L_i + L_s) + \frac{1}{j\omega C_i}, \tag{3.15}$$

the impedance of the input circuit *coupled* to the SQUID can be written in the

following form [39] accounting for the modification of R_i and L_i from the reflected

SQUID dynamic impedance:

$$Z_T^*(\omega) = R_i + \Delta R_i + j\omega(L_i + \Delta L_i + L_s) + \frac{1}{j\omega C_i} \tag{3.16}$$

with:

$$\Delta L_i = k_e^2 L \left(\frac{R_i}{\mathcal{R}^r} - \frac{1}{\omega^2 C_i \mathcal{L}^r} \right), \tag{3.17}$$

and:

$$\Delta R_i = k_e^2 L \left(\frac{R_i}{\mathcal{L}^r} + \frac{1}{C_i \mathcal{R}^r} \right). \tag{3.18}$$

By accounting for the reduced SQUID parameters and for the modification of

the input circuit by the presence of the SQUID, Martinis and Clarke [42] developed

---

[14]Also: flux-to-current transfer function J_Φ.

a signal and noise theory for a DC-SQUID amplifier expanding previous results from Tesche, Clarke and collaborators [41, 43, 44]. By expressing the amplifier voltage gain as [42] [15]:

$$G_V = \frac{V_{output}}{V_{\widetilde{input}}} = \frac{M_i V_\Phi^r}{Z_T^*} \tag{3.19}$$

where, with the term $V_{\widetilde{input}}$, a *modified* input voltage is considered, including both the voltage source V_i (if any), and the effect of the current noise in the input circuit producing an additional output voltage noise [42], [40].

Analogously, the power gain can be expressed as [40]:

$$G = \left| \frac{V_{output}}{V_{input}} \right|^2 \left(\frac{R_i}{R_{dyn}} \right) = \frac{M_i^2 (V_\Phi^r)^2 R_i}{(R_{dyn} |Z_T^*|^2)} \tag{3.20}$$

with R_{dyn} the dynamic output resistance of the SQUID.

Furthermore, the amplifier noise temperature can be defined by the following expression [40]:

$$T_N(\nu) = \frac{S_V(\nu)}{4 k_B R_i G_V^2}, \tag{3.21}$$

with $S_V(\nu)$ the SQUID output voltage noise spectral density.

Also, a useful expression for deriving the reduced flux-to-voltage transfer coefficient V_Φ^r from the output experimental noise spectra can be obtained [39], as described in the following.

From Hilbert and Clarke's data analysis, let us consider the SQUID output noise power spectral density $P_{output}(\nu_o)$ at the amplifier gain resonance ν_o, measured by a 50Ω impedance spectrum analyzer. The Nyquist noise in the input generates a

---

[15]Neglecting the loading of the SQUID output by the following amplifier stage, a valid approximation in the case of 50Ω input amplifiers.

voltage noise $\sqrt{4k_BTR_i}$, and hence on resonance a current noise $\sqrt{4k_BTR_i}/(R_i + \Delta R_i)$. This induces in the SQUID a flux noise $M_i\sqrt{4k_BTR_i}/(R_i + \Delta R_i)$ ultimately producing a SQUID output voltage $V_\Phi^r M_i\sqrt{4k_BTR_i}/(R_i + \Delta R_i)$.

The power mismatch η between the source (SQUID reduced dynamic resistance R_{dyn}^r) and the load (50Ω spectrum analyzer input impedance) is:

$$\eta = 1 - \left|\frac{(50 - R_{dyn}^r)}{(50 + R_{dyn}^r)}\right|^2. \tag{3.22}$$

As a consequence, the reduced flux-to-voltage transfer coefficient can be expressed by the following expression:

$$V_\Phi^r(\nu_o) = \frac{(R_i + \Delta R_i)}{M_i}\left[\frac{R_{dyn}^r P_{output}(\nu_o)}{4k_BTR_i\eta(BW)}\right]^{1/2}, \tag{3.23}$$

where BW the measurement bandwidth.

An interesting series of experiments was performed by Hilbert and Clarke to measure the dynamic input impedance of a SQUID coupled to a tuned input circuit [37], [39].

First the resonance $(2.94MHz)$ and resonance bandwidth (FWHM [16], $14.5KHz$) of the *unloaded* input circuit were determined with the SQUID biased with a large current $(I >> I_C)$, where inductive screening was negligible and the SQUID dynamic input impedance could be reasonably assumed to be $\approx 2\Omega$. Then the SQUID was biased at different operating (bias current and applied flux) points, and shifts in resonant frequency and bandwidth were recorded for every bias condition, resulting from the resonating voltage gain of the amplifier (Eq. 3.19), i.e. from the zeros of

---

[16]Full Width Half Maximum

the *coupled* impedance Z_T^* (Eq. 3.16).

Resonant frequency shifts were related to changes ΔL_i in the input inductance, while changes in the resonance FWHM were connected to ΔR_i (Eq. 3.15 and 3.16). Hence, *reduced* SQUID parameters could be derived from Eq. 3.17 and 3.18 [39].

Figure 3.3 [17] illustrates - as a function of Φ/Φ_o - the behavior of $L/\mathcal{L}^r$ and $R/\mathcal{R}^r$ and of the *reduced* voltage-to-flux transfer function V_Φ^r normalized to the *bare* SQUID flux-to-voltage transfer function $V_\Phi^{max} \approx R/L$ [18] at $T = 1.5K$ and for a bias current $(I/I_C)_{1.5K} \approx 1$.

From these and other data [36], [39] collected also at $T = 4.2K$ and for different I/I_C ratios [19] a series of information was derived and is here summarized:

1) As expected, the behavior of V_Φ^r presented maxima when the SQUID was biased at its maximum sensitivity point ($\Phi = (2n+1)\Phi_o/4$, with n integer). Moreover, the ratio V_Φ^r/V_Φ^{max} decreased with increasing bias current [20].

When the experimental curves were compared with simulations performed for a *bare* and a *reduced* SQUID [39], their shape and amplitude smoothly moved from a close resemblance to a simulated *bare* SQUID for higher bias currents, to a simulated *reduced* SQUID for lower bias currents, suggesting a more efficient inductive screening of the SQUID at lower currents.

2) The $L/\mathcal{L}^r$ behavior was also simulated for a *bare* and *reduced* SQUID, showing

---

[17]Reproduced from Ref.[37].

[18]The plot axis legends refer to the reduced values as verified from Ref.[39].

[19]At $T = 1.5K$ it was $I/I_C \approx 0.7, 0.85, 1$.

[20]For example, and as estimated from the published data plots in [39], at $T = 1.5K$ and $\Phi/\Phi_o = (2n+1)1/4$, it was $V_\Phi^r/V_\Phi^{max} \approx 2, 1.2$ and 0.7 for $I/I_C \approx 0.7, 0.85, 1$.
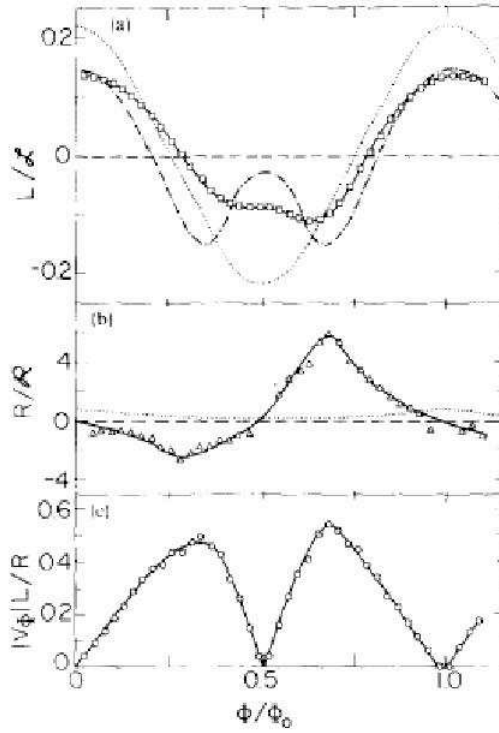
Figure 3.3: Normalized $\mathcal{L}^r$ (a); $\mathcal{R}^r$ (b) and V_Φ^r (c). The SQUID was at $T = 1.5K$, and biased at about $2I_o$. Reproduced from Ref.[37].

$L/\mathcal{L}^r$ small near $\Phi = (2n + 1)\Phi_o/4$ and reasonably agreeing with the experimental data for different bias current ranges.

3) Data related to $R/\mathcal{R}^r$ showed a strong disagreement with the simulations [39], and a capacitive feedback model was proposed and tested to explain the mechanism responsible for the measured changes ΔR_i of the input resistance R_i. It was in fact assumed that a feedback from the output of the SQUID was affecting the change of R_i through a distributed parasitic capacitance between the SQUID and the input circuit. A model was introduced where the distributed capacitance was replaced

37

with a lumped capacitor, and it accounted for the measured changes in R_i within a factor of two, compatible with the lumped capacitor approximation and variations in the individual SQUIDs used in the experiments. Moreover the parasitic capacitance, when present, was also considered responsible for the reduction of the inductive screening of the SQUID loop at the higher Josephson frequencies, where also steps in the IV characteristics were observed.

3.3 DC-SQUID shot noise-limited detection of an SET: engineering the scheme

In the course of this work, the shot noise-limited detection of a Single-Electron Transistor through a DC-SQUID was approached as an impedance and noise matching problem, and is presented in the following sections.

3.3.1 Input and output impedance matching

When engineering the read-out of a SET by a SQUID, the first issue to deal with was the impedance mismatch between:

A. the source ($R_{SET} \approx 50 - 100K\Omega$) and the low impedance SQUID amplifier ($R_{input}^{SQUID} << R_K$ [21]);

B. the SQUID output impedance ($\approx$ few Ω) and the following 50Ω room temperature amplifier.

---

[21]R_K is the resistance quantum $\approx 25.8K\Omega$.

Matching networks were designed around the chosen operating frequency ($\approx 10 MHz$[22])

by neglecting in first approximation any modification of the *bare* SQUID parameters by the mutual interaction between the input circuit and the SQUID that was introduced in the previous section based on the work of Hilbert and Clarke works [36, 37, 39]. Under this assumption:

A. The system (SQUID+input coil) equivalent circuit is presented in Fig. 3.4(a), where the SQUID and input circuit inductances (L and L_i) and shunt resistors R_S are also represented [23].

Figure 3.4(b) illustrates the system input impedance obtained after a simple network analysis was performed. The input impedance is represented by the following term [24]:

$$Z_{in} = \frac{\omega^2 L L_i k^2}{R_S} + i\omega L_i, \tag{3.24}$$

where k is the coupling constant defined as in Eq.3.12 and $\omega^2 L L_i k^2 / R_S$, the real component of the input impedance is going to be named R_{SQUID}^{eff}.

B. The output impedance (Fig. 3.4(c)) is represented by the SQUID shunt resistor R_S.

---

[22]Reminder: the device working frequency was chosen in relation to the frequency range of resonances in nanomechanical beams previously studied in Schwab's group (see Chapter 2).

[23]SQUID parameters were assumed to be in the range of the SQUIDs available for this experiment: $L \approx 100pH$, R_S was supposed $\approx 2\Omega$, $k^2 \approx 0.8$. The SQUID input inductance L_i was the unknown parameter and had to be determined from the design engineering considerations.

[24]It is important to stress again that Eq. 3.24 represents, in terms of the Hilbert and Clarke analysis [39], an approximation rigorously valid only when the inductive screening is negligible and therefore the SQUID dynamic impedance is about R_S, with the SQUID is in its resistive state, i.e. biased with a large current ($I >> I_C$).
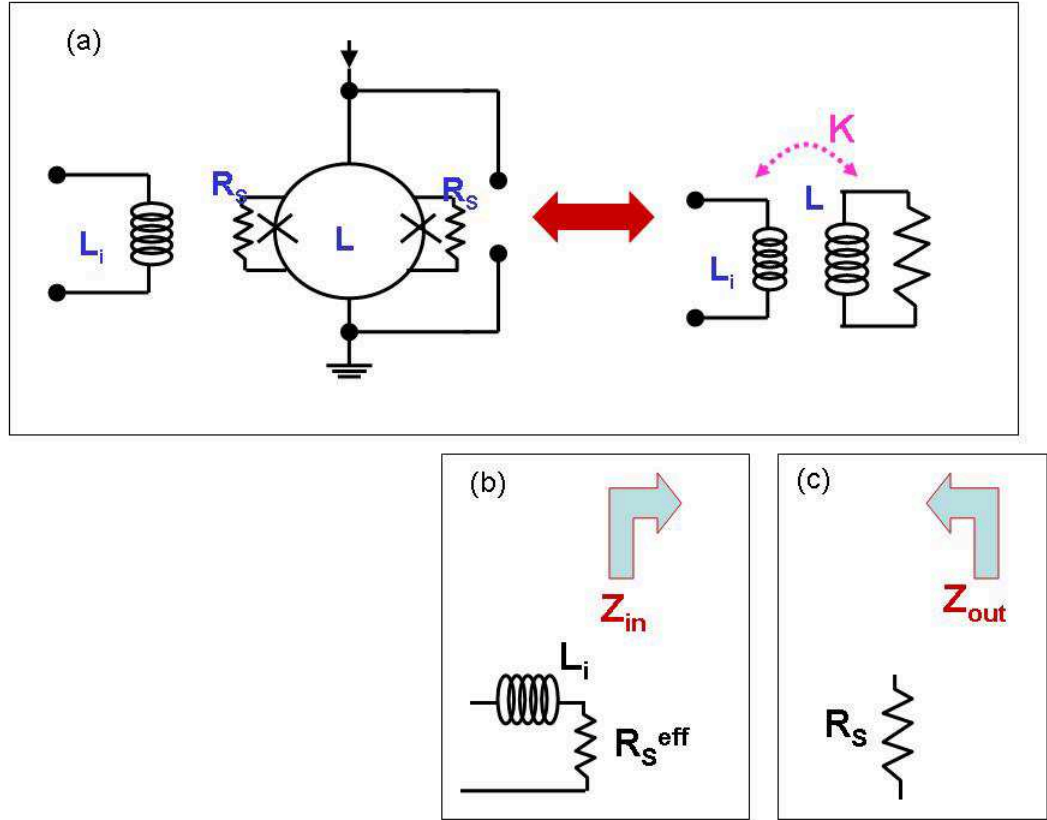
Figure 3.4: (a) Equivalent circuit of the system SQUID+input coil. (b) and (c) Schematic of the input and output impedances.

Therefore:

A. Input impedance matching: a network was needed to match a real impedance (R_{SET}) into a complex one (Z_{in}), and the choice was made to fully resonate the inductive part of the input impedance through a network section, and then proceed to match the two different resistive parts *via* another matching LC section built to conserve the DC connection [45]. Fig. 3.5 illustrates the full resonant approach taken with the SQUID-side and the matching sections, both resonating at the device operating frequency (10MHz) and having quality factors Q_2 and Q_1 respectively.

B. Output impedance matching: furthermore, a network was required to match the device output impedance ($\approx$ few Ω) to the 50Ω impedance of a room temperature amplifier. This was similarly accomplished by an LC matching section with quality factor Q_3 [45] (Fig. 3.6).
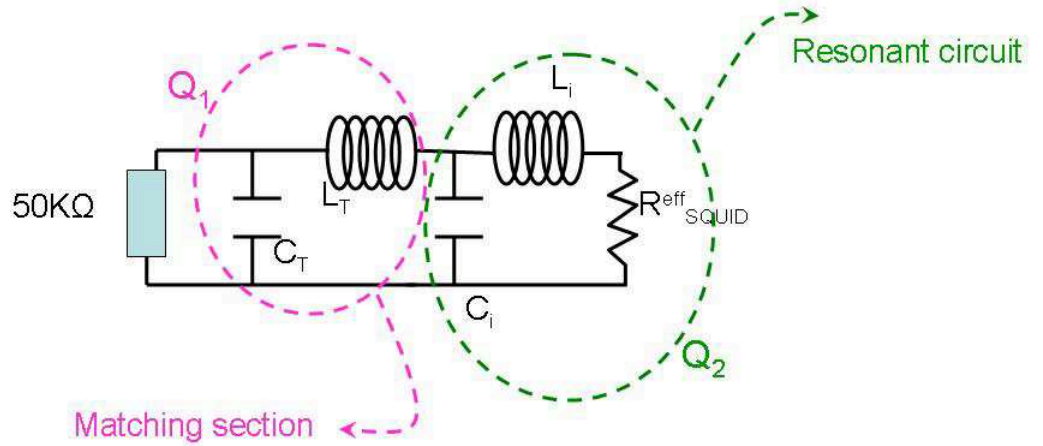
Figure 3.5: Full resonant approach scheme to match R_{SET} into the device Z_{in}.

Supposing the SQUID shunt resistors to be $\approx 2\Omega$, and choosing $L'_T = 108nH$ and $C'_T = 2.2nF$ [25], it follows that $Q_3 = (1/R_S)\sqrt{L'_T/C'_T} \approx 3$ and Z_c, the network

[25]In the calculation the network components are chosen with the same values as the ones used to build the device, see Tables 4.2 and 4.3, Section 4.1.2.
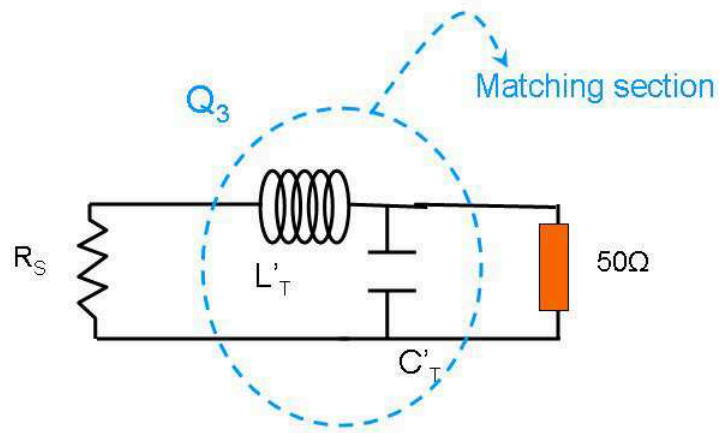
Figure 3.6: Matching scheme from the device output impedance to 50Ω.

characteristic impedance, is approximately 7Ω [26]. Moreover at the network resonant frequency the equivalent impedance $(Z_o(\omega_o) = Z_c^2/R_S)$ was calculated to be about 25Ω, moving the power mismatch factor [27] from $\eta \approx 0.15$ for the unmatched case (corresponding to a mismatch loss [28] $ML \approx -8.3dB$), to $\eta \approx 0.89$ ($ML \approx -0.5dB$).

---

[26]It is: $Z_c = \sqrt{L'_T/C'_T}$.

[27]See Eq. 3.21.

[28]$ML = 10 \lg \eta$.

3.3.2 Noise matching at the input

The input (and output) impedance matching was not the only condition that needed to be fulfilled to engineer the device. Supposing an efficient matching was performed at the input, an equivalent circuit could be introduced (Fig. 3.7), R''_{SET} being the SET resistance after going through the two matching networks as explained in the following.
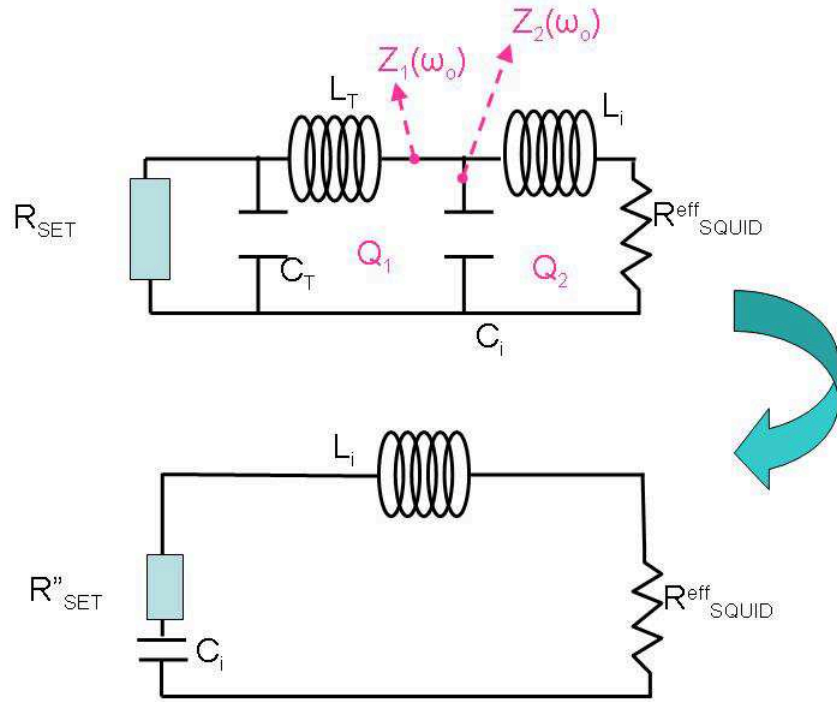
Figure 3.7: Two-section matching network and its equivalent circuit. $R''_{SET} = R_{SET}/Q_1^2Q_2^2$ is the transformed SET resistance.

By introducing the network section's characteristic impedances $Z_{C1} = \sqrt{L_T/C_T}$ and $Z_{C2} = \sqrt{L_i/C_i}$, on resonance the SET resistance transforms through the double

section network into:

$$R'_{SET} = Z_1(\omega_o) = \frac{Z_{C1}^2}{R_{SET}}$$

$$R''_{SET} = Z_2(\omega_o) = \frac{Z_{C2}^2}{R'_{SET}}, \tag{3.25}$$

where $Z_1(\omega_o)$ and $Z_2(\omega_o)$ are the sub-network's equivalent impedances at the resonant frequency ω_o [29].

The equivalent circuit is expressed in Fig. 3.8 in terms of the voltage (Nyquist) noise generated by the source and by the amplifier load whose spectral densities are $(S_V)_{source} = 4K_B T_{SET}^{eff} R''_{SET}$ and $(S_V)_{load} = 4K_B T_{SQUID} R_{eff}^{SQUID}$ respectively. In the hypothesis that the SET noise is dominated by the shot noise [30], an *effective* SET temperature (T_{SET}^{eff}) was derived by equating the SET shot noise-generated voltage noise $\sqrt{S_V} = \sqrt{2eI}R_{SET}$ [31] to an *effective* Nyquist noise produced at the temperature T_{SET}^{eff} [32].

In order to have the equivalent circuit current noise dominated by the source (R''_{SET}) and not by the amplifier load (R_{eff}^{SQUID}) the following relation was added to the design requirements:

$$\sqrt{4K_B T_{SET}^{eff} R''_{SET}} >> \sqrt{4K_B T_{SQUID} R_{eff}^{SQUID}} \tag{3.26}$$

Equation 3.26, together with the previously stated relations between parameters of the input network, provided the starting point to determine the value of the

---

[29]Also, it is possible to express $R''_{SET} = R_{SET}/(Q_1^2 Q_2^2)$, with Q_1 and Q_2 being the quality factors $(Q = Z_C/R)$ of each subnetwork.

[30]$eV_{DS} > k_B T$, with V_{DS} the SET drain-source voltage.

[31]For a SET biased very near the blockade threshold [10].

[32]As an estimate, when considering a current through the SET $I_{DS} \approx 1nA$, it results $T_{SET}^{eff} \approx 350mK$.
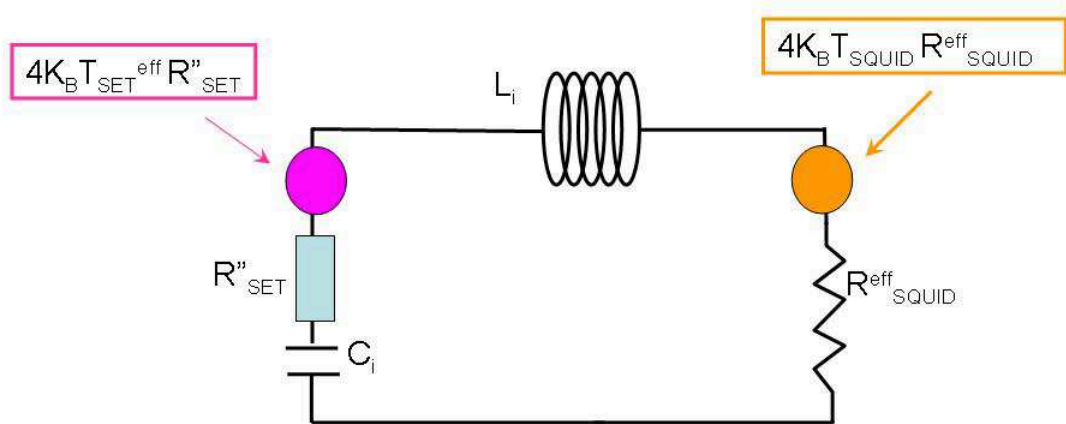
Figure 3.8: Voltage noise sources in the input equivalent circuit.

input inductor (L_i) and the circuit components.

When choosing $L_i \approx 10nH$, and preliminarily imposing $Q_1 \approx 150$, $Q_2 \approx 3$, [33] it was possible to determine the remaining components for the input circuit network (operating at frequency $\omega_o/(2\pi) \approx 10MHz$). When moving from the estimated values to commercial components (see Tables 4.2 and 4.3) the following nearest-values were chosen:

[33]As reasonably attainable quality factors when using commercial, surface-mount parts. The additional constraint in the choice was to push the self-resonant frequencies of inductive components outside the frequency range of interest.

$C_i = 30nF$

$L_T = 10\mu H$

$C_T = 18pF.$

From where it resulted:

$Z_{C1} \approx 745\Omega$ and $Z_{C2} \approx 1\Omega$;

$R'_{SET} \approx 10\Omega$ and $R''_{SET} \approx 0.1\Omega$;

$Q_1 \approx 70$ and $Q_2 \approx 10$;

$R^{eff}_{SQUID} \approx 1m\Omega.$[34]

3.3.3 Design evaluation/Top-of-the-fingers estimates

It is easy to verify that the above values could fulfill the condition set by Equation 3.26. Also, a simple top-of-the-fingers calculation could provide a rough estimate of the flux noise amplitude related to the device design. Starting from the voltage noise generated at $T = 250mK$ by R''_{SET} in the input equivalent circuit and amplified on resonance by a factor $Q_2 \approx 6$, the current noise amplitude could be determined as $\sqrt{S_I^{input}} = Q_2\sqrt{4K_B T^{eff}_{SET} R''_{SET}}/R''_{SET} \approx 80pA/\sqrt{Hz}$. From $\sqrt{S_I^{input}}$ and the value of the mutual inductance as defined by Equation 3.12 ($M_i \approx 1nH$), it was possible to estimate the flux noise generated in the SQUID by the designed input circuit: $\sqrt{S_\Phi^{input}} = M_i\sqrt{S_I^{input}} \approx 40\mu\Phi_o/\sqrt{Hz}$.

This value could be compared to the *intrinsic* SQUID flux noise (noise floor), that could be expressed through the following contributions:

---

[34]From $R^{eff}_{SQUID} = \omega^2 L L_i k^2/R_S$ and supposing $L \approx 100pH$, $L_i \approx 10nH$, $k \approx 0.8$ and $R_S \approx 2\Omega$.

(a) Nyquist noise of the SQUID shunt resistors generating a voltage noise power $\sqrt{16K_BTR_S} \approx 10pV/\sqrt{Hz}$ at $T = 250mK$, hence a current noise $\sqrt{S_I^{SQUID}} = \sqrt{S_V^{SQUID}}/R_S \approx 5.3pA/\sqrt{Hz}$ from where a flux noise $\sqrt{S_\Phi^{SQUID}} = L\sqrt{S_I^{SQUID}} \approx 0.3\mu\Phi_o/\sqrt{Hz}$ could be calculated.

(b) *Backwards* noise term due to the current noise around the SQUID loop $\sqrt{S_I^{SQUID}}$ as calculated in point (a), producing a voltage noise into the (equivalent) input circuit on resonance equal to $Q_2\omega M_i\sqrt{S_I^{SQUID}}$, generating in turn (at resonance) a current noise $Q_2\omega M_i\sqrt{S_I^{SQUID}}/R_{SET}''$ ultimately inducing a flux into the SQUID equal to $Q_2\omega M_i^2\sqrt{S_I^{SQUID}}/R_{SET}'' \approx 10\mu\Phi_o/\sqrt{Hz}$, [35]. In conclusion, according to these estimates, the engineered detection scheme should be able to detect a $50K\Omega$ source with a signal-to-noise ratio greater than 1.

---

[35]Point (b) follows an argument presented in Ref.[36], p.11. Absolute values have been reported for simplicity.

Chapter 4

Device realization and measurement set up

Throughout this thesis a *device* is defined by a SQUID chip and its circuitry mounted in a box and thermally anchored to the 300mK stage of the He$_3$ refrigerator. In this chapter the device realizing the proposed detection scheme is described together with the measurement equipment and set-up. The SQUID chip and its circuitry will be introduced in Sec. 4.1.1 and Sec. 4.1.2 respectively. The wiring of the fridge and the room temperature measuring circuitry will be described in Sec. 4.2.1 and Sec. 4.2.2.

4.1 The device

4.1.1 The device: SQUID chip

When an external signal needs to be coupled to the SQUID inductance, this is configured through a multi-turn input coil of inductance L_i and of mutual inductance M_i to the SQUID. The actual SQUID chips used in this work were designed and fabricated in the late 1980s by Dr. Mark Ketchen and collaborators [1]. In order to achieve tight inductive coupling between the SQUID loop and the input coil the design used a planar coupling scheme between thin-film structures [46, 47] first

---

[1]IBM T.J. Watson Research Center

introduced on a SQUID in 1979 by Dettmann, Richter, Albrecht and Zahn [48].

Fig. 4.1 illustrates one of the chips utilized in this thesis, with three SQUID devices [2] (n=15, 70 and 100 input coil turns, not visible in the picture) and two gradiometers (not used in this work).

The inductive loop of the SQUIDs of this thesis (Fig. 4.2 and Fig. 4.3) consists of a Niobium superconducting square washer with a slit from the central hole to its outer edge where two Nb-AlO$_x$-Nb Josephson junctions are placed away from the higher field region near the center hole [59] , [60], [61]. The washer is electrically insulated from (but magnetically tightly coupled to) an n-turn planar spiral input coil, and it acts as the single turn secondary of a thin-film transformer, while the input coil acts as a multi-turn primary fabricated directly underneath it [59].

While excellent coupling can been achieved through this planar scheme, care had to be taken in the design of thin-film dc SQUIDs to account for the parasitic capacitance C_p across the SQUID inductance, leading to resonances coupled with the SQUID dynamics and possibly degrading its energy resolution. Moreover, a microstripline is formed by the input coil with the SQUID loop as ground plane introducing high-Q resonances that, in turn, introduce irregularities in the I-V and V-Φ characteristics leading also to excess noise [49]. Data and simulations from Ryhanen *et al.* [50] showed that optimal energy resolution was achieved for $C_p << C$ (C being the SQUID junction's self-capacitance), and in order to minimize C_p different solutions have been proposed [51, 52, 53]. For instance, SQUIDs have been fabricated with the Josephson junctions near the hole of the washer instead of near

---

[2]The three square washers with a square hole in the center.
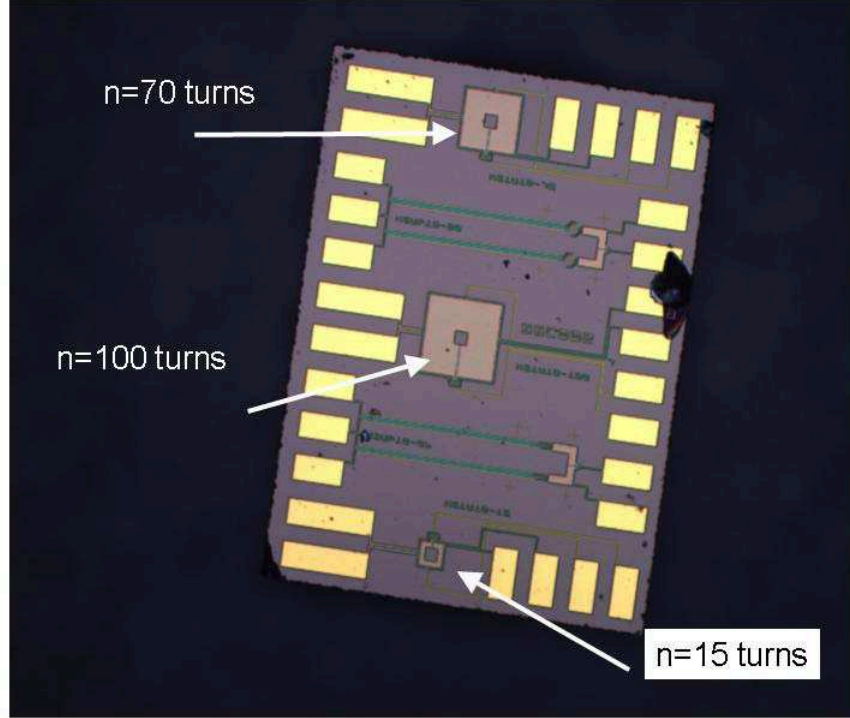
Figure 4.1: SQUID chip, including three SQUID devices (n=15, 70 and 100 input coil turns, not visible at the image magnification) and two gradiometers (not utilized in the course of this work). Calling W the size of the SQUID washer and d the size of its central hole, it is: W=90μm, d=50 μm (n=15 turns); W=220 μm, d=50 μm (n=70 turns); W=300 μm, d=50 μm (n=100 turns).

its edge, thus eliminating the parasitic capacitance [51].

An alternative, using sub-μm line-width input coils, allowed for a more compact SQUID layout with reduced parasitic capacitance while achieving a tight coupling, as demonstrated by Ketchen *et al.* [54, 55].

In addition, to assure a non hysteretic behavior in the current-voltage SQUID characteristics, shunt resistors ($\approx$ few Ω) are placed across each junction (Fig. 4.3).
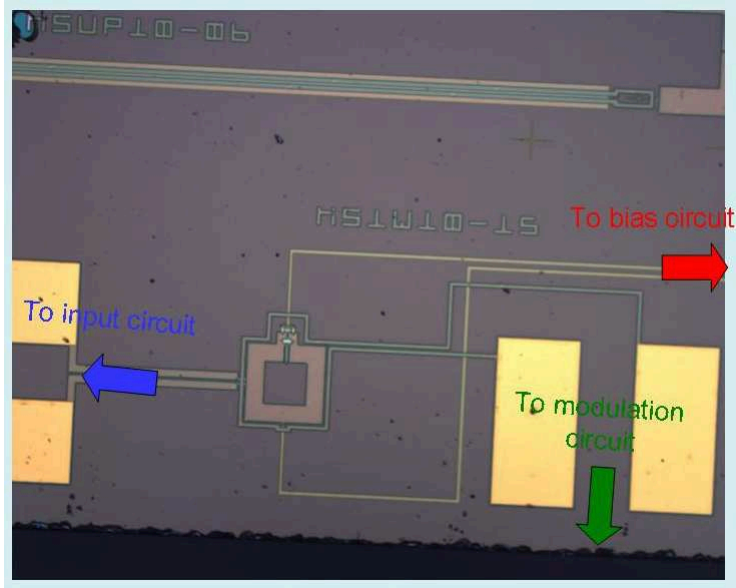
Figure 4.2: Detail of the n=15 turn input coil SQUID: leads to the wiring pads.

Moreover, in order to achieve a well-behaved voltage-to-flux characteristic, a damping resistor is also placed across the SQUID inductance (Fig. 4.3), to damp the washer resonances and smooth the SQUID characteristics. The value of the damping resistor was chosen such that its thermal noise does not contribute significantly to the device flux noise [56, 57, 58].

In the SQUID geometry just presented, the signal to be measured is transformed into a current flowing in the input coil (of inductance L_i) and generates a magnetic flux that tightly couples to the SQUID loop (whose inductance is dominated by the washer's inductance L) via a mutual inductance term M_i. A coupling constant can then be defined [3] as

$$k^2 = \frac{M_i^2}{LL_i}. \tag{4.1}$$

___
[3]The coupling constant has already been introduced in Chapter 3
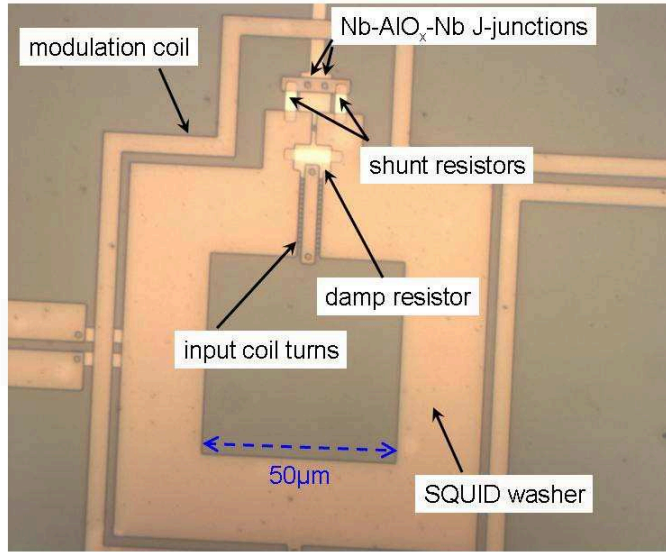
Figure 4.3: Detail of the n=15 turn input coil SQUID. The SQUID washer dimensions are W=90μm-outer square size, and d=50 μm-hole size. The input coil turns are barely visible underneath the washer's slit.

Moreover, a control current I_{mod} can be applied through a single turn coil (modulation coil, Fig. 4.3) around the SQUID washer with the purpose of adjusting the flux bias point and/or to modulate the SQUID along the voltage-flux (V-Φ) curve [54]. For example, in the so-called *small-signal mode* operation that has been used through this work, the SQUID was DC-biased at its optimum working point, on the steepest part of the $V - \Phi$ characteristics, and a small oscillating flux of amplitude $\delta\Phi \approx 10 - 100 m\Phi_o$ was sent through the modulation coil, producing an output voltage $\partial V = \partial\Phi V_\Phi$, with V_Φ the flux-to-voltage transfer coefficient at the working point [30].

A series of useful expressions to calculate the SQUID parameters (washer inductance L, input coil inductance L_i, mutual inductance M_i and coupling constant k) can be found in Refs. [30], [56] and [61] for different SQUID washer geometries and is in the following summarized for the purpose of this work.

The inductance of the SQUID washer can be expressed by the sum of three terms: L_h (inductance of the hole), L_{sl} (inductance of the slit), and the parasitic junction inductance L_{jp} - usually negligible (of the order of few pH):

$$L = L_h + L_{sl} + L_{jp}. \tag{4.2}$$

Numerical simulations [59] showed that, since in a square-shaped SQUID loop with hole size d and width $w = (W-d)/2$ the current distribution is strongly peaked near the central hole, L_h has the following limiting value once $w \geq d$:

$$L_h \approx 1.25\mu_o, \tag{4.3}$$

where $\mu_o = 4\pi \times 10^{-7} NA^{-2}$ is vacuum permeability.

Moreover, a numerical analysis of the slit inductance L_{sl} as a two-dimensional structure has found it is weakly dependent on the slit geometry and with an inductance per unit-length L_{sl}^l [56]

$$L_{sl}^l = 0.3pH/\mu m. \tag{4.4}$$

Also, it is possible to show that for an n-turns input coil the expressions for M_i and L_i are given by:

$$M_i = n\left(L_h + \frac{L_{sl}^l l}{2}\right) \tag{4.5}$$

$$L_i = n^2\left(L_h + \frac{L_{sl}^l l}{3}\right) + L_s, \tag{4.6}$$

where l is the length of the slit, and L_s is the inductance of the stripline defined by the washer and the input coil. The upper bound for L_s can be determined through application of Ampere's law to the cross section of the washer

$$L_s = n^2 L_h \pi \frac{d+w}{d} \left(\frac{s + \lambda_1 + \lambda_2}{w} \right), \tag{4.7}$$

with λ_1 and λ_2 the superconducting penetration depths of the coil and the washer respectively, and s the separation between the washer and the coil. By using the set of equations 4.1-4.7 together with the values $\lambda_1 = \lambda_2 = 0.086 \mu m$ [4] and $s = 0.15 \mu m$ used in Ref. [56], it is possible to give an estimate of the following parameters for the different (uncoupled, i.e. *bare*) SQUIDs available as illustrated in Table 4.1. According to the requirements for the detection scheme as engineered in Section 3.3.2 ($L_i \approx 10nH$), a 15-turns input coil SQUID was chosen to be used in the experimental realization of the device.

4.1.2 The device: SQUID circuitry

A circuit board was designed for the purpose of this experiment, then produced and gold-plated by Sierra Proto Express, CA. The board was accomodated inside a home-made lead box ($3.5 \times 3.5 cm^2$). Mechanical stability of the board and electrical connection to the box ground were achieved with few drops of silver-paint on the

---

[4]The value given for $\lambda_2 = 0.086 \mu m$ in Ref. [56] is different, and almost twice from that determined in past work using Niobium thin superconducting films, both from a BCS dirty-limit estimate, and from experimental data. See $\lambda \approx 0.035 - 0.050 \mu m$ in [63]

n	d (μm)	w (μm)	L_h (pH)	L_{sl} (pH)	L (pH)	M_i (nH)	L_s (nH)	L_i (μH)	k^2
100	50	125	78	38	116	18	150	3.4	0.82
70	50	85	78	26	104	7	30	0.56	0.84
15	50	20	78	6	84	1	2.5	0.020	0.59

Table 4.1: Washer inductance L, input coil inductance L_i, mutual inductance M_i and coupling coefficient k for the SQUIDs in Fig. 4.1 according to Eq. 4.1 to Eq. 4.7.

board metalized bottom side (connected to the top ground pads through metalized drilled holes), and with some small Indium fragments pushed in between the board and the box edges. SMA snap-in connectors were then inserted into the box fitting holes, fixed with some drops of low-temperature glue and then soldered to the board leads for external connections. The device circuitries were obtained by soldering small surface-mount (SMT) components (thick film SMT resistors, inductors and capacitors) to the board. Capacitors were chosen to be ceramic NPO [5] because of their stability at low temperature. Nevertheless, a shift in capacitance between room temperature and 4K was recorded when measuring the resonant frequency of LC circuits mounted on a test board on a He$_4$ dip probe and it is shown in Fig. 4.4 - as an example - for the $10\mu H$-18pF section of the input coil circuitry. These tests were performed to ensure that the resonant frequencies at low temperature were

_____

[5]Negative-Positive-Zero, meaning that the negative and poitive temperature coefficients of the capacitors are zero, within the featured tolerance.

within the frequency range of interest.
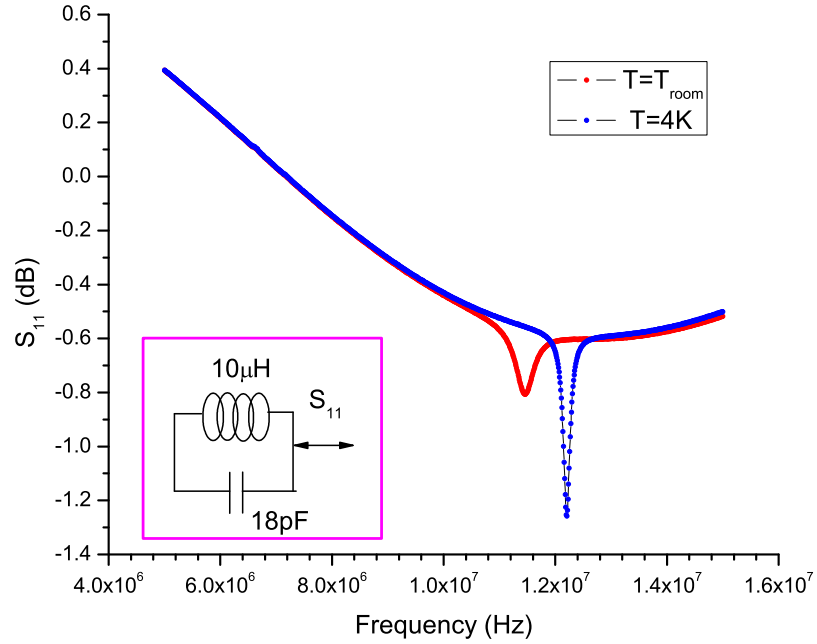
Figure 4.4: Reflectivity measurement of the $10\mu H$-18 pF section of the input circuit at $T = T_{room}$ and T=4 K, ungrounded. The input power from the network analyzer was -20dBm.

Part numbers for inductors and capacitors used in this thesis are listed in Tables 4.2 and 4.3.

Finally the SQUID chip was glued to the board central ground pad by a small drop of PMMA resist and it was then wire-bonded to the box circuits pads with 0.001" aluminum wire. The SMA connectors on the device box were numbered as in the following:

1- SQUID bias circuitry

2- Device output circuitry

56

3- SQUID modulation coil circuitry

4- SQUID input coil circuitry

L	Part number	from
3 nH	1008HQ3N0XJLB	Colicraft
15 nH	1008HT-15NTJLB	Coilcraft
108 nH	0805LS-111XJBB	Coilcraft
$10\mu H$	IMC-1210	Vishay-Dale

Table 4.2: Values and part numbers for inductors used in this work.

C	Part number	from
$18pF$	C1206C180J5GAC-TU	Kemet
$22pF$	C0805220J56AC-TU	Kemet
$2.2nF$	VJ1206-A222JXAMT	Vishay-Vitramon
$4.7nF$	C1210C472J5GA	Kemet
$0.01\mu F$	C1206C103J3GA-TU	Kemet

Table 4.3: Values and part numbers for capacitors used in this work.

Then the device box was closed with a home-made Niobium lid for magnetic field shielding (Fig. 4.5) tightened with mini-screws, and lined on its inner side by a thin layer of Kapton tape to prevent accidental shorts with some of the surface-

mount components. The whole package was finally sealed with lead adhesive tape as additional shielding against magnetic fields (Fig. 4.6).

Figure 4.5: Sample box closed by niobium lid.
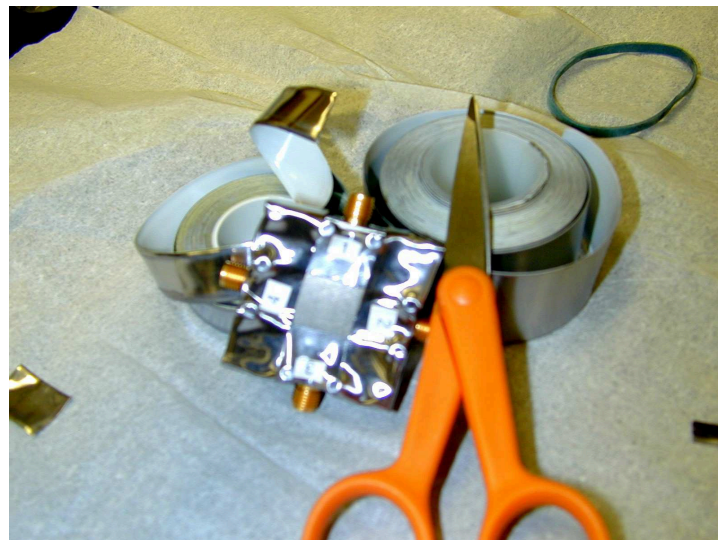
Figure 4.6: Sample box sealed by lead adhesive tape.

The box and circuitry for Device (3.0) are presented in Fig. 4.7 and Fig. 4.8. Device (3.0) was damaged during wire-bonding, and the same components and geometry were used for Device (4.0).
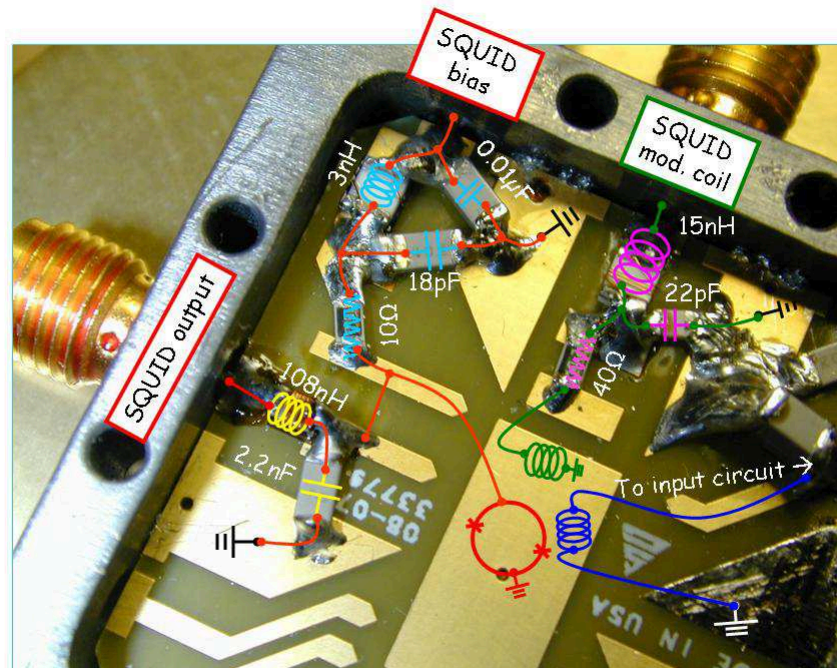
Figure 4.7: Device 3.0 box: detail on SQUID bias, SQUID output and SQUID modulation coil circuits. The SQUID is represented through a colored schematics: SQUID loop (red), modulation coil (green) and input coil (blue).

The board includes the double matching circuit at the SQUID input and the output matching to 50 Ω according to Section 3.3 design. [6] The SQUID chip, here represented by a colored schematics (see caption in Fig. 4.7), would sit in the center ground pad.

---

[6]Note that the output circuit in Fig. 4.7 has a wrong (inverted) disposition of its components. The arrangement was corrected after the picture was taken.
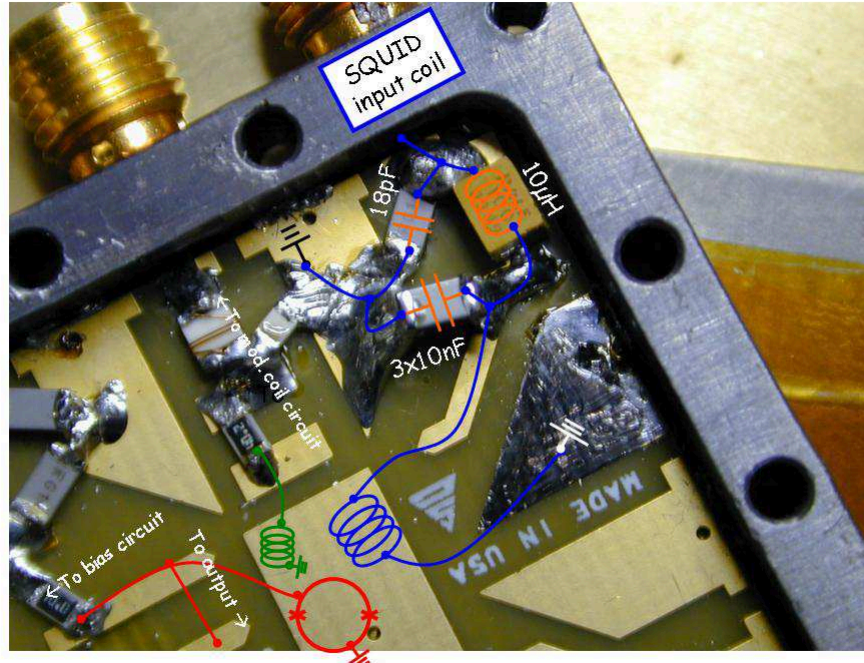
Figure 4.8: Device 3.0 box and components: detail on the SQUID input coil circuit.

The detection scheme also included the networks at the SQUID bias and modulation coil circuits, filtering frequencies above 1MHz and 180MHz respectively, as illustrated by PSpice [7] simulations of the modulation and SQUID bias circuits schematically represented in Fig. 4.9 and Fig. 4.10. Those circuits have further been implemented by room temperature filter boxes that will be described in the following section.

Figure 4.9 shows the schematic diagram of the modulation coil circuit as expressed by a set of lumped elements, and the result of the PSpice simulation of the attenuation (in dB) of the circuit in logarithmic plot with a 3dB cutoff frequency of about

---

[7]Orcad PSpice student version, Release 9.1

180MHz.

Fig. 4.10 shows the schematic of the SQUID bias circuit, where the SQUID is expressed by the parallel of its shunt resistors ($\approx 2\Omega$ each), and the simulated attenuation (in dB) *versus* frequency in logarithmic scale with a 3 dB cutoff frequency of about 1MHz.
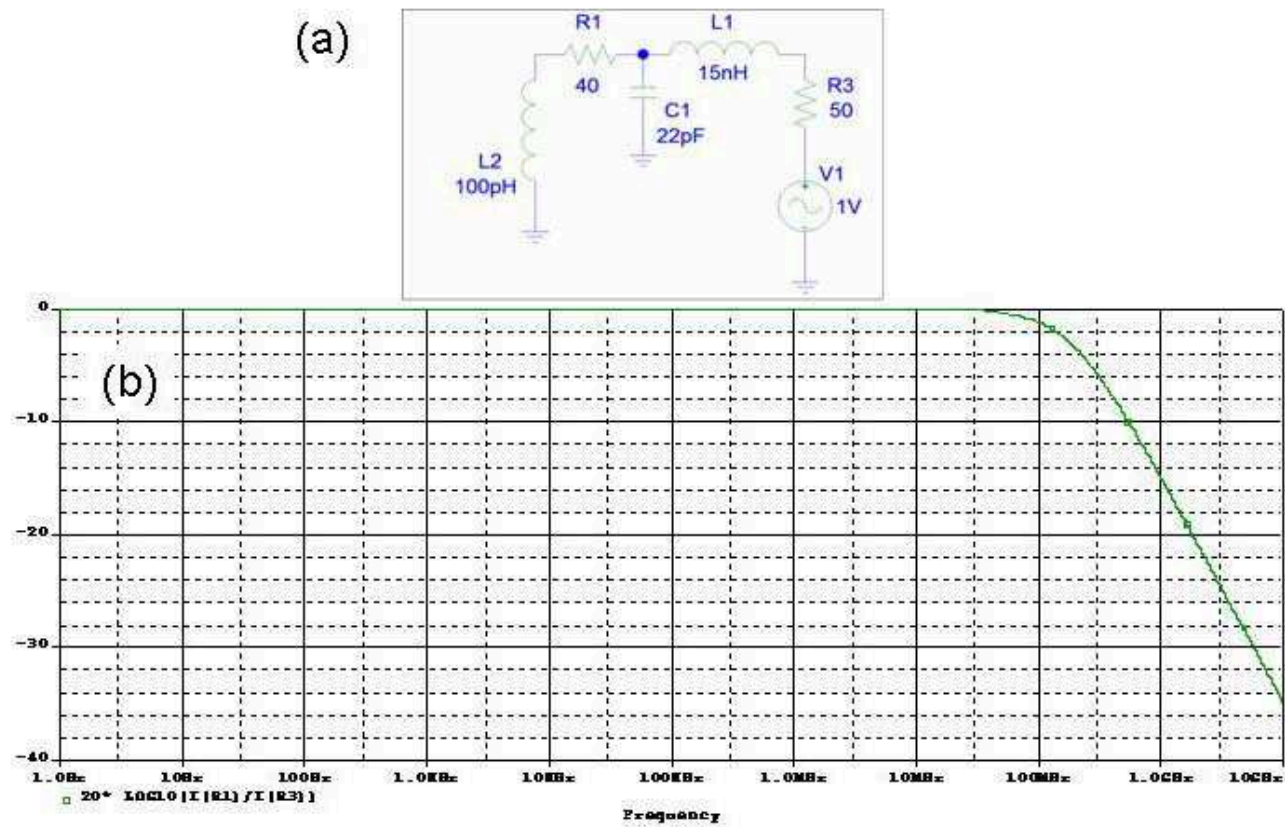
Figure 4.9: (a): Schematic of the modulation coil circuit expressed by a set of lumped elements. Resistances are expressed in Ohms. (b): PSpice simulation of the attenuation (in dB) of the modulation coil circuit. The vertical axis represents the circuit attenuation expressed in dB. The 3 dB cutoff frequency is located at about 180 MHz.
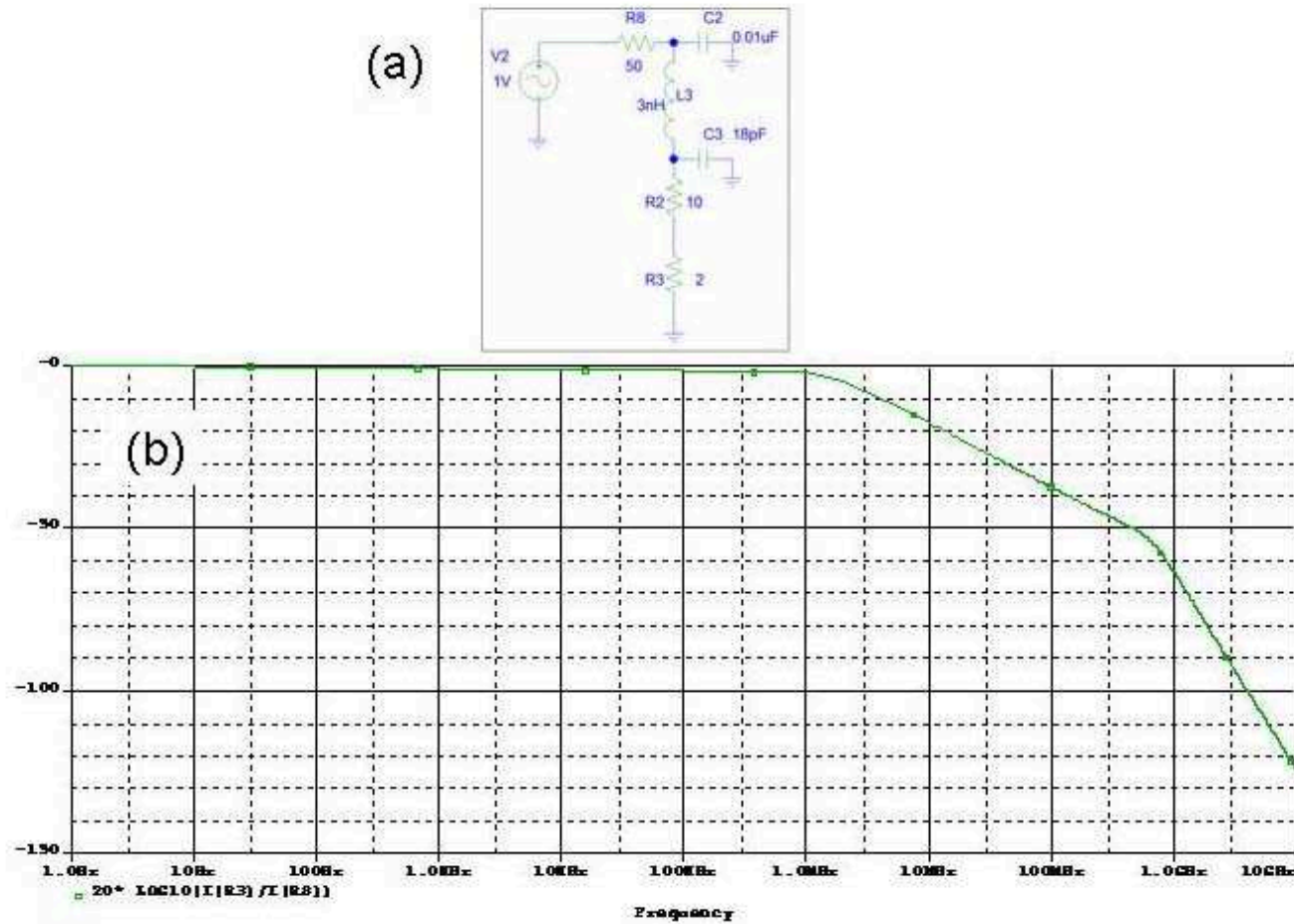
Figure 4.10: (a): Schematic of the SQUID bias circuit expressed by a set of lumped elements. Resistances are expressed in Ohms. (b): PSpice simulation of the attenuation (in dB) of the bias circuit as a function of frequency in logarithmic scale. The vertical axis represents the circuit attenuation expressed in dB. The 3 dB cutoff frequency is located at about 1 MHz.

4.2 The apparatus

4.2.1 The apparatus: ^{3}He refrigerator and its wiring

The *device* was thermally fixed to the 300 mK stage of a ^{3}He fridge [8] (Figs. 4.11 and 4.12) operating inside a 45 L helium dewar [9]. The wiring of the fridge is illustrated in Fig. 4.13.

The temperatures of the charcoal sorption pump and 1K pot were measured by silicon diode thermometers, while the temperature of the ^{3}He pot was measured by a RuO_2 thermometer. Wires for all the thermometers and heaters were connected to a 19-pin electrical feed-through on the IVC pumping port. All wires were made of insulated copper and were thermally anchored onto copper spools installed at 4.2K. Wires for the RuO_2 thermometer were also thermally anchored on the copper spool installed on the 1K pot, and from there they connected to the ^{3}He heater [62].

From room temperature to the base temperature stage, signals for the SQUID bias, SQUID modulation and input circuits were transmitted through stainless steel coaxial cables, thermally anchored at 4K and connected to a series of two home-made powder filters [64] anchored at 1.4K and 300mK respectively. The filters were built in banks of four, each filter consisting of a RF-tight, Au-plated Cu box containing a copper wire wound in a spiral and embedded into a mix of epoxy resin and grain copper powder in equal weight proportions as previously described [23].

---

[8]Janis model HE-3-SSV

[9]Kadel Inc.
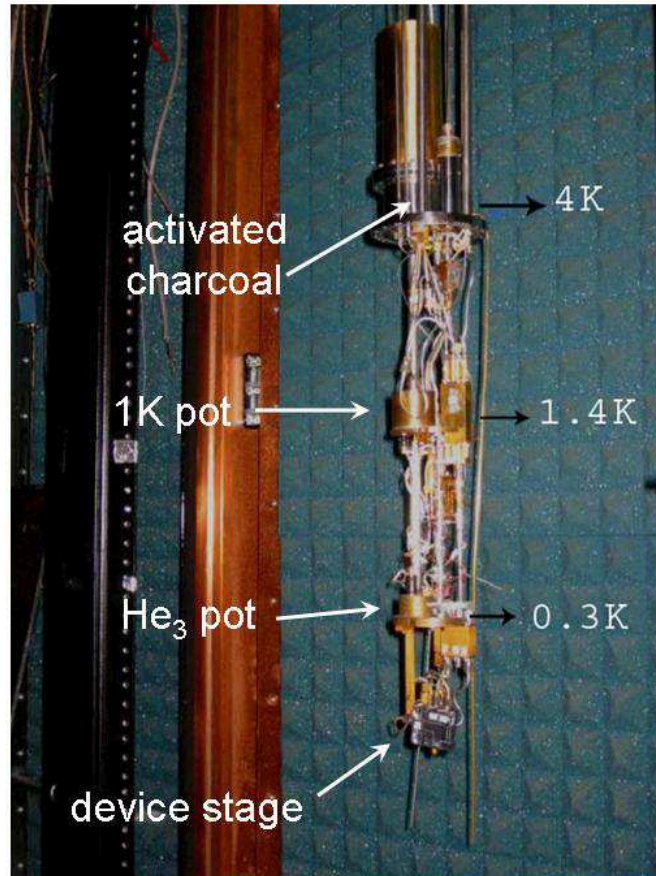
Figure 4.11: ^{3}He refrigerator.

The device output was directed, after a small section of stainless steel flexible coaxial line, through a niobium semi-rigid coaxial cable, into a series of two heat sinks anchored at 300mK and 1.4K and then directed toward the 4K stage through another section of stainless steel flexible cable. The heat sinks, with the purpose to thermalize the inner conductor of the coaxial cable, consisted of home-built 50Ω microstrip lines, Au on a quartz substrate for the heat sink at 300mK, and of
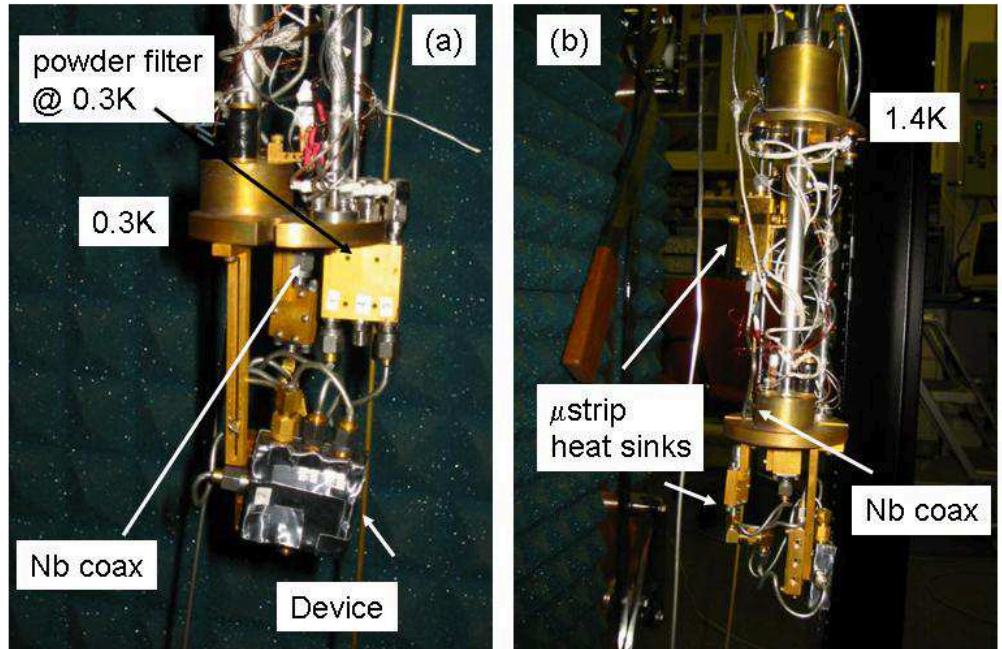
Figure 4.12: ^{3}He fridge: (a) sample stage; (b) 1.4 K stage.

alternating sections of Au and Nb deposited on quartz for the microstrip line at 1.4K, both enclosed in RF-tight Au-plated Cu boxes [23].

The resistance of the lines was measured at room temperature from the T_{room} connectors to the sample stage and is reported in the following.

R_{line1} (SQUID bias line)$=61\Omega$

R_{line2} (device output line)$=16\Omega$

R_{line3} (SQUID modulation line)$=67\Omega$
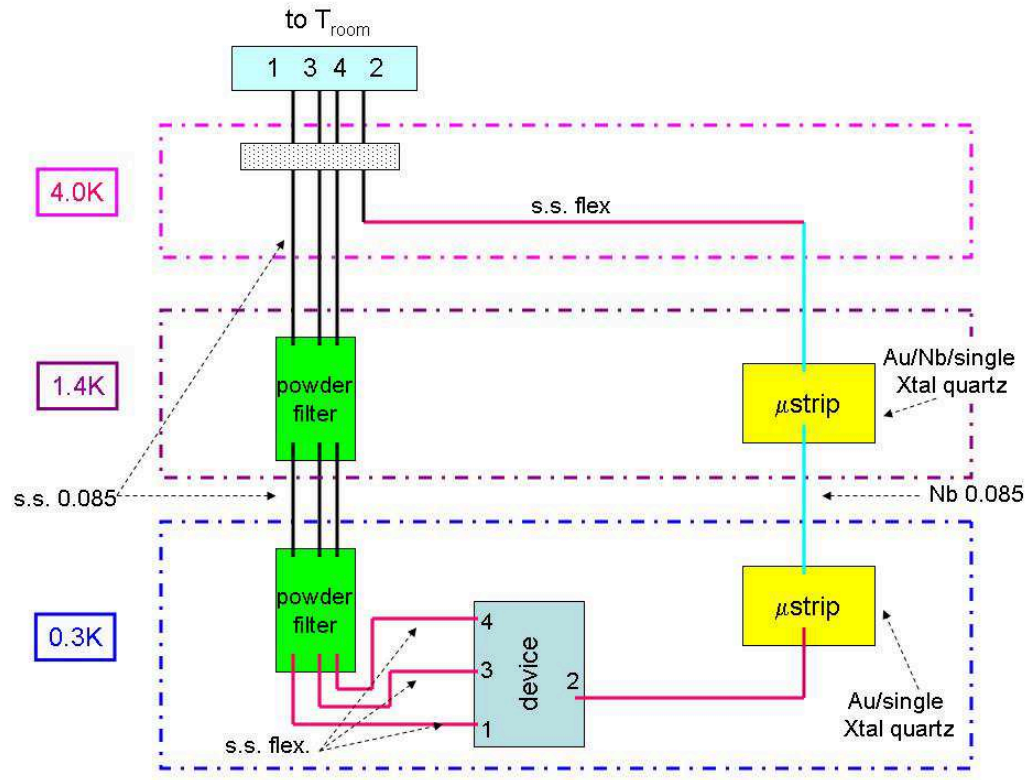
Figure 4.13: ^{3}He fridge wiring.

R_{line4} (SQUID input circuit line)=65Ω

Transmission measurements through the fridge lines from the IVC pumping port level to the device stage were performed (with the fridge at room temperature) to determine and check the continuity and attenuation of the lines. Fig. 4.14 illustrates one typical result. Attenuation of the device output line (line 2) was about -1.5 dB at 10 MHz (around the operating frequency of the device), while the attenuation of the SQUID bias, modulation and input coil lines (lines 1, 3 and 4 respectively) was about -5.5 dB at the same frequency.

Moreover reflection *versus* frequency through SQUID bias, modulation coil and
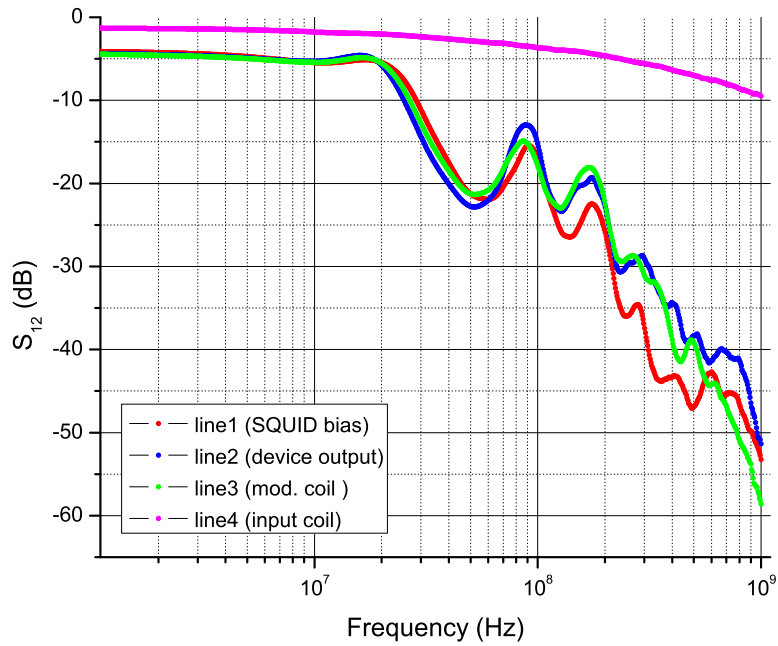
Figure 4.14: Transmission through the fridge lines at $T = T_{room}$. Around 10MHz (operational frequency of the device) the attenuation was about -1.5dB for line 2 (device output), and about -5.5dB for the remaining lines (line 1, 3 and 4).

input lines was measured with the fridge at room temperature and the lines open at one end. Reflection coefficient traces (in dB) are shown in Fig. 4.15 illustrating an absorption dip of about -15dB in the range of frequencies of interest related to internal reflection in the powder filters. This is illustrated by a PSpice simulation (Fig. 4.16) where each powder filter has been modeled through a T-shaped (almost) symmetric RLC filter, where the values of inductance, capacitance and resistance of each filter section have been determined in the first step of the simulation from similar powder filters recently fabricated in Keith Schwab's Laboratory at Cornell

University, and then optimized in the following PSpice runs.
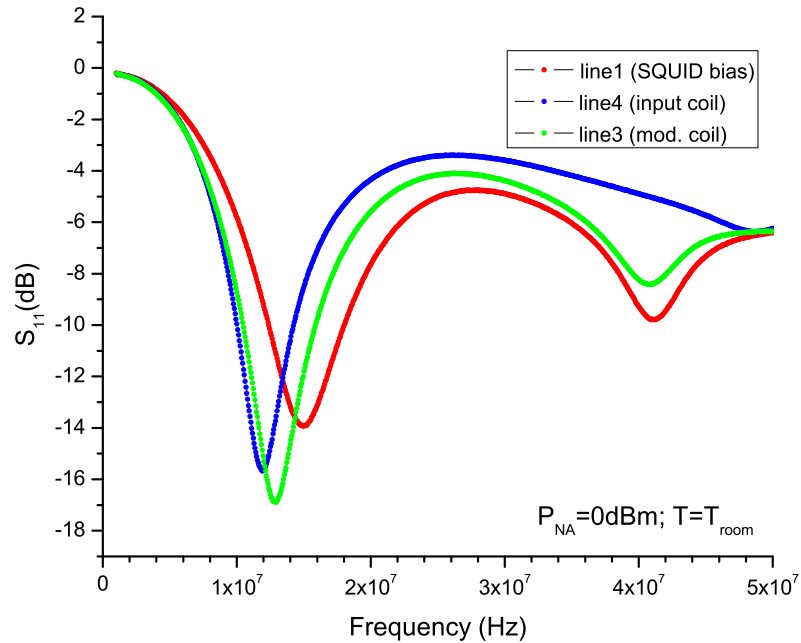
Figure 4.15: Measured refection through bias, input and modulation lines of the fridge at $T = T_{room}$.

A $100M\Omega$ resistor closes the circuit line in the simulation schematic to *mimic* an open circuit. While a detailed lumped element modeling of powder filters is beyond the purpose of this thesis, the simulation presented in Fig. 4.16 provides in first approximation a reasonable estimate of the resonances observed in the device during reflection measurements that will be presented later (Section 5.2.1).
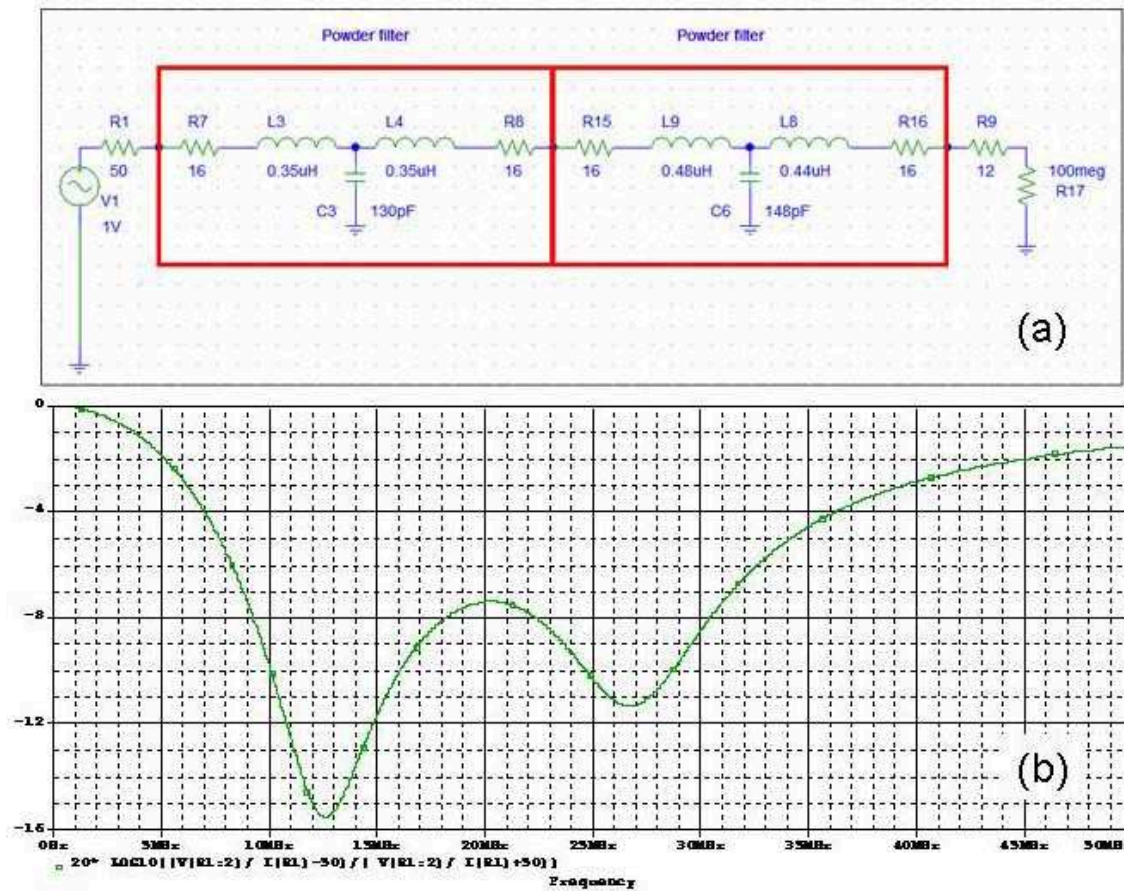
Figure 4.16: a): Schematic of the fridge input line expressed by a set of lumped elements. Resistances are expressed in Ohms. (b): PSpice simulation of the reflection through input line of the fridge at $T = T_{room}$ as a function of frequency. The vertical axis represents the reflection coefficient expressed in dB.

4.2.2 The apparatus: Room temperature wiring and measurement set-up

DC bias signals for the SQUID and the modulation coil were sent from a PC-controlled program [10] through a breakout box [11] and an opto-isolator [12] bench whose input and output were fed by a homemade DC power supply and by $\pm 18V$ batteries respectively. DC voltage signals were then converted into current bias by passing through 100KΩ (SQUID bias) and 10KΩ (modulation coil bias) resistors inserted in room temperature filter boxes. Fig. 4.17 shows a PSpice simulation of the SQUID bias circuitry attenuation (in dB) including the room temperature filter box, fridge lines, powder filters (as simulated in the previous section), the device bias circuit and the SQUID, represented in its resistive state by the parallel of its two shunt resistors.

Analogously, Fig. 4.18 shows a Pspice simulation of the modulation coil circuitry including its room temperature filter box, where the modulation coil inductance has been expressed by a 100pH inductor- as approximately estimated by scaling the value of the input coil inductance, and supposing L $\approx$n^2, with n the number of turns in a planar coil.

---

[10]LabView

[11]National Instruments BNC-2140

[12]ISO 100CP by Burr Brown Co., Tuscon, AZ 85734, Tel. (520) 746-1111.
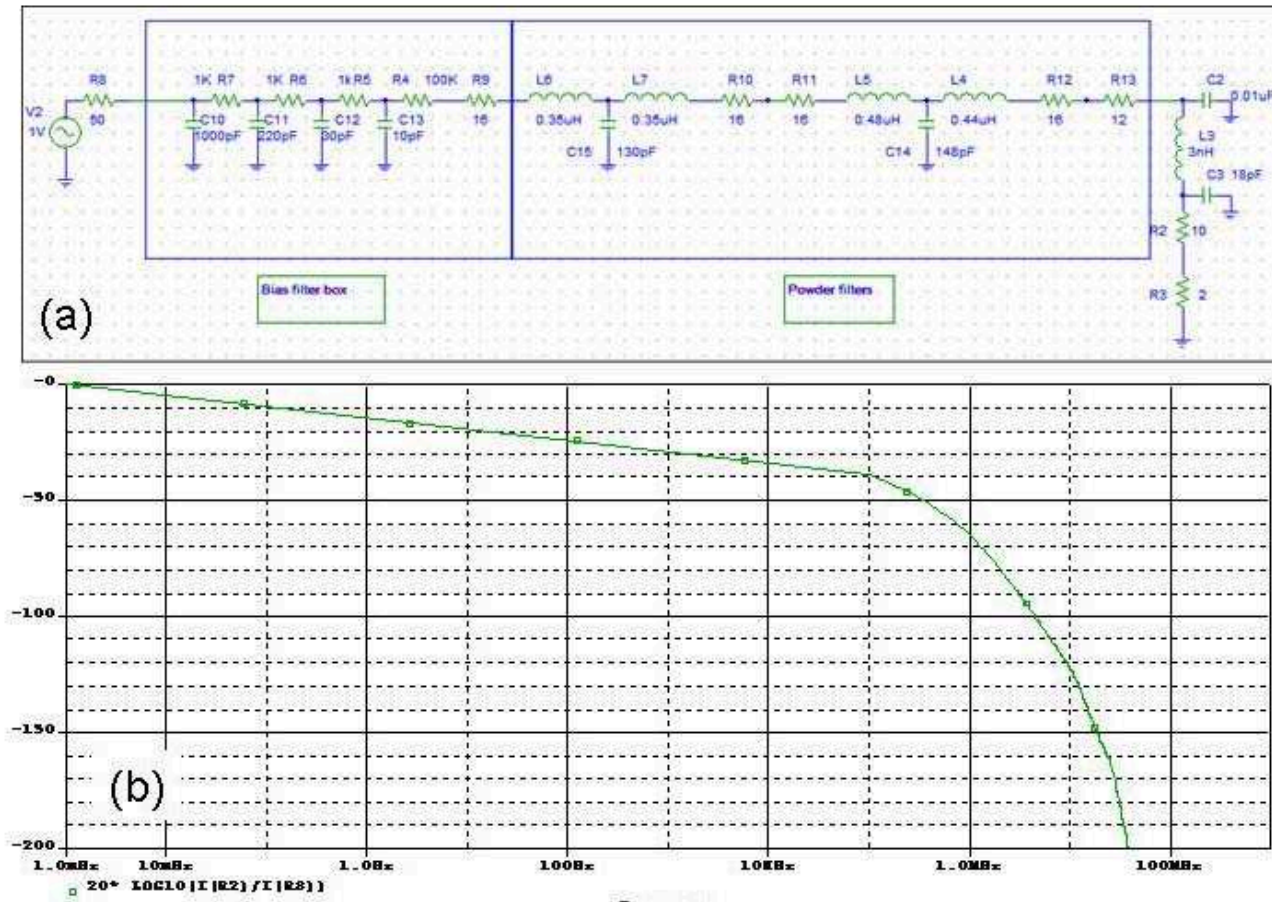
Figure 4.17: PSpice schematic (a) and simulation (b) of the SQUID bias circuitry attenuation including room temperature filter box, fridge lines, powder filters and device bias circuit. Resistances are expressed in Ohms. The SQUID is represented by the parallel of its two shunt resistors.
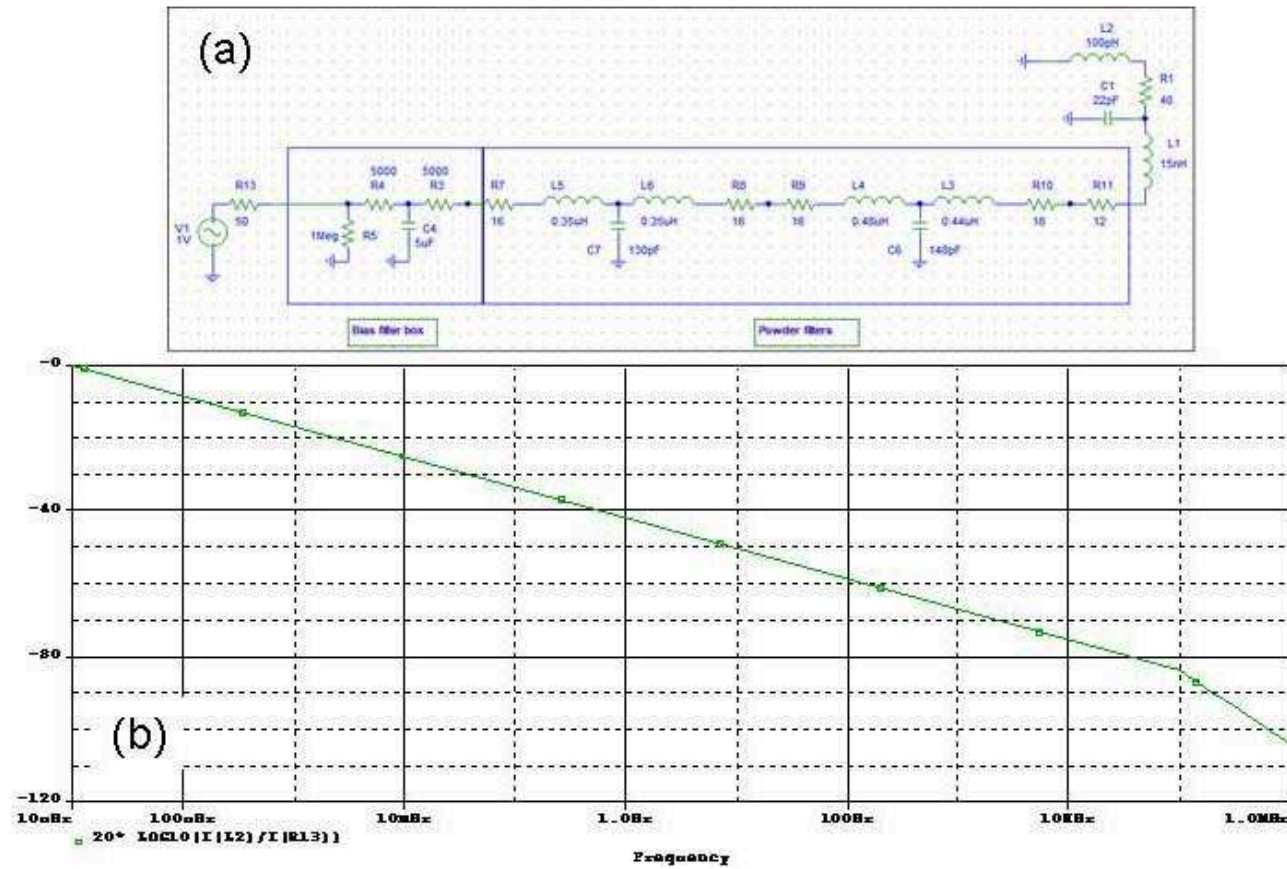
Figure 4.18: PSpice schematic of the modulation bias circuitry (a) and simulation (b) of circuit attenuation including room temperature filter box, fridge lines, powder filters and device bias circuit.

An alternating signal at frequencies around 10MHz could also be fed into the modulation coil circuit from a function generator [13] by means of a commercial room temperature bias-tee [14] followed by a series of attenuators whose value will be specified in the following for different measurements. The output of the device was split by a room temperature bias-tee [15] into DC and RF outputs. The DC output was directed into a low-noise preamplifier [16] with the signal amplified by a factor of 10^3, while the RF output signal was fed into an RF room temperature amplifier [17]. The RF amplifier gain as a function of the frequency is illustrated in Fig. 4.19, presenting a gain G $\cong$ 37dB up to about 10MHz. Also, the amplifier voltage noise was determined from the measurement of the output power spectrum with the amplifier input shorted ($\sqrt{S_v}$=0.3nV/$\sqrt{Hz}$).

---

[13] Agilent 3320A

[14] Mini-Circuits ZFBT-4R2GW

[15] Mini-Circuits ZFBT-4R2GW

[16] Stanford Research System SR560

[17] MITEQ amplifier, M/N AU-1464, Freq. 1-200MHz, S/N 848590
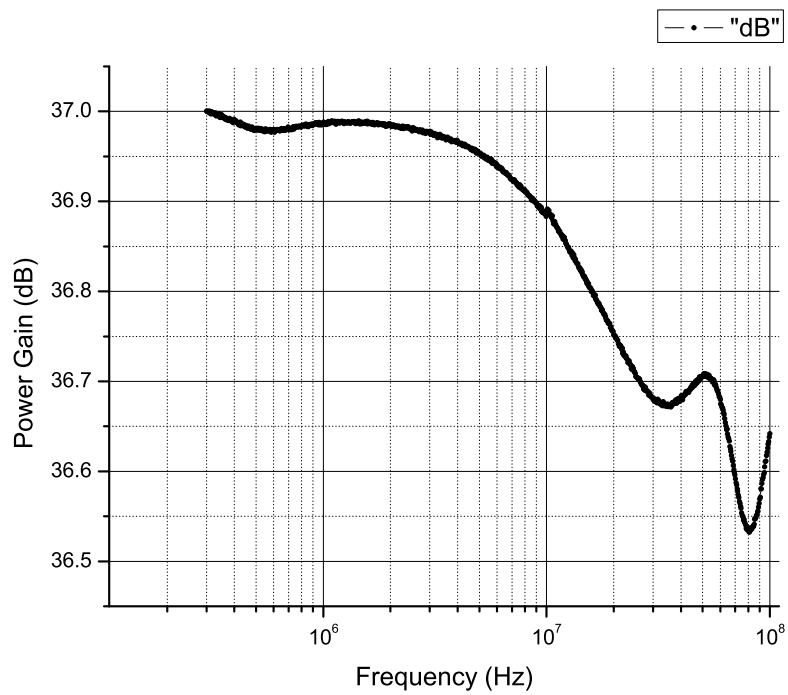
Figure 4.19: Gain of the room temperature Miteq amplifier. The power of the network analyzer was set to -40 dBm.

Chapter 5

Experimental results: device characterization and sensitivity

Though different devices were built and tested in the course of this work, the main results have been achieved working with the device named (4.1), and will be presented in the following. A previous device (4.0) will be introduced as an intermediate step toward the last tested and measured version. Flux noise measurements for an uncoupled ($\approx 3\mu H$ input inductance) SQUID were performed on device (1.0) and are presented in Appendix B.

5.1   From device 4.0 to device 4.1: adjusting the design

Device 4.0 was built following the layout for device 3.0 (Fig. 4.7 and Fig. 4.8). According to the scheme presented in Section 3.3, a 15-turn input coil SQUID [1] was wired to the device circuitry. In order to test if the resonances of the input circuit were falling in the frequency range required by the design, a measurement of reflection through the input circuit was performed.

First the SQUID was DC biased in the resistive state ($I_{bias}^{SQUID} >> I_c \approx 4\mu A$) along the IV curve taken at 4K and for zero DC voltage applied at the modulation coil circuit (Fig. 5.1).

---

[1] Input inductance $L_i \approx 20$ nH, SQUID inductance $L \approx 80pH$, and coupling constant $k \approx 0.8$, as determined from Section 4.1.1 formulas. See Table 4.1.
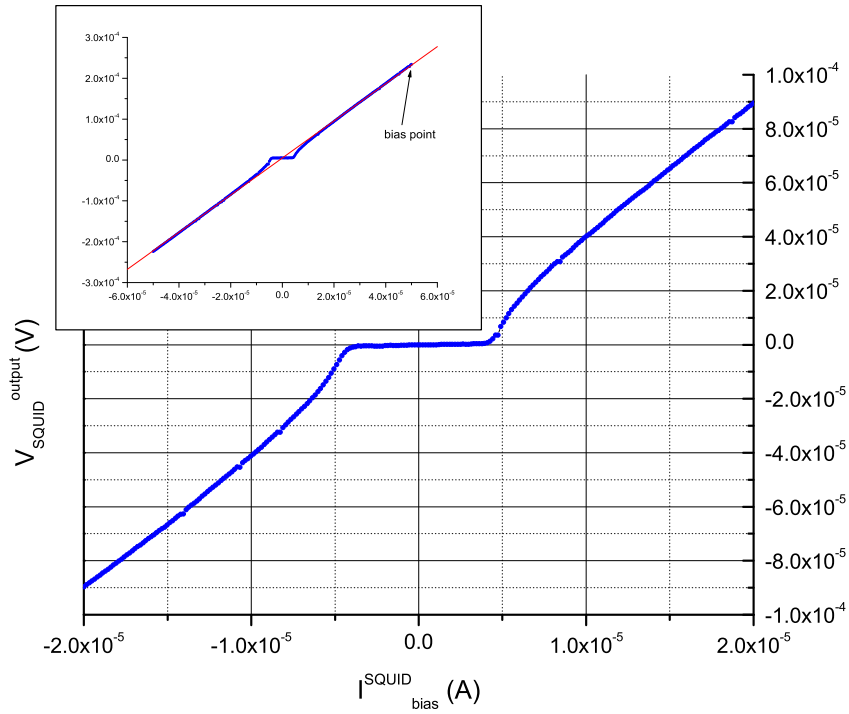
Figure 5.1: Device 4.0, IV characteristics at T=4K. Inset: the red line is the linear fit of the high bias current curve.

The SQUID dynamic resistance is defined as $R_{dyn} = \partial V/\partial I_{bias}$, with V the voltage at the output of the SQUID and I_{bias} the SQUID bias current. With the SQUID in the high-bias current, resistive state, R_{dyn} is the parallel of the two shunt resistors. R_{dyn} could thus be extracted from the slope of the high-current curve (see inset in Fig. 5.1) resulting in $R_{dyn} \approx 4.5\Omega$. Then a -20 dBm signal from a Network Analyzer [2] was sent into the input circuit and the reflected-to-incident power ratio in dB (S_{11}) was measured.

Two hypothesis were formulated when considering the data taken at 4K (Fig. 5.2),

---

[2]Agilent N3383A (300KHz - 9GHz) PNA Series Network Analyzer.
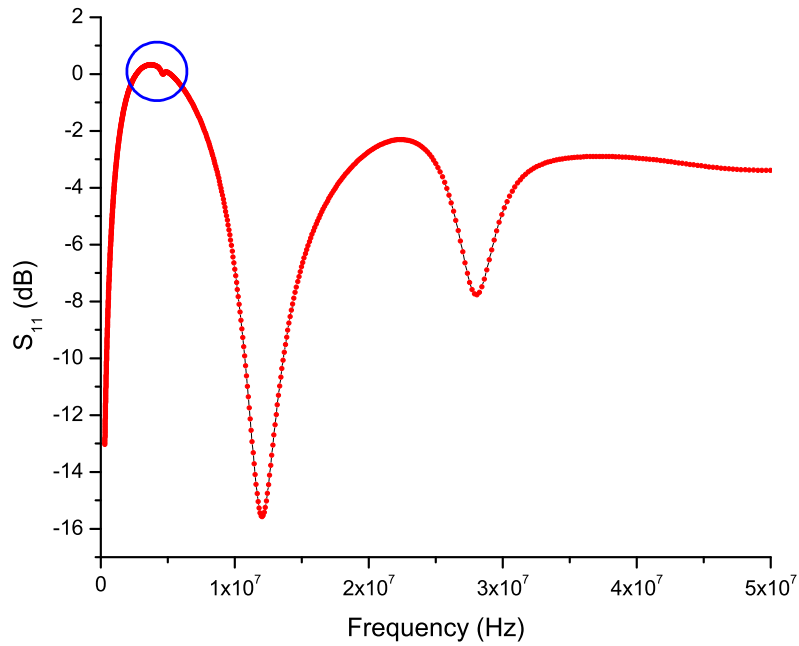
Figure 5.2: Device 4.0, reflection through the input, T=4 K. The blue circle highlights the 4.6MHz resonance of the SQUID-side section of the input circuit.

and tested with device (4.1) that will be introduced in the following section:

- the main absorption dips in the data could be explained by internal reflections in the powder filters along the input line, as introduced in Section 4.1.3;

-the small resonance around 4.6MHz could be attributed to the resonance of the SQUID-side section of the input circuit [3].

[3]Of the two sections of the device input circuit the resonance related to the $10\mu H$-$18pF$ section of the input circuit could not be observed in this configuration, since it was shorted by the impedance of the 30nF around 10 MHz. The values of the components of the section had been previously tested at T_{room} and 4K in a configuration connected to ground by a stray capacitance (Fig. 4.4).

5.2   Device 4.1

5.2.1   Device 4.1: characterization

From the 4.6MHz resonant frequency shown in Fig. 5.2 and the 30nF capacitance in the SQUID-side section of the input circuit an *effective* total inductance $(L_i + L_{stray}) \approx 40nH$ was derived. Device 4.1 was then built with the value of the capacitor changed to 4.7nF in order to move the resonance accordingly in the frequency range of interest (Fig. 5.3).
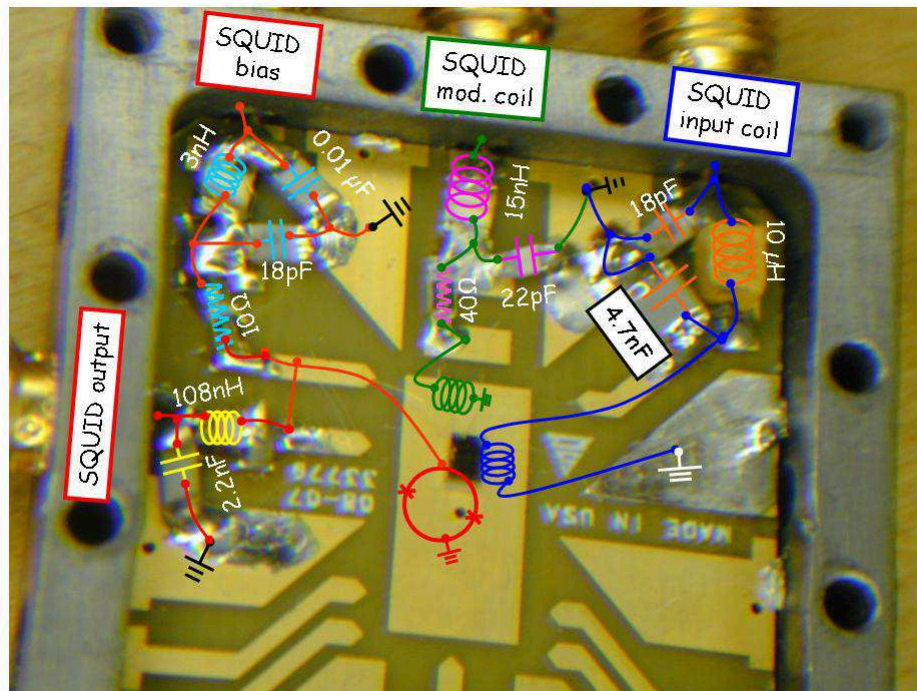
Figure 5.3: Device 4.1 box: detail on SQUID bias, SQUID output, SQUID input and SQUID modulation coil circuits. The SQUID is color-coded: SQUID loop, bias and output (red), modulation coil (green) and input coil (blue).

Figure 5.4 presents the data from reflection measurements through the fridge

input line and the device input circuit at 4K with the SQUID biased in the resistive state, together with the T_{room} reflection data taken on the fridge input line open on one end (no device) showing the $\approx 16dB$ measured dip (related to internal reflections in the powder filters as introduced in Section 4.1.3), as well as the dip of the device input circuit (SQUID side section) shifted from 4.6MHz to about 11.6MHz.
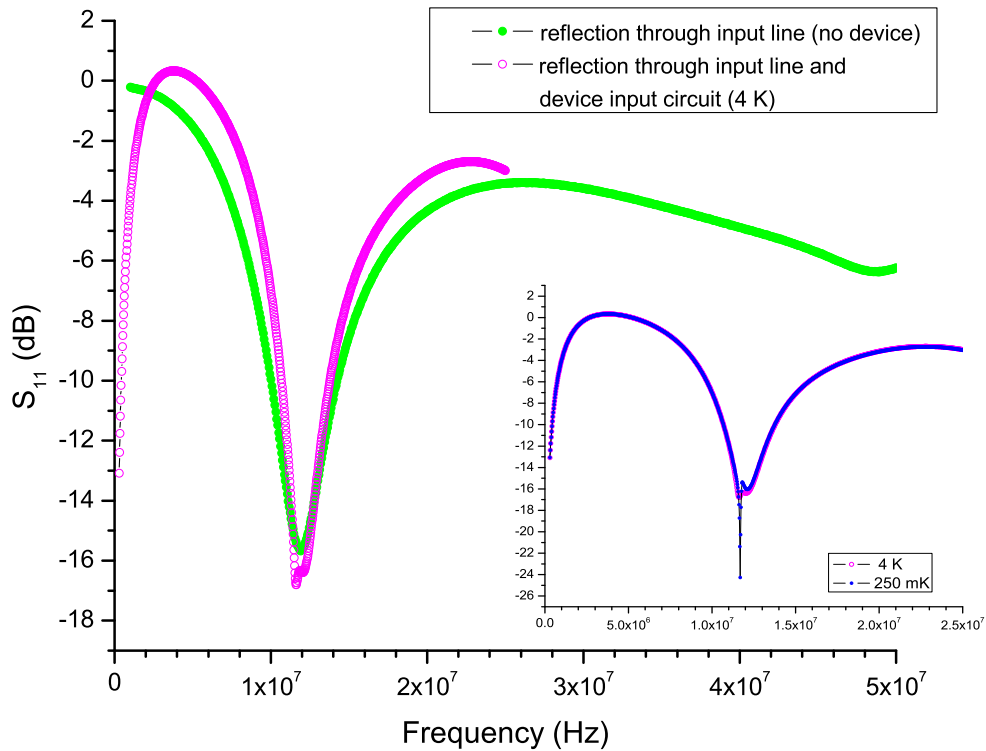
Figure 5.4: Device 4.1: Reflection through the input at T=4 K with the SQUID biased in a resistive state and reflection $(T = T_{room})$ through the fridge input line (line 4). Inset: Reflection through the input at T=4K and T=250mK.

PSpice simulation of the device is presented in Fig. 5.5. The input line and powder filters have been modeled following the schematics presented in Chapter 4

(Fig. 4.16), while the device has been represented by its lumped elements circuitry, with the SQUID as a linear transformer (labeled *TX1* in Fig. 5.5), whose primary inductance has been set to 40nH and the secondary (SQUID) inductance to 100pH (see also Table 4.1). Values for resistors are in Ohms.
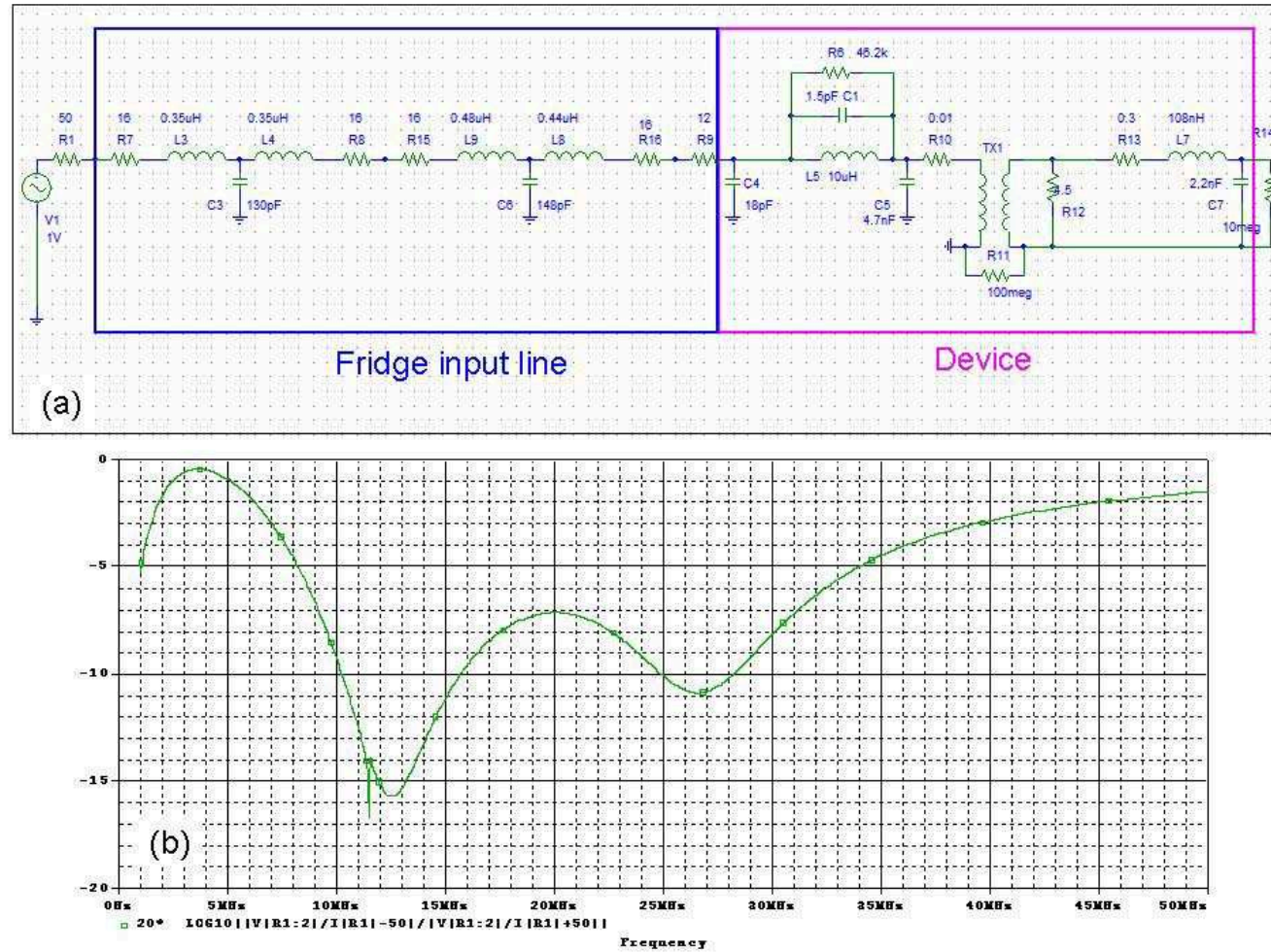
Figure 5.5: (a) PSpice schematics of device 4.1 and fridge input line. The circuit is described in the text. (b) Reflection coefficient simulation.

The $10\mu H$ and the $108nH$ inductors at the input and output circuits have been represented by equivalent circuits for real inductors [4]. A $10M\Omega$ resistor closes the device output to represent reflection from an open termination [5]. The 0.01Ω in one of the two input sections (SQUID-side) represents the resistance of the Aluminum bonding wires still normal at 4K. Fig. 5.4 (inset) shows reflection through the input data taken at 250mK where the quality factor of the resonance increased as a result of the Aluminum bonding wires becoming superconducting. At 250mK the input circuit resonated at 11.68MHz, with a quality factor $Q \approx 170$, and a resonance width $\Delta\nu \approx 70KHz$.

Also, a measurement of straight reflection through the device output circuit was performed by biasing the SQUID in the resistive state, and measuring the reflection coefficient S_{11} (dB) from the output of the device, with -20dBm of input power from the network analyzer.

Figure 5.6 shows an absorption dip at about 13.3MHz (T=4K), with a quality factor Q of about 3 in agreement with the design. Moreover, reflection through the output circuit was verified by sending the reflected wave into the MITEQ (50Ω

---

[4]To model the $10\mu H$ inductor from Vishay-Dale (see Table 4.2) the results from circuit simulation provided by the manufacturer were used (www.vishay.com), while the impedance of the $108nH$ inductor was separately modeled with Matlab using the manufacturer's parameters (http://www.coilcraft.com/models.cfm), and then expressed (for frequencies around 10MHz) as a series of an ideal inductor ($108nH$) and a resistor (0.3Ω).

[5]To comply with PSpice requirement that each node in the circuit must have a DC path to ground, a resistor R_{11} was introduced in the schematics (Fig. 5.4) and its value ($100M\Omega$) chosen such that its effects on circuit performance were negligible [65].
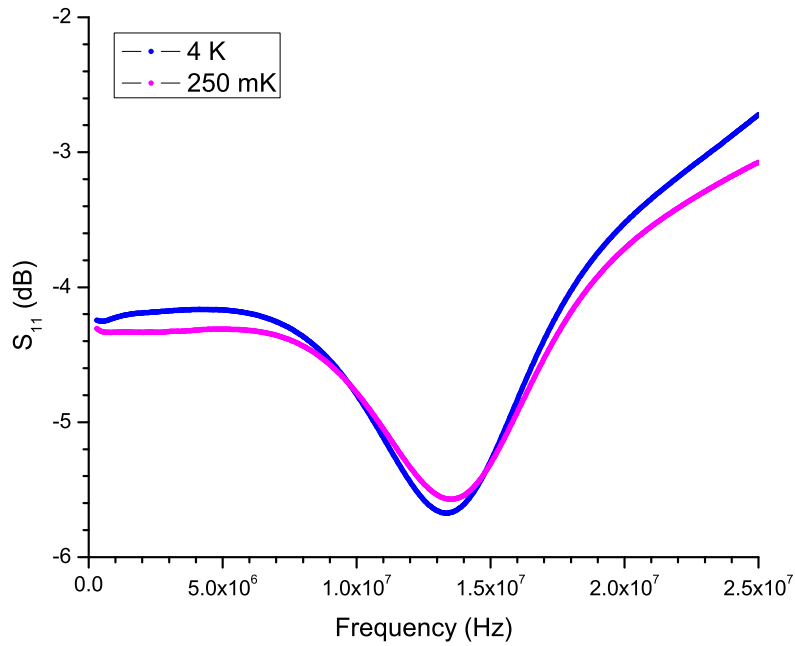
Figure 5.6: Reflection through the output, with the SQUID biased in the resistive state. T=4K and T= 250mK.

impedance) amplifier through a commercial directional coupler [6], and verifying the frequency of the absorption dip.

5.2.2 Device 4.1: reference signal calibration

A signal calibration was needed for the modulation coil circuit signal in order to determine the ratio between the voltage applied at the modulation coil and the flux produced in the SQUID (*modulation coil voltage-to-flux transfer coefficient* in the following). When sending a DC signal into the modulation coil, the calibration is accomplished through the modulation current (I_{mod})-voltage characteristics, shown

---

[6]Mini-Circuits ZFDC-20-3

in Fig. 5.7 as $(V - \Phi)$ after calibration, and obtained at T=250mK with the SQUID current-biased slightly above its critical current.
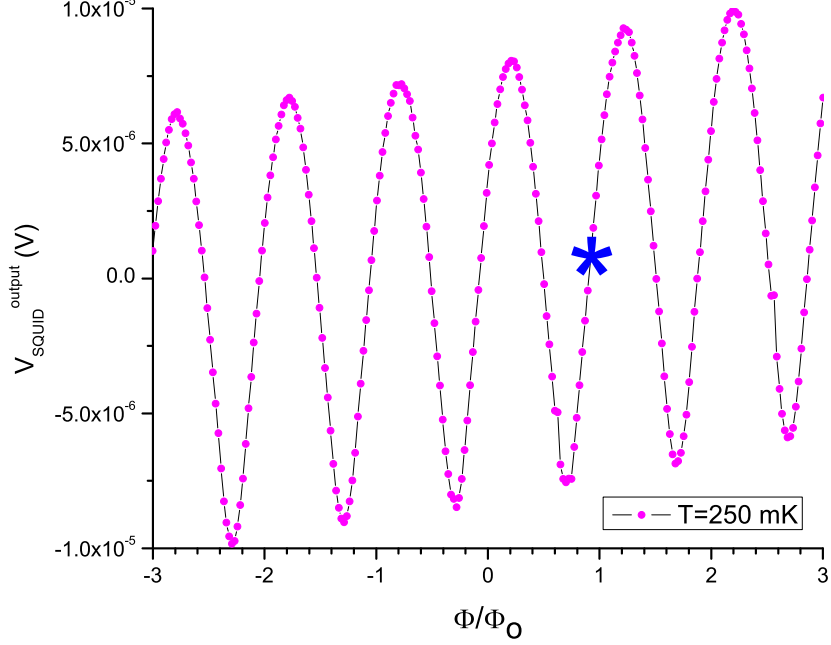
Figure 5.7: SQUID output voltage as a function of the flux generated by a DC signal into the modulation coil at T=250 mK. The blue star indicates a typical bias point at $\Phi = (1 \pm 2n)\Phi_o/4$ (maximum sensitivity point).

The data illustrate the SQUID output voltage V_{SQUID}^{output} periodic in Φ with period Φ_o[7], with a modulation coil transfer function (referred to the DC voltage applied from the source) $\mathcal{V}_{\phi}^{mod}{}_{DC} = 0.33V/\Phi_o$ and a current transfer coefficient referred to the current flowing in the modulation coil $(\mathcal{I}_{\phi}^{mod})_{DC} = 33\mu A/\Phi_o$. From data in Fig. 5.7 it was also possible to estimate M_{mod}^{DC} (mutual inductance between

---

[7]Data show a drift most probably due to the low-noise amplifier.

the SQUID and the modulation coil, $\approx 0.8nH$).

Moreover, the linear fit of the maximum slope portion of the $V - \Phi$ curves allowed to determine the device *flux-to-voltage* transfer coefficient $(V_\phi^{device})_{DC} = (45 \pm 2)/\Phi_o$, while an estimate for $(V_\phi^{SQUID})^{max} \approx (R/L)$ provided $\approx 214\mu V/\Phi_o$ as derived from $R \approx 9\Omega$ and $L \approx 84pH$.

Because of external losses in the circuitry leads, it is reasonable to expect that the coupling between the modulation coil and the SQUID should be modified when an RF signal is fed into the modulation circuit. An alternating signal through the modulation coil could be calibrated by means of the Bessel function calibration currently used in RF-SET detection schemes [17] [23] [24]. In this measurement (see Fig. 5.8 for a schematic) the SQUID was biased at a maximum sensitivity point of the DC $V - \Phi$ curve (the blue star in Fig. 5.7).

Then, a sinusoidal signal of frequency ν_o and variable amplitude was fed into the modulation coil circuit from a function generator [8] through a series of room temperature attenuators (-50dB unless otherwise specified), and the (real component of the) SQUID output signal [9] after the MITEQ amplifier was monitored by an RF lock-in [10].

The device output amplitude as a function of the variable amplitude applied at the modulation circuit followed a Bessel function of the first kind behavior [17], and the zeros of its fundamental harmonic provided the amplitude of the voltage generating

---

[8]Agilent 3320A

[9]The phase of the RF lock-in was set such as to minimize the portion of signal amplitude in the imaginary component channel.

[10]Stanford Research Systems SR844 RF lock-in amplifier.
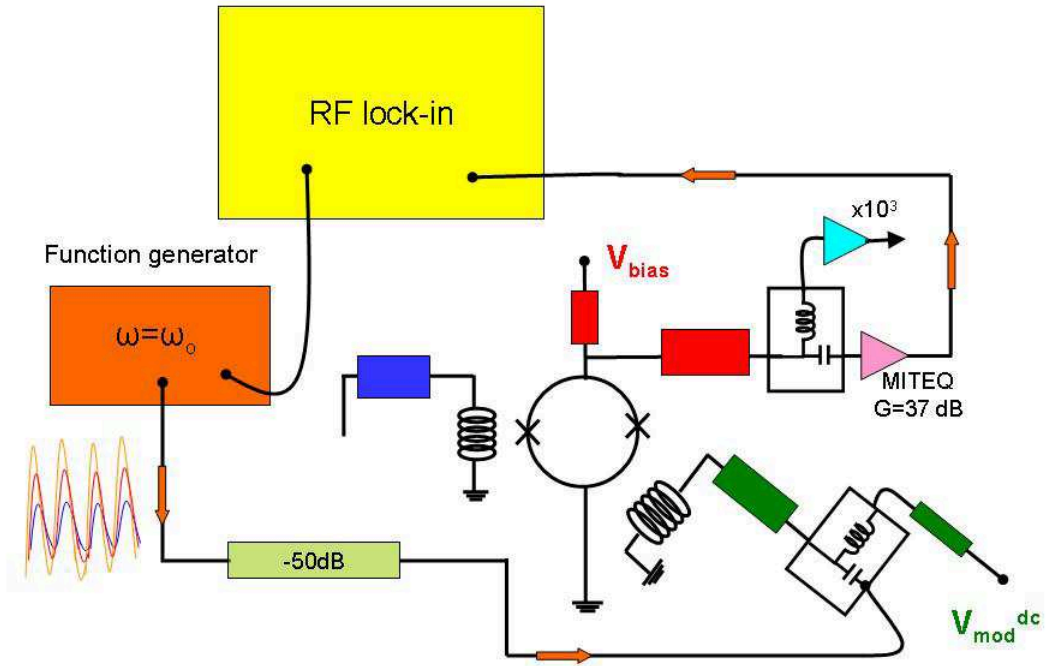
Figure 5.8: Bessel calibration measurement set-up. The device circuitry is represented by a a color scheme: input (blue), SQUID bias and output (red), modulation coil circuitry (green).

$1\Phi_o$ in the SQUID.

Figure 5.9 illustrates such measurement for a device with the input circuit disconnected from any source, frequency ν_o=10MHz and temperature T=250mK, expressed in terms of amplitude of the device output voltage (V_{device}^{output}) *versus* the rms voltage applied at the modulation coil (V_{mod}^{rms}). The device output was determined after dividing the signal from the RF lock-in by the amplification of the MITEQ (a factor of 70 in voltage). The rms voltage applied at the modulation coil was derived
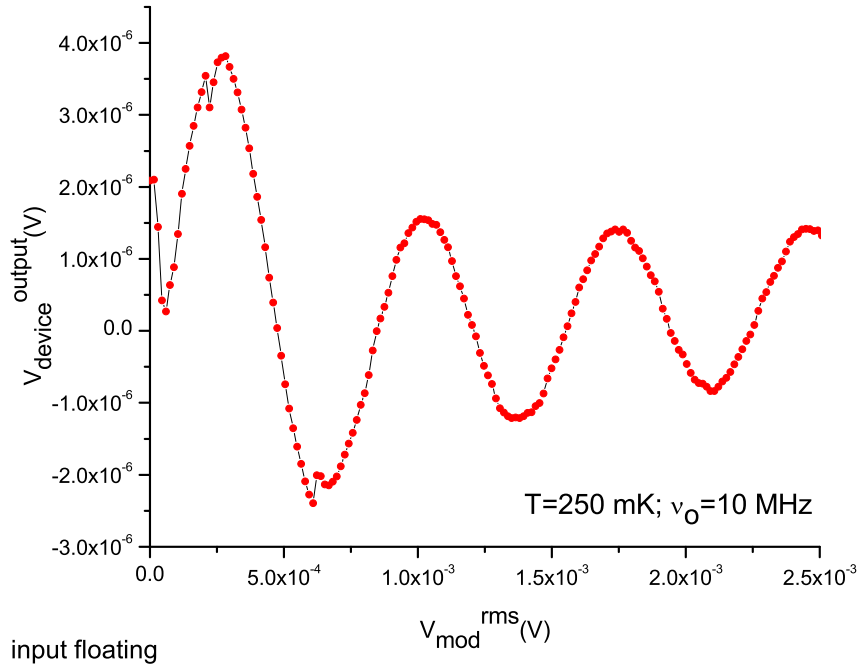
Figure 5.9: Bessel calibration measurement data, T=250mK, and $\nu_o = 10MHz$.

from the amplitude of the source signal after 55.5dB of attenuation, accounting also for the cable attenuation. For a modulation coil signal frequency of 10MHz $(\mathcal{V}_\phi^{mod})_{10MHz} \approx 3.2 \mathrm{x} 10^{-4} V_{rms}/\Phi_o$ resulted.

5.2.3 Device 4.1: transmission through the modulation coil circuit

Measurements of transmission from the modulation coil circuit to the output of the device were performed for different temperatures and SQUID bias conditions. In the measurement set-up (Fig. 5.10) the SQUID was DC-biased (at its maximum

sensitivity point [11], shorted [12], or in the resistive state [13]), and a signal from the Network Analyzer [14] was fed into the modulation coil circuit through a set of room temperature attenuators and a commercial bias-tee [15].
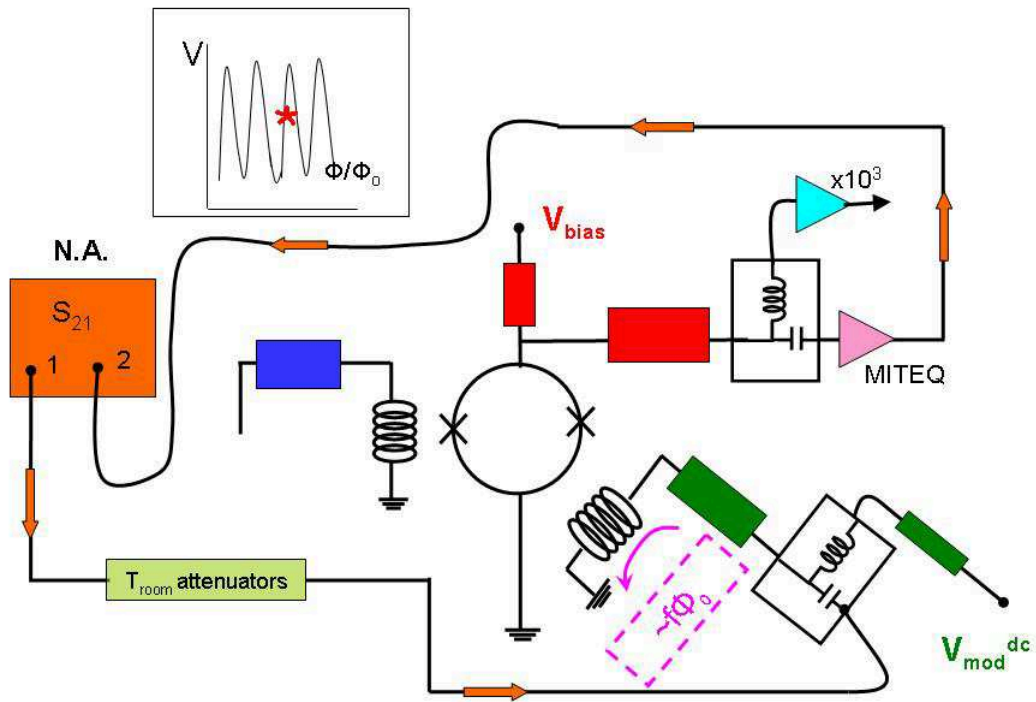
Figure 5.10: Transmission through the modulation coil measurement's scheme.

The transmission S_{12}(dB) as ratio of the device output power (before am-

---

[11] As shown in Fig. 5.7.

[12] For zero applied DC SQUID bias and DC modulation voltage.

[13] For zero DC voltage applied at the modulation coil circuit, and 5V applied to the SQUID bias circuit from the DC source.

[14] Agilent N3383A (300KHz - 9GHz) PNA series Network Analyzer or Agilent 4395A (10Hz - 500MHz/10Hz - 500MHz/100KHz - 500MHz) Network/Spectrum/Impedance Analyzer.

[15] Mini-Circuits ZFBT-4R2GW

plification through the MITEQ) and the Network Analyzer input power was then recorded and it is illustrated in Fig. 5.11 for T=4K, 1.5K and 250mK and different SQUID bias. The power fed into the modulation coil circuit from the Network Analyzer and after -84.5 dB of total attenuation was about 4pW.

The data showed a resonance at about 11.6MHz [16] sensitive to both the temperature and the SQUID bias. Moreover, at T=250mK, a series of resonances appeared in the main peak (see Fig. 5.11 (d)) suggesting a possible overdriving from the modulation coil, and consequent excitation of more than $1\Phi_o$ in the SQUID.

Changes in the 11.6MHz resonance were recorded at T=250mK and the SQUID biased at its sensitivity point by varying the power levels from the N.A. into the modulation coil circuit. Fig. 5.12 shows a set of data for different powers at the modulation coil (i.e. after -85.5dB of attenuation from the output of the N.A.) ranging from 9pW to 0.3pW.

Unfortunately the data in Fig. 5.12 only show a qualitative trend, since no satisfying calibration was taken in relation to the data set. Indeed, from the modulation coil voltage-to-flux transfer coefficient determined from the Bessel calibration at 10MHz $((\mathcal{V}_\phi^{mod})_{10MHz} \approx 3.2\text{x}10^{-4}V_{rms}/\Phi_o$, Section 5.3.2) it resulted that a 4pW power into the modulation coil (as in Fig. 5.11) generated about $40m\Phi_o$ in the SQUID, well below the supposed multi-Φ_o oscillations observed in the data. Hence it appeared evident that a Bessel calibration at the resonant frequency of the device response (about 11.7MHz) was necessary for a more quantitative data analysis, and it will be presented in the following sections in relation to another measurement set

---

[16]The resonance of the input circuit had been observed around 11.6MHZ in Section 5.3.1
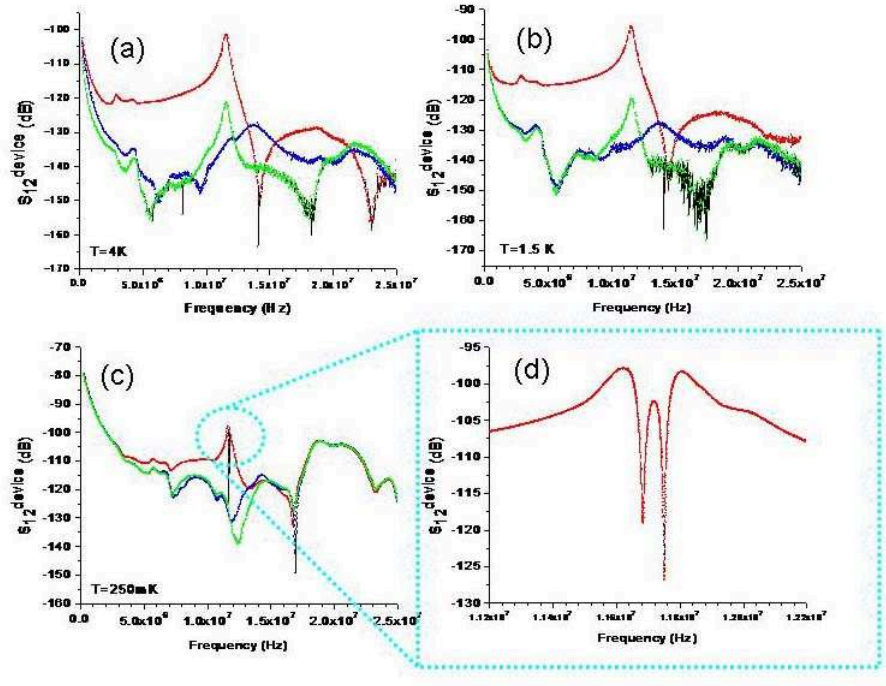
Figure 5.11: Transmission through the modulation coil circuit for different SQUID bias and temperatures. Green trace, SQUID resistive; Blue trace, SQUID shorted, red trace, SQUID biased at the sensitivity point. (a) T=4K; (b) T=1.5K; (c) T=250mK; (d) Zoom of the resonances, T=250mK, $\nu = 11.6 MHz$ and SQUID biased at the sensitivity point.

up (Section 5.3.5).

5.2.4 Device 4.1: transmission through the input coil circuit (Gain)

The gain of the device was measured according to the set-up illustrated in Fig. 5.13. With the SQUID biased at its sensitivity point at T=250mK, a frequency sweeping signal from the N.A. was sent into the input circuit through a series of room temperature attenuators, and the transmission coefficient (S_{12} (dB)) was recorded as the ratio between the device output power after MITEQ amplification and the
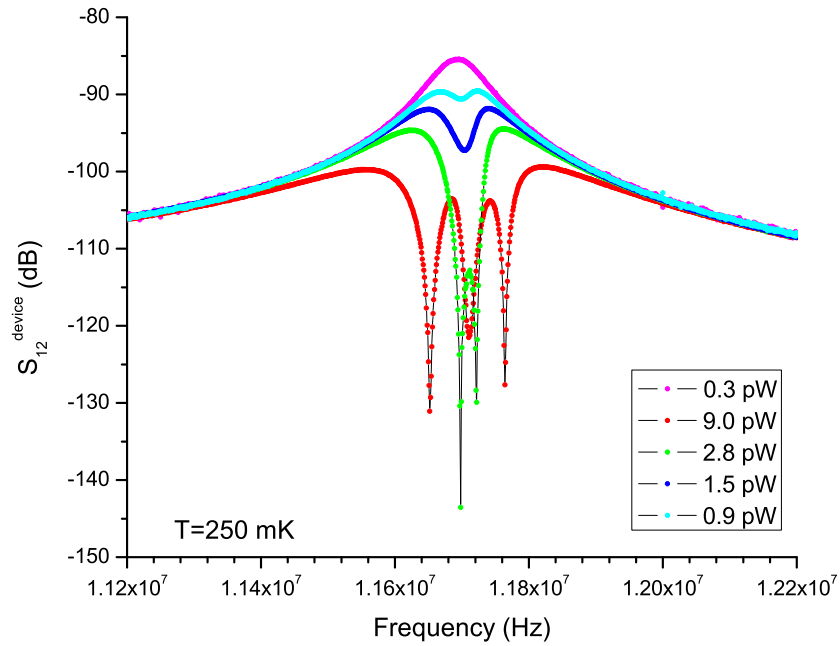
Figure 5.12: Transmission through the modulation coil circuit, T=250mK, SQUID biased at its sensitivity point and different values of power fed into the modulation coil.

Network Analyzer input power .

Results from gain measurement are shown in Fig. 5.14 for two power levels (0.3pW and 0.3fW) into the input circuit after attenuation from the fridge line (-5.5dB) and an added series of room temperature attenuators (-30dB) for the lowest power level. A series of multi-Φ_o resonances is present for the highest power level, while the low power shows the device response to the input circuit drive going smoothly through a peak at 11.7MHz.

In order to simulate the measurement set-up, the device and the fridge line were modeled in a PSpice schematic as illustrated in Section 5.2.1 (Fig. 5.15). In
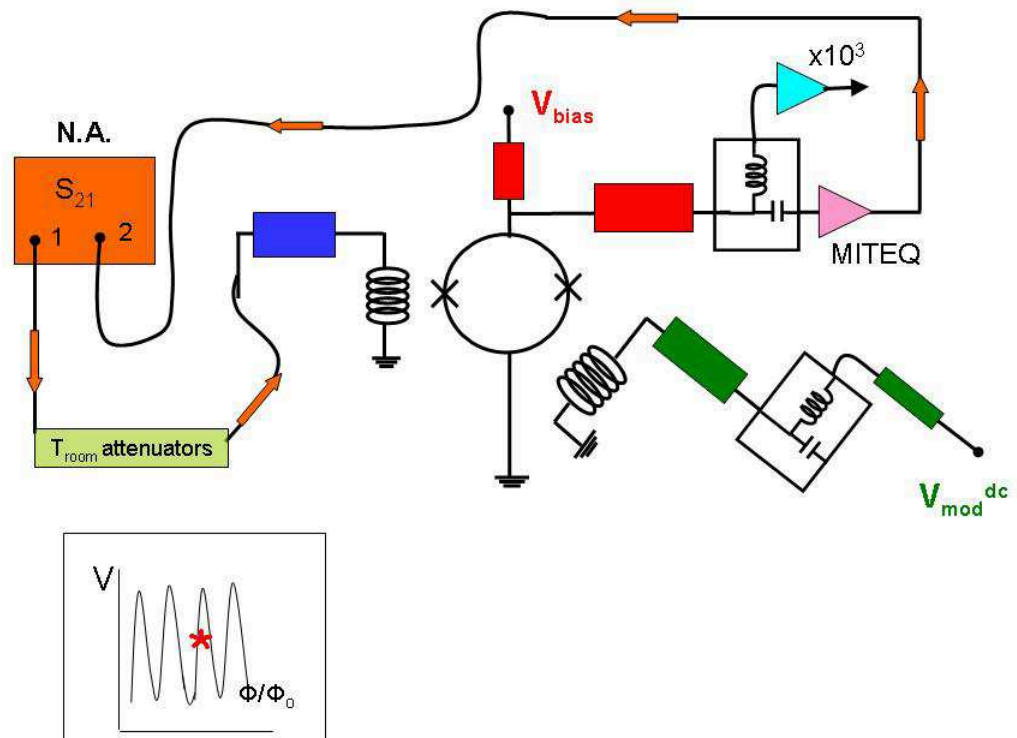
Figure 5.13: Scheme of the device gain measurement set-up (transmission through the input circuit).

the schematic the device output was closed by a 50Ω resistance to represent the impedance of the RF amplifier, and the resistance of the Aluminum bonding wires was set to $1m\Omega$.
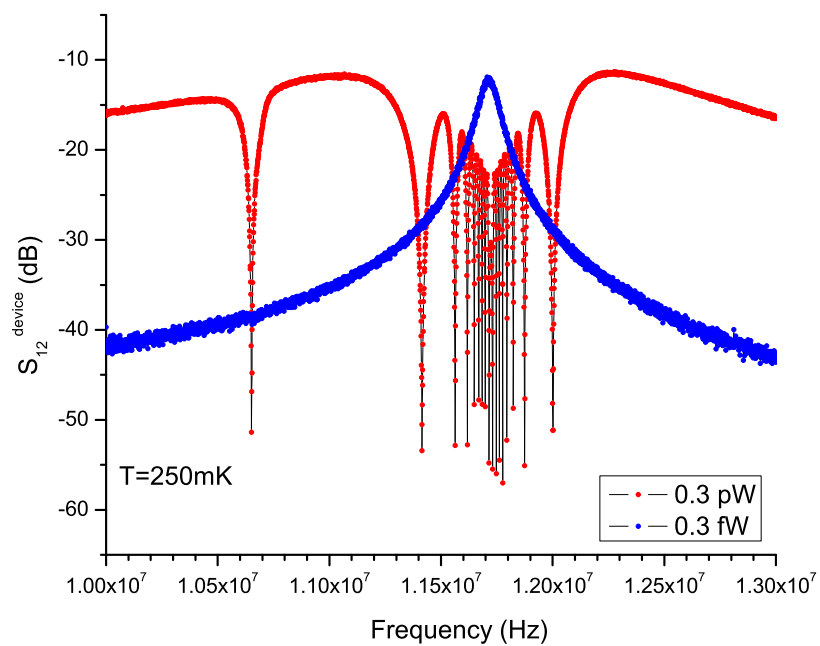
Figure 5.14: Transmission through the input, T=250mK, SQUID biased at the sensitivity point, 0.3pW (red dots) and 0.3fW (blue dots) into the input circuit.
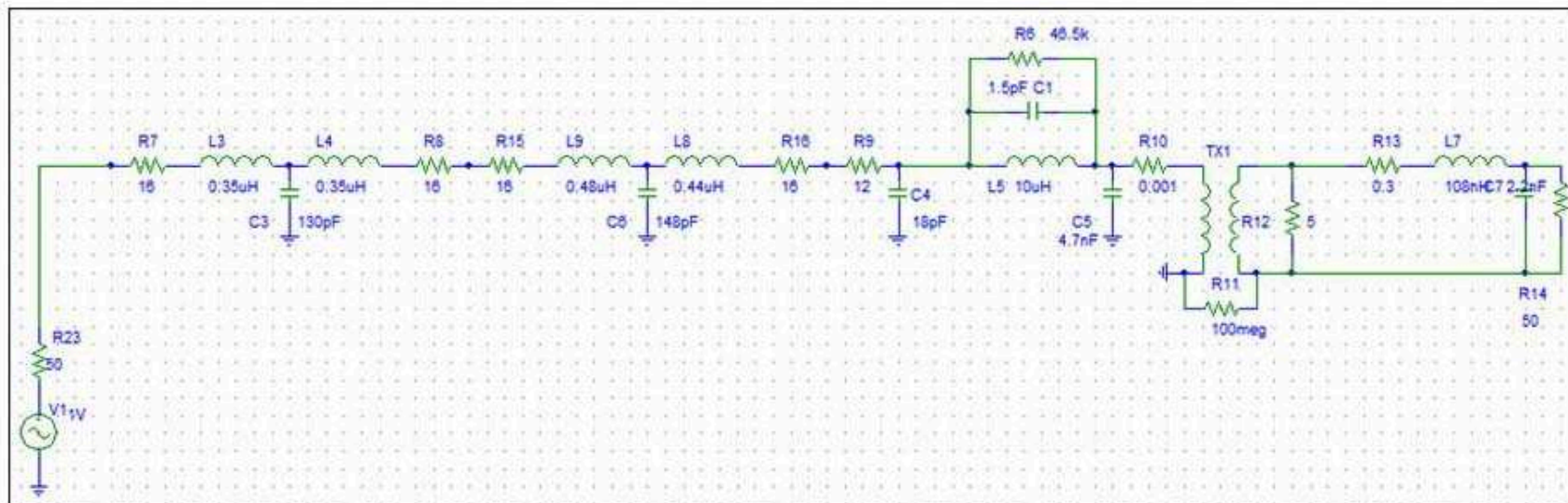
Figure 5.15: PSpice schematic of the gain measurement.

Simulation result and the experimental data for 0.3fW are also presented
(Fig. 5.16).
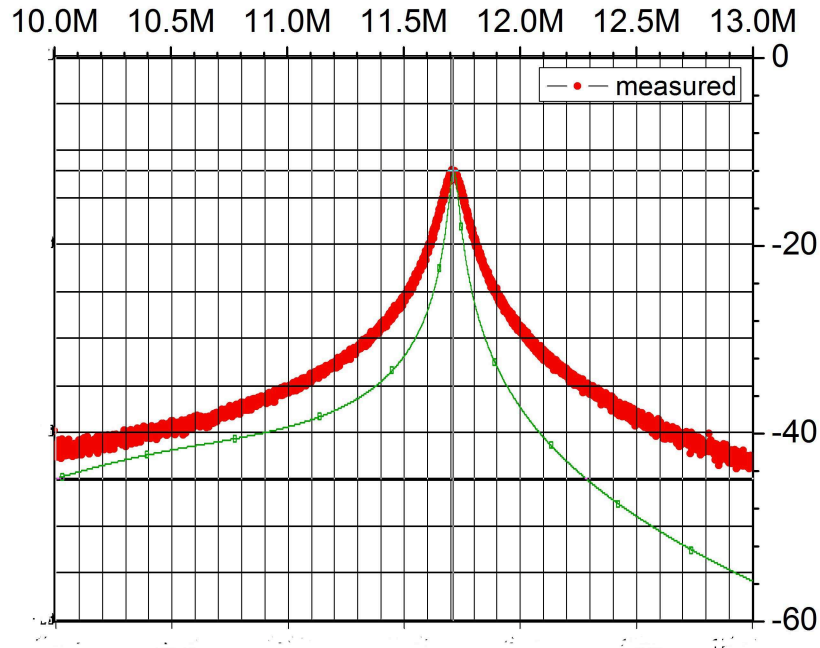
Figure 5.16: Transmission through the input. Simulation (green) and
data (0.3fW into the input circuit, red points). The vertical axis repre-
sents the transmission coefficient S_{12} expressed in dB.

Moreover, the impedance mismatch between the 50Ω Network Analyzer source
and the designed input circuit introduced a gain loss whose order of magnitude was
estimated in the following way. A PSpice simulation of a *simplified* version of the
transmission network (i.e. neglecting the modeling of the fridge lines) was performed
in the case of the input circuit closed by a 50Ω and a $50K\Omega$ source. Figure 5.17
presents the simulated $S_{12}(dB)$ as the ratio of the device output power across the
50Ω room temperature amplifier, and the input power across each source and shows
a gain loss of about $-30dB$ (at resonance) in the the mismatched source case.
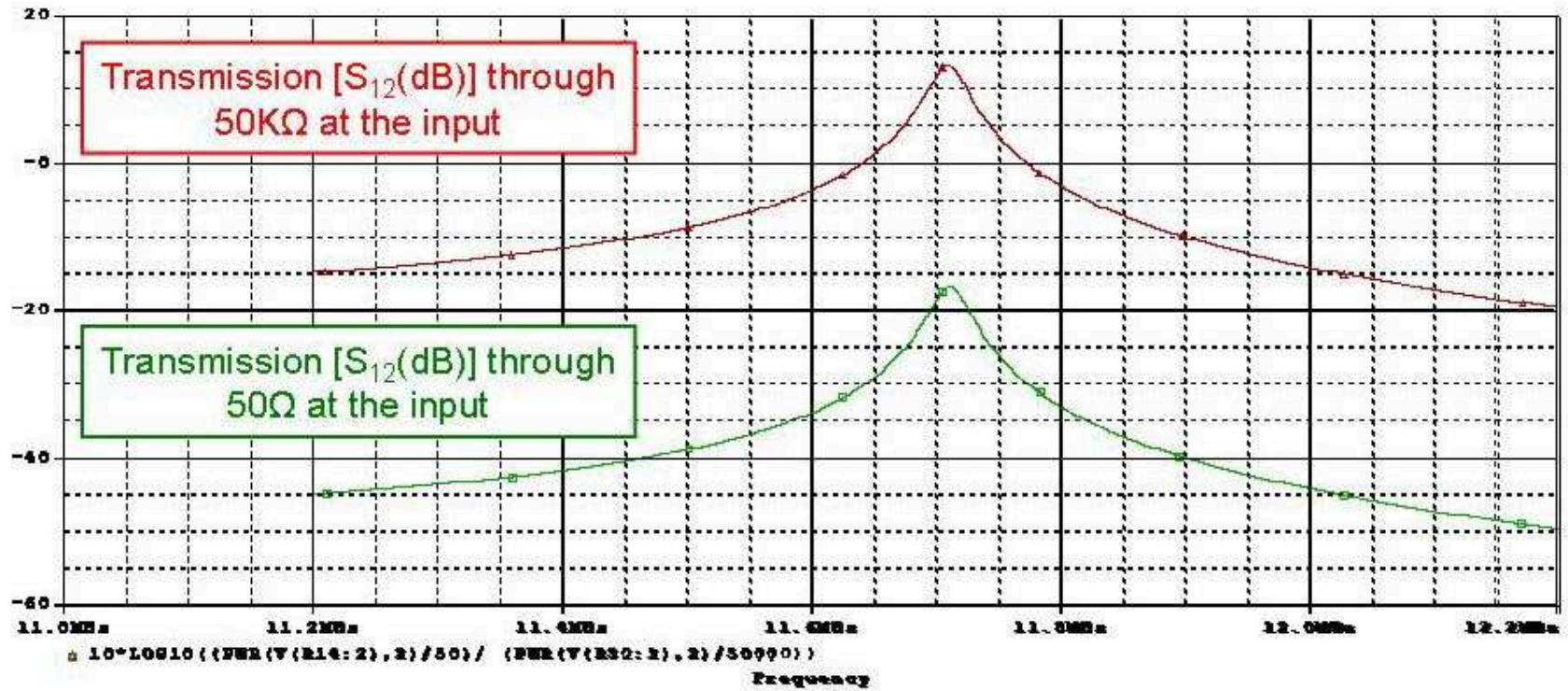
Figure 5.17: PSpice simulation of transmission through the input closed by 50Ω and $50K\Omega$ sources.

It is worth stressing that the previous estimate comes from an oversimplified modeling. A more quantitative evaluation will be given later in this chapter (Section 5.2.5).

Finally, the output gain ($G_p^{meas}(\omega_o) = 25dB$), measured on resonance after MITEQ amplification, was used to determine the *device* power gain ($G_p(\omega_o)$), as the ratio between the power fed into the input circuit (after attenuation) and the device output power, resulting in $G_p(\omega_o) \approx 24dB$. The source, attenuators and fridge line impedances [17] mismatch with the input circuit input impedance [18] accounted for an estimated factor of about $-14dB$ in mismatch power losses.

Data presented in Section 5.3.1 to 5.3.4 show the device response peaked at 11.7 MHz and sensitive to temperature, SQUID bias and power level from both the modulation coil and the input circuit. PSpice simulations have also been used, showing a reasonable agreement with the device behavior when the SQUID was represented by a lumped element transformer. Because of the extreme sensitivity of the device response around 11.7 MHz, the use of Bessel plot signal calibrations at the same frequency was required in the following part of the work for a more quantitative analysis of the data. The next section will analyze the device sensitivity and noise.

---

[17]For a total impedance between 150Ω and 200Ω, depending on the number ($2-3$) of room temperature attenuators used, for which a record was unfortunately not kept.

[18]About $16K\Omega$ around $11.7MHz$ from PSpice simulation.

5.2.5   Device 4.1: sensitivity and noise

Device (4.1) was engineered as a scheme to detect a DC-SET in the shot-noise limit. Supposing a SET with $R_{SET} = 50K\Omega$ and $1nA$ current, it is $\sqrt{S_I} = \sqrt{2eI} \approx 20fA/\sqrt{Hz}$, corresponding to a voltage noise $\sqrt{S_V} = \sqrt{S_I}\text{x}R_{SET} \approx 1nV/\sqrt{Hz}$. This section addresses the following question:

Can the device detect a noise source of $1nV/\sqrt{Hz}$ at its input?

Two calibrated noise sources, both presenting a Nyquist noise of about $1nV/\sqrt{Hz}$, were used to study device (4.1) sensitivity:

- A 50Ω source at $T = T_{room}$

- A $50K\Omega$ source (metal film resistor) at $T = 250mK$

The scheme of the measurements set-up is illustrated in Fig. 5.18 and Fig. 5.19.

The two noise sources were separately connected to the device input circuit in two series of experiments. The 50Ω source was plugged into the input circuit line at room temperature, while the $50K\Omega$ film resistor was put inside a separate Au-plated copper box anchored to the $300mK$ stage of the He_3 fridge. One side of the $50K\Omega$ resistor was grounded to the box and the other soldered to the connecting pin of an SMA connector that was then screwed into the device input circuit connector.

The measurement was performed in the following way: first the SQUID was DC biased at its maximum sensitivity point, then an 11.7MHz calibration voltage signal equivalent to 1-10 mΦ_o was sent into the modulation coil through the bias-tee
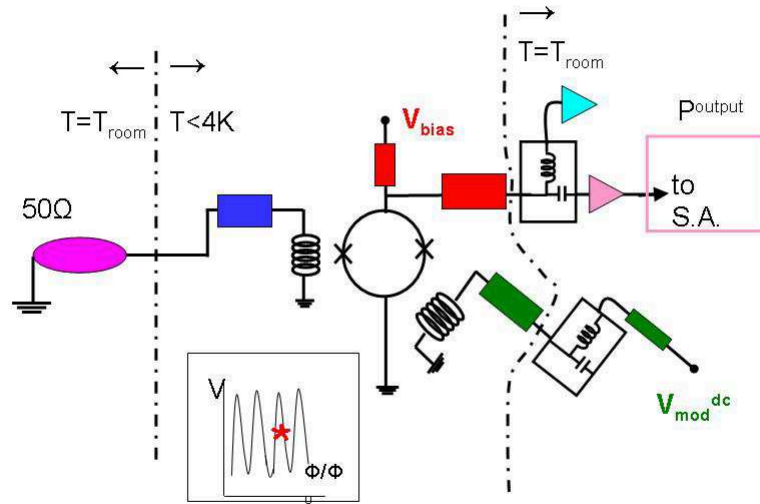
Figure 5.18: Scheme of the noise power measurement of the 50Ω source at $T = T_{room}$, with the SQUID biased at the sensitivity point.

on its line and from a function generator (not shown in Fig. 5.18 and Fig. 5.19), and the sensitivity of the device was optimized by maximizing the signal peak in a narrow-band (4KHz, RBW=10Hz) spectrum by slightly moving the SQUID DC bias point. The function generator was then disconnected, and the device output broadband (1MHz, RBW=100Hz) power spectrum around 11.7MHz was recorded at the output of the RF amplifier for both experimental setups by a Spectrum Analyzer [19] (Fig. 5.20).

To verify that the output power in Fig. 5.20 was sensitive to the $(1nV/\sqrt{Hz})$

---

[19]Agilent 4395A, (10Hz-500MHz Network Analyzer/10Hz-500MHz Spectrum Analyzer/100KHz-500MHz Impedance Analyzer.
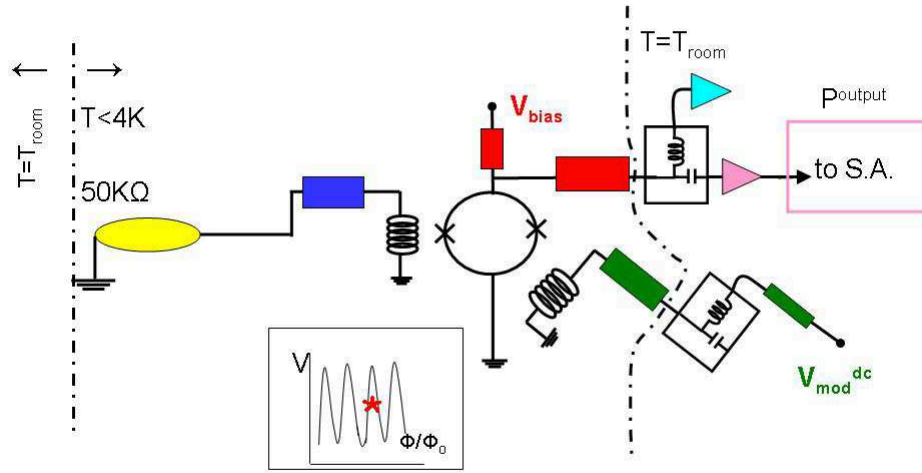
Figure 5.19: Scheme of the noise power measurement of the $50K\Omega$ source at $T = 250mK$, with the SQUID biased at the sensitivity point.

noise signal and not only to the Nyquist noise sources *intrinsic* to the input circuit, the same measurement was repeated with the input circuit shorted [20], as also connected and disconnected [21] to the 50Ω source. Data in Fig. 5.21 show the output power depending on the input circuit configuration and a distinguishable device response to the $1nV/\sqrt{Hz}$ noise source at the input [22].

In order to try to provide a quantitative interpretation of data in Fig. 5.21

---

[20]a short was placed on the input line on top of the fridge

[21]also *floating* in the following

[22]Also, changes in peak frequencies and quality factors were reported: $\nu_o = 11.72MHz$ and $Q \approx 90$ (input closed by 50Ω); $\nu_o = 11.75MHz$ and $Q \approx 37$ (input shorted); $\nu_o = 11.69MHz$ and $Q \approx 80$ (input disconnected from the source).
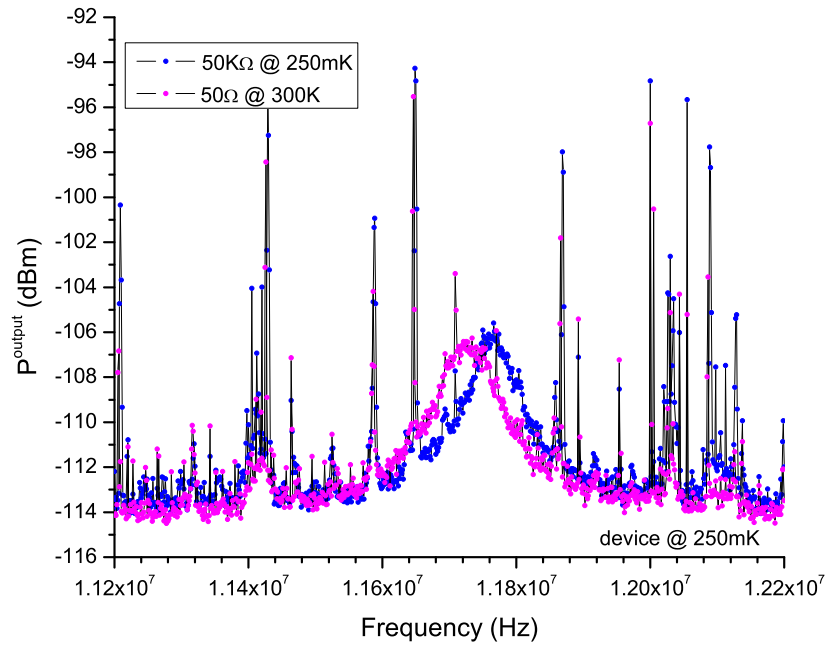
Figure 5.20: Power spectrum at the output of the RF amplifier for device (4.1) with the input circuit closed by 50Ω at $T = T_{room}$ and $50K\Omega$ at $T = 250mK$. The device was at $T = 250mK$.

further data were needed for the same measurement setups. As a tentative comment, the *coupled* input coil impedance (Z_T^* in Section 3.2.1), modified by the different input configurations, together with the screening effect (L^r) of the input circuit seemed to have affected output power level, resonant frequency and resonance width [39].

5.2.5.1 Device power gain (G_p)

Both spectra in Fig. 5.20 show a comparable noise floor and peak noise level, with a shift in frequency of about 40KHz (ν_o=11.76MHz for the input closed by
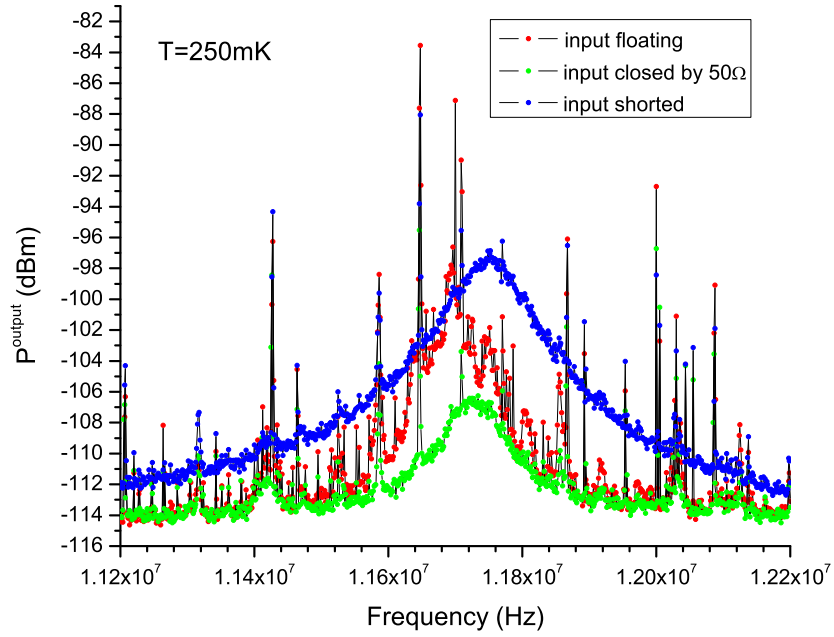
Figure 5.21: Output power spectrum for the input closed by 50Ω at $T = T_{room}$, shorted and disconnected from the source. The device was at $T = 250mK$.

50$K\Omega$, and ν_o=11.72MHz for the input closed by 50Ω) and quality factors Q of about 100 and 90 respectively. While both sources displayed (almost) the same noise power level at the device input, they presented different impedances: as a consequence it was reasonable to expect the SQUID dynamics affected by the diverse impedances connected across the input coil [39], [66], as well as by their unequal matching factors. Information about the device power gain on resonance $(G_p(\omega_o))$ was obtained and confronted also with the gain evaluation determined in Sec. 5.3.4.

1) 50Ω source:

From the $1nV/\sqrt{Hz}$ noise density at the input of the fridge line and the measurement

bandwidth the power level across the 50Ω source was obtained, reduced to half by the fridge line 50Ω impedance acting as a voltage divider, and attenuated by the line $-5.5dB$ attenuation. The *device* output power level was derived from the measurement output power measured at the MITEQ output divided by its power amplification. The impedance mismatch between the fridge line impedance (50Ω) and the input of the input circuit ($\approx 16K\Omega$ [23]) introduced a power mismatch factor $ML = -19dB$. On resonance the detection power gain resulted: $G_p^{scheme}(\omega_o) = 14dB$.

2) $50K\Omega$ source:

The $50K\Omega$ source was plugged directly at the input of the device, so the power gain calculations did not involve the voltage divider nor the known attenuation from the fridge lines. A slight impedance mismatch was nevertheless estimated ($ML = -1.3dB$) between the source and the input circuit impedances, and a detection power gain was obtained of $G_p^{scheme}(\omega_o) = 33dB$, while in the case of optimal matching with the source the device power gain was estimated to be $G_p(\omega_o) = 35.4dB$. Figure 5.22 illustrates the device power gain versus frequency for the detection of a $50K\Omega$ and a 50Ω source.

5.2.5.2   Spectra calibration

In order to get information on the device sensitivity, the power spectrum data needed to be expressed in SQUID flux noise units ($\Phi_o/\sqrt{Hz}$). Calibration was performed on the device with the input closed by $50K\Omega$ in three steps and is described

---

[23]See Section 5.3.4.
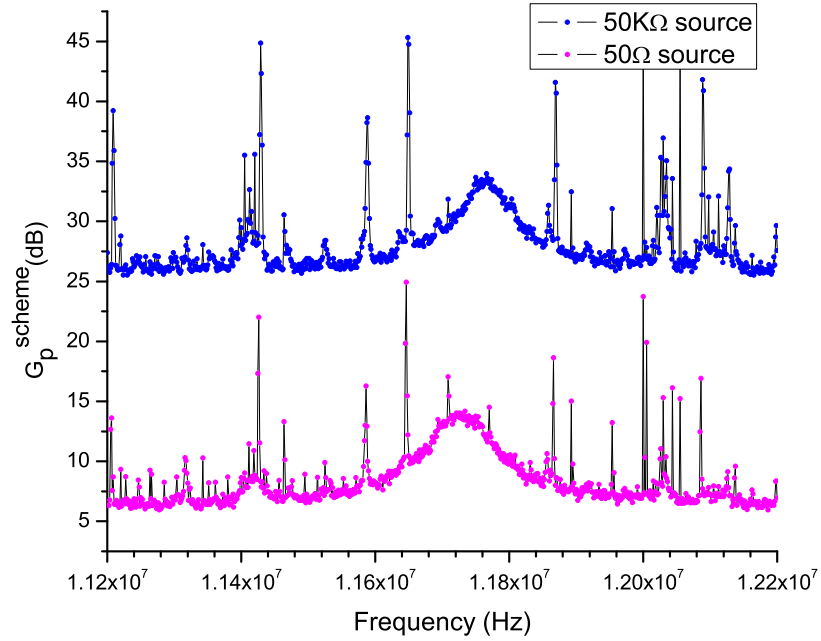
Figure 5.22: Power gain for the detection of a $50K\Omega$ source at $T = 250mK$ and a 50Ω source at $T = T_{room}$. The device was at 250mK.

in the following:

1) A series of Bessel plots was taken using the reference signal calibration setup described in Section 5.2.2, with the device at 250mK and for frequencies $\nu = 5MHz$, $10MHz$ and $11.7MHz$ for comparison (Fig. 5.23) [24].

From the zeros of the fundamental harmonic of the Bessel plot taken at ν=11.7MHz the modulation coil voltage-to-flux transfer function was determined

---

[24]While recording the 11.7MHz data, the RF lock-in phase was incorrectly set, and the maximum output amplitude was measured in the imaginary component channel-and hence here shown in the data.
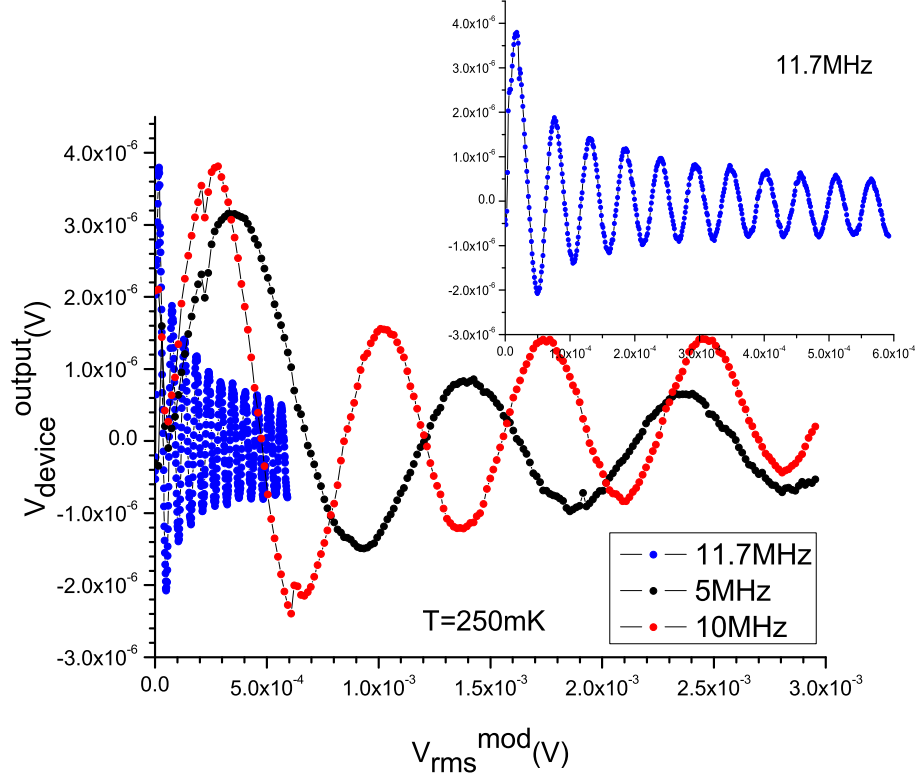
Figure 5.23: Bessel plots for different frequencies (5 MHz; 10 MHz and 11.7 MHz). The device output is shown as function of the rms amplitude applied at the modulation coil. Device at 250 mK and input closed by $50K\Omega$ anchored at the same temperature. Inset: Detail of Bessel plot at ν=11.7 MHz.

to be $(\mathcal{V}_\phi^{mod})_{11.7MHz} \approx 33\mu V_{rms}/\Phi_o$ ($\approx 20mV_{rms}/\Phi_o$ when referred to the signal source). The device output voltage was obtained by dividing the data by the amplification factor of the MITEQ (a factor of 70 in voltage), and it is shown in Fig. 5.23 as function of the rms voltage applied at the modulation coil, obtained after 55.5dB of total attenuation of the source voltage.

2) By keeping the input circuit closed on the cold $50K\Omega$ source, transmission

through the modulation coil was performed at $T = 250mK$, and is shown in Fig. 5.24 for three levels of power (after -85.5 dB of total attenuation).
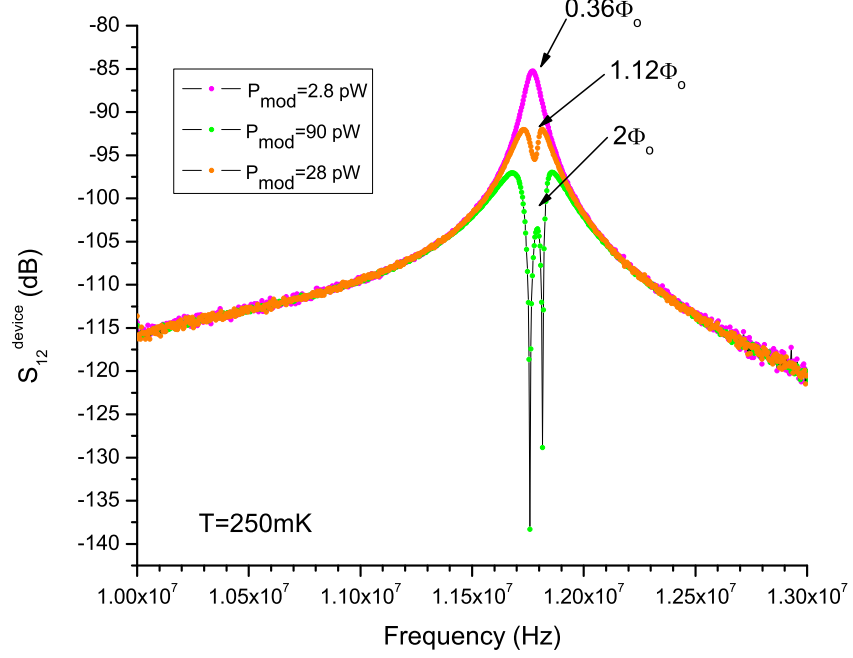
Figure 5.24: Transmission through modulation coil for three power levels (2.8pW, 28pW and 90pW) applied at the modulation coil. Corresponding fluxes generated in the SQUID are also shown as determined from the modulation coil voltage-to-flux transfer function obtained from 11.7 MHz Bessel plot. T=250mK.

By using $(\mathcal{V}_\phi^{mod})_{11.7MHz}(\approx 33\mu V_{rms}/\Phi_o)$ from Bessel plot it was possible to calculate the flux generated in the SQUID at 11.7MHz for each power fed into the modulation coil. In particular it resulted:

$2.8pW \Longrightarrow 0.36\Phi_o$

$28pW \Longrightarrow 1.12\Phi_o$

$90pW \Longrightarrow 2\Phi_o$

As a consequence, since 2.8pW of power into the modulation coil generated in the SQUID about $0.36\Phi_o$ at 11.7MHz, and this produced (from transmission measurement data at the same frequency) a *device* output voltage of about $14\mu V_{rms}$, the device flux-to-voltage transfer function was determined to be $(V_\phi^{device})_{11.7MHz} \approx 39\mu V_{rms}/\Phi_o$. The transfer coefficient so determined resulted to be in reasonable agreement with the one independently assessed from the initial linear slope of the 11.7MHz Bessel plot ($\approx 33\mu V_{rms}/\Phi_o$), being in fact also:

$$\left(V_\phi^{device}\right)_{11.7MHz} = \left(\frac{\partial V_{device}^{output}}{\partial V_{rms}^{mod}}\right) \times \left(\mathcal{V}_\phi^{mod}{}_{11.7MHz}\right). \qquad (5.1)$$

In addition, and as a comparison, $(V_\phi^{device})_{DC}$ was determined from the maximum slope of $V - \Phi$ curves taken at T=250mK and with the input circuit closed by $50K\Omega$, and resulted to be $(45 \pm 2)\mu V/\Phi_o$, in excellent agreement with what determined in Section 5.2.2, but a factor of about 0.2 from the *nominal* $(V_\phi^{SQUID})^{max} = R/L$. The flux-to-voltage transfer coefficient determined at the device operating frequency (11.7MHz) resulted to be about 0.18 times $(V_\phi^{SQUID})^{max}$ as calculated from the SQUID nominal parameters and as determined in Section 5.2.2.

Hilbert and Clarke studies [39] on the effect of the input circuit into SQUID parameters that can affect V_Φ have been reviewed in Section 3.2.1. Although $\Delta V_\Phi/V_\Phi = (0.6 \pm 0.2)$ is reported by the same work [39], with a large systematic relative error related to the uncertainties in the parameters of the unloaded circuit, more study is necessary to understand the origin of the discrepancy for the input circuit configuration of this thesis.

3) Finally, data in Fig. 5.20 were expressed in terms of SQUID flux noise (Fig. 5.25).

Output power measured in dBm was converted into voltage noise at the output of the device $(\sqrt{S_V})^{device}$ after correcting for the output line attenuation (-1.5dB). Then, the *device* flux noise $(\sqrt{S_\Phi})^{device}$ was derived through the transfer coefficient:

$$(\sqrt{S_\Phi})^{device} = \frac{(\sqrt{S_V})^{device}}{(V_\phi^{device})_{11.7MHz}} \tag{5.2}$$

Figure 5.25 shows the device flux noise. The horizontal green line in the plot represents the RF amplifier equivalent flux noise referred to the device output [25].

5.2.5.3   Noise temperature

Noise spectra were analogously recorded after increasing the stage temperature T_{stage} to $500mK$ and $800mK$. Noise power referred to the output of the SQUID was then derived for each stage temperature from the *device* output voltage, divided by the MITEQ gain and the amplifying factor $(Q = 3)$ of the output matching network. Then peaks areas (*integrated noise power*) were obtained from Lorentzian fits of the curves (see inset in Fig. 5.26), to be plotted versus T_{stage} as shown in Fig. 5.26.

In agreement with the equipartition theorem, integrated noise power data showed a linear dependence on stage temperature, with an intercept to the origin within the fit error $[(3 \pm 3)10^7(\mu\Phi_o)^2]$. Furthermore the noise power peaks areas were in the same ratios as the stage temperatures they were referring to, illustrating that the $50K\Omega$ noise source was in thermal equilibrium with the bath

---

[25]$(\sqrt{S_V})^{MITEQ} = 0.3nV/\sqrt{Hz}$ at about 10MHz -as reported in Section 4.4. When referred to the device output $(\sqrt{S_V'})^{MITEQ}$ was estimated to be $\approx 0.4nV/\sqrt{Hz}$.
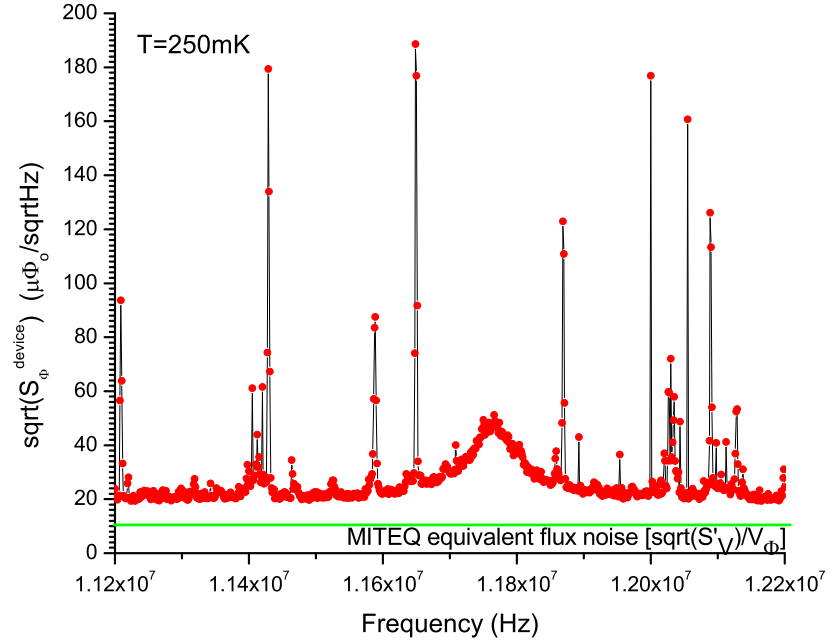
Figure 5.25: Device flux noise (red curve), with cold $50K\Omega$ source at its input. The green line represents the equivalent flux noise of the MITEQ amplifier at the device output.

and allowing to perform noise thermometry. In fact, from the slope of the linear fit $[(5.4 \pm 0.5)10^8 (\mu\Phi_o)^2/K]$ the following temperatures were derived for the $50K\Omega$ source:

$T_{stage} = 0.3K, \Rightarrow T_{source} = (0.30 \pm 0.06)K;$

$T_{stage} = 0.5K, \Rightarrow T_{source} = (0.55 \pm 0.07)K;$

$T_{stage} = 0.8K, \Rightarrow T_{source} = (0.8 \pm 0.1)K.$

Lastly, the noise performance of the detection scheme (referred to the SQUID output) was assessed through the estimate of the device noise temperature T_N, i.e. the temperature for which the rms amplitude of the flux noise would be equal to the

110
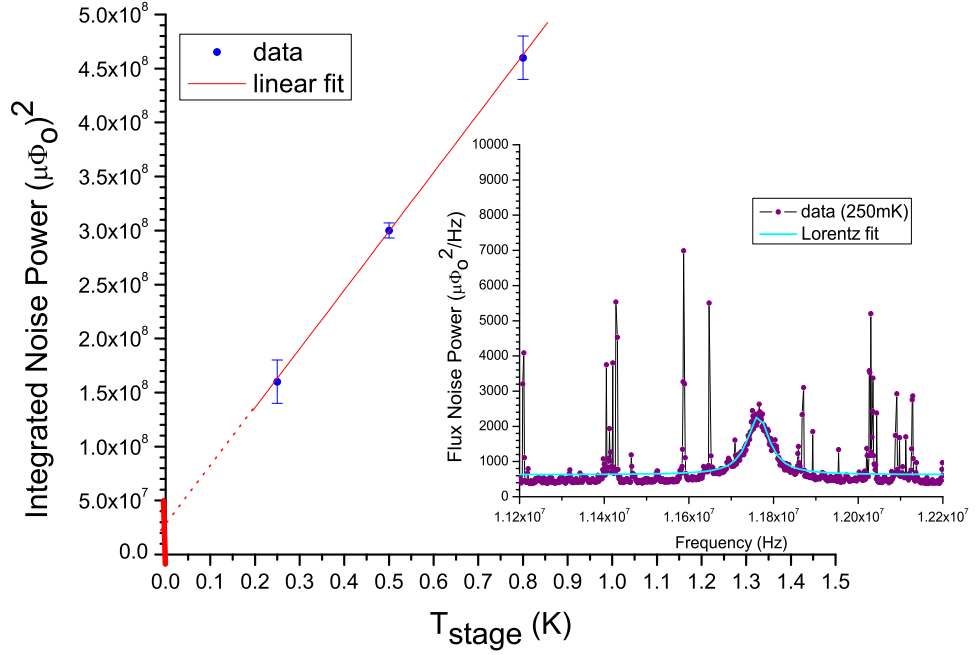
Figure 5.26: Integrated noise power (referred to the output of the SQUID) versus stage temperature. Red line is the linear fit of the data, while the dashed red line is the extrapolation of the fit to illustrate the intercept and its error (red thick sign). Inset: noise power curve (purple dots), and Lorentzian fit (cyan line). T=250mK.

r.m.s. background level. From the Lorentzian fit of flux noise power data taken at $T_{source} = (0.30 \pm 0.06) K$, background and amplitude levels were obtained (Fig. 5.27), and the noise temperature $[T_N = (116 \pm 30) mK]$ derived from the following ratio [23]:

$$T_N = \frac{T_{source} \times (Background)}{(Amplitude)} \qquad (5.3)$$

The derived noise temperature allowed to estimate the detection scheme current sensitivity. As a reference with some recent experiments performed by A. Naik
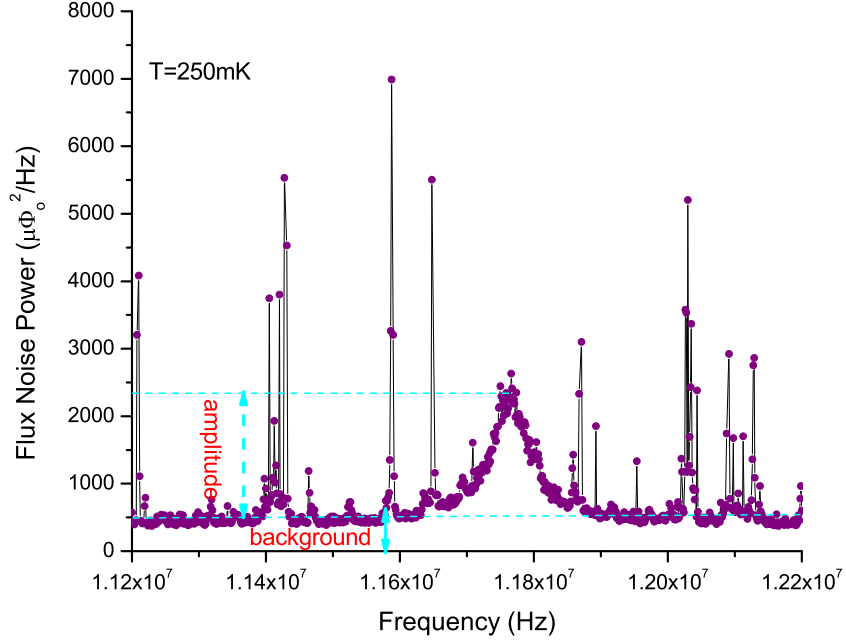
Figure 5.27: Amplitude and background in flux noise power, $50K\Omega$ source at $T_{source} = (0.30 \pm 0.06)K$.

and collaborators in Keith Schwab's Nanomechanics group [25], a current I_{DS} flowing across a SET with $R_{SET} = (104.0 \pm 0.3)K\Omega$ [24] was considered. Thus, by imposing the voltage noise generated by the shot noise across the SET equivalent to the Nyquist noise of R_{SET} placed at the noise temperature T_N it was:

$$\sqrt{S_V} = R_{SET}\sqrt{S_I} = R_{SET}\sqrt{2eI_{DS}} = \sqrt{4k_B T_N R_{SET}} \qquad (5.4)$$

From the previous equation it was $I_{DS} = (0.20 \pm 0.05)nA$. As a consequence, a current noise spectral density could be obtained: $\sqrt{S_I} = \sqrt{2eI_{DS}}$. A current sensitivity of $(8 \pm 1)fA/\sqrt{Hz}$ was determined in correspondence with the noise

temperature $T_N = (116 \pm 30)mK$.

5.3   Understanding the results

Figure 5.25 illustrates the flux noise levels as referred to the output of the device, with the input closed by a $50k\Omega$ source at $T = 250mK$: $\approx 20\mu_o/\sqrt{Hz}$ ($\approx 0.8nV/\sqrt{Hz}$) for the noise floor level, and $\approx 50\mu\Phi_o/\sqrt{Hz}$ ($\approx 1.8nV/\sqrt{Hz}$) at $\nu = 11.7MHz$. The present section addresses the following question:

Were the observed flux noise levels within what is expected from the device engineering? In other words: was the impedance model network correct, and the noise sources as expected?

A series of noise sources -all referred to the device output- was analyzed, and it is introduced in the following together with some estimates:

A. Amplifier noise $(\sqrt{S_V^{MITEQ}})$:

The MITEQ voltage noise referred to the device output was estimated as $\sqrt{S_V^{MITEQ}} = 0.4nV/\sqrt{Hz}$.

B. Intrinsic SQUID noise $(\sqrt{S_\Phi^{SQUID}})$:

Nyquist noise contribution from the shunt resistors $(\sqrt{S_V^{SQUID}} = \sqrt{16k_BTR})$ was estimated for $T = 250mK$ and $R = 9\Omega$ to be about $22pV/\sqrt{Hz}$, then converted into SQUID flux noise by: $\sqrt{S_\Phi^{SQUID}} = \sqrt{S_V^{SQUID}}L/R \approx 0.12\mu\Phi_o/\sqrt{Hz}$, as estimated for a bare, uncoupled SQUID. The SQUID voltage noise could be roughly estimated to

be about $100pV/\sqrt{Hz}$ if referred to the output of the device.

C. Nyquist noise from the equivalent source ($\sqrt{S_V^{source}}$):

Let R''_{source} be the equivalent of the $50K\Omega$ source resistance after double transformation through the networks of the input circuit. This source generates a Nyquist noise, hence a current in the equivalent input circuit generating a flux in the SQUID. After amplification by the quality factor ($Q = 3$) of the output circuit, it was:

$$\sqrt{S_V^{source}} = QM_iV_\Phi^{SQUID}\sqrt{4k_BTR''_{source}}/(R''_{source})$$

with M_i the mutual inductance between the SQUID and the input coul ($\approx 1nH$), and V_Φ^{SQUID} the transfer coefficient referred to the SQUID output ($\approx 13\mu V/\Phi_o$).

D. Backwards noise:

As previously introduced in Chapter 3, current noise in the SQUID couples back to the input circuit generating a flux that in turn generates a current coupling back to the SQUID and producing flux noise.

Although a more accurate assessment of $\sqrt{S_V^B}$ could probably become very complicated, as it involves the total circulating current noise, a first estimate was obtained from the SQUID current noise deriving from the Nyquist noise of its shunt resistors $\sqrt{S_I^{SQUID}} = 2.5pA/\sqrt{Hz}$. It was thus possible to derive the following expression for this process contribution (at resonance, $\omega_o = 2\pi\nu_o$) to the device output voltage noise:

$$\sqrt{S_V^B} = QM_i^2\omega_o\sqrt{S_I^{SQUID}}/R''_{source} \times V_\Phi^{SQUID}.$$

E. Losses in the input and output circuit:

Two additional noise sources needed to be considered together with the level of flux noise they generated in the SQUID. These sources were represented by the losses

in the input and output circuits from the *real* inductors as modeled in Section 5.2.1 (see Fig. 5.5 for reference). In particular, $46.5K\Omega$ at the input circuit and 0.3Ω at the output. Being at the same temperature of the device, the $46.5K\Omega$ resistance at the $10\mu H$ inductor generated a Nyquist noise of about $0.8nV/\sqrt{Hz}$, and the 0.3Ω source at the output circuit about $2pV/\sqrt{Hz}$.

A Pspice model was considered, shown in Fig. 5.28, representing the device input circuit closed on the $50K\Omega$ resistor, as defined from the experimental conditions. A voltage source was connected in series with each source in turn (Fig. 5.28 shows the source attached to the $46.5K\Omega$ resistor), simulating their Nyquist-generated white noise. The PSice model used in this thesis and modeling the SQUID as a linear transformer is valid when the SQUID can be expressed as a passive lumped element. Its use was thus limited in this case to evaluate the current flowing in the input inductor from where, through the mutual inductance coefficient $M_i \approx 1nH$ and the SQUID inductance $L \approx 80pH$, an estimate of the flux in the SQUID was determined.

For the $46.5K\Omega$ source, $\sqrt{S_\Phi^{46.5K\Omega}} \approx 0.06\mu\Phi_o/\sqrt{Hz}$ was found, translating into $\sqrt{S_V^{46.5K\Omega}} \approx 2.3pV/\sqrt{Hz}$ at the device output.

The 0.3Ω was estimated to generate in the SQUID the flux noise $\sqrt{S_\Phi^{0.3\Omega}} \approx 0.7\mu\Phi_o/\sqrt{Hz}$, i.e. $\sqrt{S_V^{0.3\Omega}} \approx 27pV/\sqrt{Hz}$ at the device output.

Subsequently, supposing that the *white* noise sources (A), (B), (C) and (E) contributed to the $0.8nV/\sqrt{Hz}$ noise floor, the value of $R''_{source} = 0.04\Omega$ was found, a reasonable value when compared with the device design (Chapter 3). R''_{source}
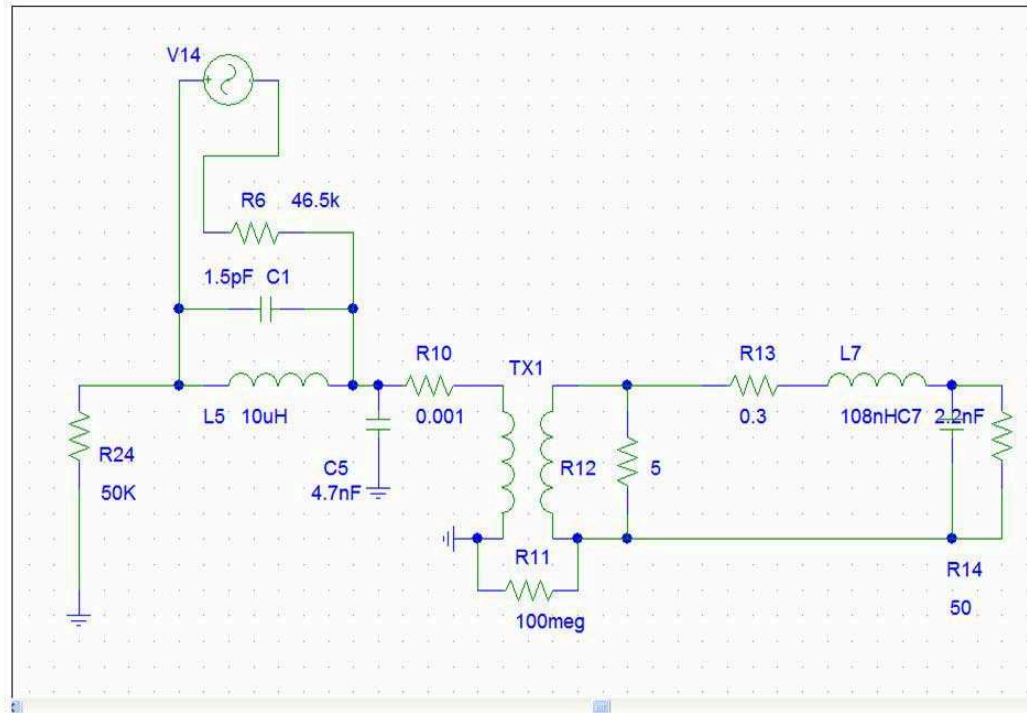
Figure 5.28: PSpice schematic for the evaluation of the contribution of the lossy terms to the measured noise levels.

contributed to the device output voltage of $\sqrt{S_V^{source}} = 0.4nv/\sqrt{Hz}$. Moreover, $\sqrt{S_V^B} = 0.1nV/\sqrt{Hz}$ was determined too.

With $R''_{source} = 0.04\Omega$ and referring to the flux noise level *in* the SQUID, the following numbers resulted:

$$\sqrt{S_\Phi^{SQUID}} \approx 0.12\mu\Phi_o/\sqrt{Hz}$$

$$\sqrt{S_\Phi^{source}} \approx 9.4\mu\Phi_o/\sqrt{Hz}$$

$$\sqrt{S_\Phi^B} \approx 2.3\mu\Phi_o/\sqrt{Hz}$$

Also, a check was performed with the $50K\Omega$ source in PSpice schematic (Fig. 5.28) and a flux of about $4.3\mu\Phi_o/\sqrt{Hz}$ was determined, about half of the previous *approximate*

116

estimates: a reasonable consistency considered the level of approximation involved in separating the different contributions to the flux noise.

5.4   Conclusions and future work

A scheme for the shot noise-limited detection of a DC-biased Single-Electron Transistor was engineered and tested. The device was based on an impedance and noise matching network at the input circuit of a DC-SQUID to match the SET high-impedance $(50 - 100K\Omega)$ source with the low impedance SQUID amplifier. Device transmission and reflection characteristics showed a response at the working frequency which was sensitive to temperature, SQUID bias and flux and was reasonably modeled through a lumped-element circuit and SQUID analysis. Moreover, a $50K\Omega$ source, *simulating* a noise-equivalent $50K\Omega$ SET was detected, and the device noise levels were shown in agreement with that expected from the scheme design. An *approximate* argument showed that the $50K\Omega$ Nyquist noise dominated the other noise sources *intrinsic* to the SQUID and to the device circuitry.

The noise temperature of the detection at the output of the SQUID was derived: $[T_N = (116 \pm 30)mK]$, as well as a current sensitivity of $(8 \pm 1)fA/\sqrt{Hz}$ for the detection of a $100K\Omega$ Single-Electron Transistor.

A further improvement in the device read-out could be achieved through the *flux-to-voltage* transfer coefficient, that was experimentally determined to be $V_\Phi^{device} = 39\mu V/\Phi_o$

when referred to the output of the device [26], to be compared with the *optimum, bare* SQUID value $V_\Phi^{max} = R/L \approx 214 \mu V/\Phi_o$.

As was shown by Hilbert and Clarke [39], the SQUID bias current (for $\Phi/\Phi_o = 1/4$) affects the measured value of the transfer coefficient because of the associated screening of the SQUID inductance: in particular a reduced inductive screening sets at higher currents, $I/I_C > 1$ (the range of bias currents utilized in the present work). Although it is not possible to conclude at present that this is the only cause for the observed dramatic reduction in V_Φ^{SQUID}, future experiments could also include a mapping of the flux-to-voltage coefficient, as derived from Bessel plots and transmission through the modulation coil (Section 5.2.5.2) for different SQUID bias currents, and find the optimal SQUID working point corresponding to the maximum transfer coefficient.

Furthermore, a series of SET devices was realized by Akshay Naik and Jared Hertzberg to be used in the second part of this experiment. SETs were fabricated on Si_3N_4-coated Si wafers following a recipe developed in the Nanomechanics group [24]; their resistances ranged from $70K\Omega$ to $400K\Omega$. As an example, Figure A.1 in Appendix A [27] illustrates one of the samples fabricated by Akshay Naik. Although most of what was needed was already in place to continue the experiment , it was unfortunately not possible to test the detection of at least one of such SETs because of interrupted access privileges to experimental facilities at the Laboratory for Physical Sciences. Attempts to continue this experiment by connecting an SET to the device

---

[26]$V_\Phi^{SQUID} = 13\mu V/\Phi_o$ when referred to the output of the SQUID.

[27]Appendix A describes the SET bias circuit box fabricated and tested for the experiment.

are actively being made at the moment of writing.

Appendix A

SET bias circuit

Figure A.1 illustrates one of the SET devices fabricated by Akshay Naik to be read with the detection scheme described in this work.
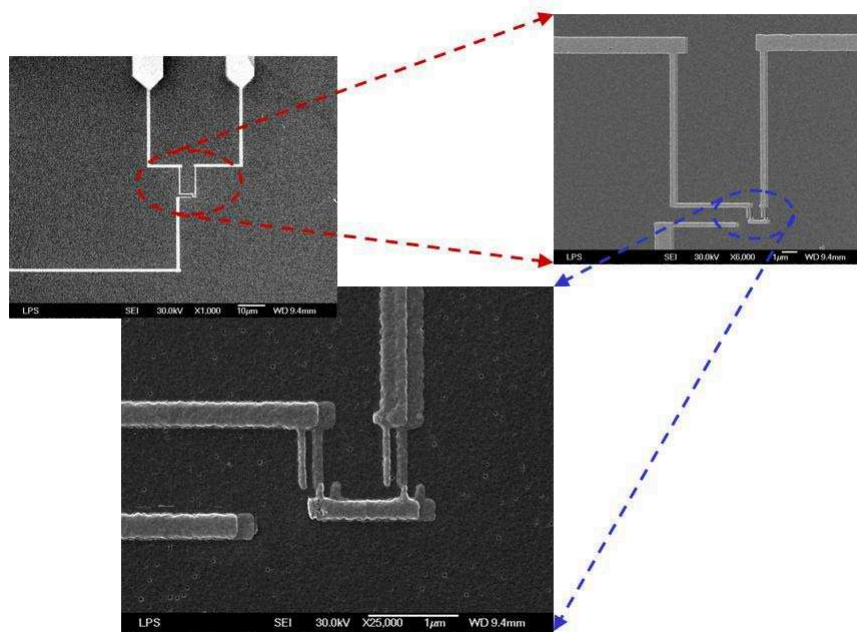
Figure A.1: SEM image of a Single-Electron transistor. Fabrication and image courtesy of Akshay Naik.

In the read-out of a DC-biased Single Electron Transistor the SQUID device-operating at the frequency ω_o- must access only voltage fluctuations related to the SET changes of impedance.

The SET bias circuit was thus designed to resonate at ω_o and present an elevated

equivalent impedance $Z(\omega_o)$ as seen from the SQUID, while maintaining a DC connection to the SET. This was accomplished with an RLC circuit as illustrated in Fig. A.2.
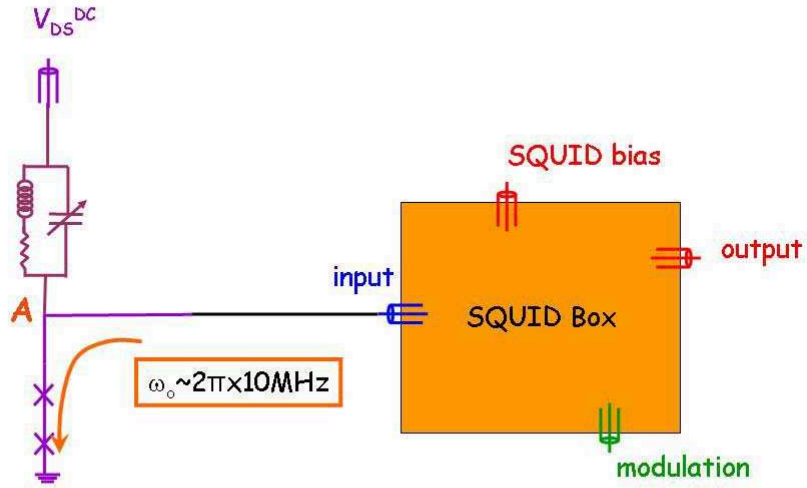
Figure A.2: Schematic of the SET bias and read-out.

The SET bias circuit was designed by fixing $L = 47\mu H$ and $R = 8\Omega$, and by choosing a surface mount trimmable capacitor $(2 - 10pF)$ in order to adjust the resonance of the bias circuit to the device operating frequency at low temperature. The circuit was mounted on a board, enclosed in a Au plated copper box provided with SMA connectors, and its resonance frequency was measured at room temperature through a reflection measurement from a Network Analyzer. Shifts in the resonant frequency were also recorded at $T = 4K$, and a calibration curve of the

resonant frequency at $T = 4K$ (ν_{4K}) *versus* the resonant frequency at $T = 300K$ (ν_{300K}) was obtained, as shown in Fig. A.3, allowing one in the future to tune the room temperature resonant frequency in order to match the device working frequency, once at low temperature.
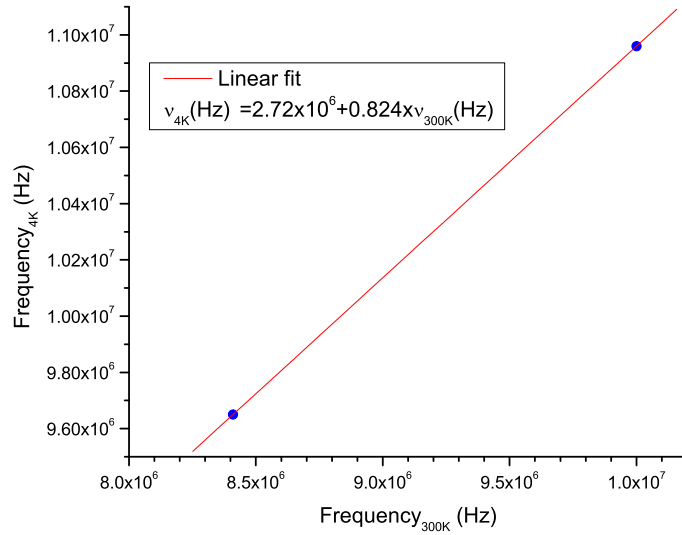
Figure A.3: SET bias circuit calibration curve, ν_{4K} *versus* ν_{300K}.

Appendix B

Characterization and flux noise of an *uncoupled* SQUID

As part of a preliminary assessment, and in order to test the noise of an *uncoupled* SQUID, device (1.0) was built with a 100 turns SQUID [1]. No circuitry was connected to the input inductor, which was kept floating. An output matching circuit was realized with a capacitor $C = 1.6nF$ and an inductor $L = 0.15\mu H$, resonating at about $10MHz$. From the IV data taken at 4K (Fig. B.1), the slope of the high-current curve provided the value of SQUID dynamic resistance in the resistive state: $R_T \approx 4\Omega$, indicating that the SQUID shunt resistors were about 8Ω each, assuming both shunts equal.

At T=4K and with the SQUID current biased slightly above its critical current, the $V - \Phi$ curve was obtained by sending a DC voltage through the modulation coil, and the DC voltage-to-flux transfer coefficient (referred to the source) was obtained $(\mathcal{V}_\phi^{mod})_{DC} = 0.23V/\Phi_o$. At the time these data were taken, no Bessel plot calibration was yet used, and $(\mathcal{V}_\phi^{mod})_{DC}$ was used to calibrate the signal from the modulation coil. The SQUID flux noise measurement at T=4K was performed according to the scheme shown in Fig. B.2 and summarized in the following.

The SQUID was first biased at its maximum sensitivity point along the $V - \Phi$ curve taken at a bias current slightly above its critical current, then a $200mV_{rms}$ amplitude signal at $9.2MHZ$ was sent into the modulation coil circuit from a function

---

[1]From Table 4.1: $L = 116pH$, $L_i = 3.4\mu H$
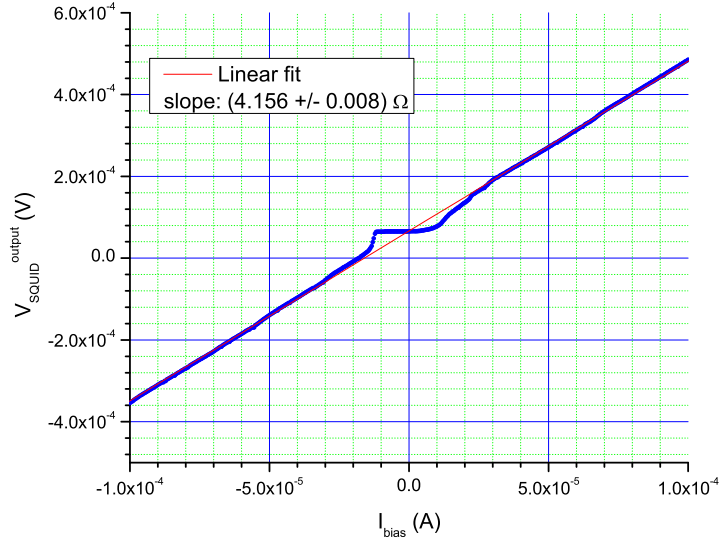
Figure B.1: IV characteristics, T=4K. The red line is the linear fit of the high bias current portion of the data.

generator through $-83dB$ of room temperature attenuators and $-5.5dB$ attenuation from the fridge line. By means of $(\mathcal{V}_\phi^{mod})_{DC}$, it was possible to assess that the signal at the modulation coil generated about $6m\Phi_o$ in the SQUID. Then the SQUID signal was recorded at the output of a room temperature RF amplifier [2] by a spectrum analyzer. First the sensitivity (i.e. the calibrating peak amplitude) was maximized by slightly changing the DC bias points, then a narrowband spectrum $(RBW = 10Hz)$ was recorded around $9.2MHz$. A calibration peak of $-77.5dBm$ was measured at $9.2MHz$, providing $V_\Phi = 154\mu V/\Phi_o$ as transfer coefficient at the output of the de-

---

[2]CLC 425. Analogously to what described in Section 4.2.2, the gain of the amplifier and its voltage noise were measured at T_{room} and $10MHz$, resulting in $G = 30.55dB$ and $\sqrt{S_V} = 0.7nV/\sqrt{Hz}$.
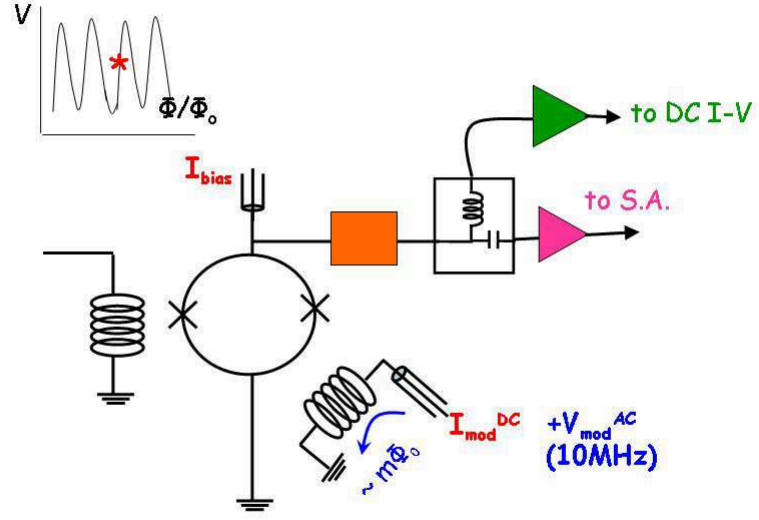
Figure B.2: Scheme of the flux noise measurement for an *uncoupled* SQUID.

vice and before the fridge line attenuation (1.5dB). Then from the spectrum noise floor ($-131dBm$) the voltage noise referred to the input of the amplifier, and accounting for the fridge line (1.5dB) attenuation was derived ($\sqrt{S_V} \approx 0.73nV/\sqrt{Hz}$), resulting in a flux noise $\sqrt{S_{phi}} = 4.7\mu\Phi_o/\sqrt{Hz}$. The flux noise density referred to the input of the amplifier is given by [30]:

$$\sqrt{S_{phi}} = (\sqrt{S_{phi}})^{SQUID} + \frac{(\sqrt{S_V})^{amp}}{V_\Phi} \qquad (B.1)$$

Where:

(a) $(\sqrt{S_{phi}})^{SQUID}$, the intrinsic flux noise of the bare, *uncoupled* SQUID, can be expressed through $\sqrt{16k_BTRL}/R \approx 0.6\mu\Phi_o/\sqrt{Hz}$, with $T = 4K$, $R = 8\Omega$ and

125

$L = 116pH$.

(b): $(\sqrt{S_V})^{amp}$ is the preamplifier voltage noise, dominating the overall flux noise $((\sqrt{S_V})^{amp}/V_\Phi \approx 5\mu\Phi_o/\sqrt{Hz})$.

The output circuit was not optimized to match the SQUID output impedance ($\approx$ few Ohms) with the CLC425 amplifier input impedance ($1K\Omega$), and a mismatch loss of about 11dB was introduced in the circuit portion between the SQUID and the preamplifier.

Assuming a good impedance match was performed, it is possible to estimate the noise temperature of the source (SQUID shunt resistors), and to compare it with the amplifier noise temperature $T_N^{CLC} = 40K$. So, by writing $\sqrt{16k_BTR} = \sqrt{4k_BT_N^{source}R}$, $T_N^{source} = 16K$ could be extracted. The source (SQUID) power level could be read-out by an amplifier such as the CLC425, provided an impedance matching network. For example, it should be possible to match SQUID dynamic output impedance ($\approx fewOhms$) to 50Ω, then send the signal to a $Z_o = 50\Omega$ cable, and match the amplifier $1K\Omega$ impedance into Z_o.

Bibliography

[1] M.H. Devoret and R.J. Schoelkopf "Amplifying quantum signals with the single-electron transistor", Nature **406**, 1039 (2000).

[2] H. Brenning, S. Kafanov, T. Duty, S. Kubatkin and P. Delsing "An ultrasensitive radio-frequency single-electron transistor working up to 4.2K", Journ. Appl. Phys **100**, 114321 (2006).

[3] D. Rogovin and D.J. Scalapino, "Fluctuation phenomena in tunnel junctions", Ann. Phys. (USA), **86(1)**, 1 1974.

[4] L.F. Spietz "The shot noise thermometer", PhD Thesis, Yale University 2006.

[5] S. Kafanov, "The radio frequency single-electron transistor': noise properties and its potential for detecting electrons on Helium", Thesis for the Degree of Licentiate of Engineering, Department of Microtechnology and Nanoscience, Chalmers University of Technology 2006.

[6] W. Schottky, "Electric oscillations", Annalen der Physik, **57**, 541 (1918).

[7] H. Birk, M.J.M. de Jong and C. Schonenberger "Shot-noise suppression in the Single-Electron tunneling regime", Phys. Rev. Lett. **75**, 1610 (1995).

[8] K.A. Matsuoka and K.K. Likharev "Shot noise of single-electron tunneling in one-dimensional arrays", Phys. Rev. B **57**, 15613 (1998).

[9] C. Beenakker and C. Schonenberger "Quantum shot noise. Fluctuations in the flow of electrons signal the transition from particle to wave behavior", Physics Today, May 2003.

[10] A.N. Korotkov "Intrinsic shot noise of the single-electron transistor", Phys. Rev. B **49**, 10381 (1994).

[11] A.N. Korotkov and M.A. Paalanen "Charge sensitivity of radio frequency single-electron transisotr", Appl. Phys. Lett. **74**, 4052 (1999).

[12] A.N. Korotkov, D.V. Averin, K.K. Likharev and S.A. Vasenko "Single-electron transistors as ultrasensitive electrometers", in H. Koch and H. Lubbig (Eds) *Single-electron tunneling and mesoscopic devices*, (Springer-Verlag Berlin Heidelberg 1992).

[13] S. Hershfield, J.H. Davis, P. Hyldgaard, C.J. Stanton and J.W. Wilkins "Zero-frequency current noise for the double-tunnel-junction Coulomb blockade", Phys. Rev. B **42**, 1967 (1993).

[14] M.-S. Choi, F. Plastina and R. Fazio "Shot noise for resonant Cooper Pair tunneling", Phys. Rev. Lett. **87**, 116601-1 (2001).

[15] V.B. Braginsli and F.Ya. Khalili *Quantum Measurement* (Cambridge University Press, 1992).

[16] R.J. Schoelkopf, P. Wahlgren, A.A. Kozhevnikov, P. Delsing and D.E. Prober "The radio-frequency single-electron transisotr (RF-SET): a fast and ultrasensitive electrometer", Science **280**, 1239 (1998).

[17] P. Wahlgren "The radio frequency Single-Electron Transistor and the horizon picture for tunneling", PhD Thesis, Chalmers University of Technology, Goteborg University 1998.

[18] A. Assime, G. Johansson, G. Wendin, R.J. Schoelkopf and P. Delsing "Radio-frequency Single-electron transistor as readout device for qubits: charge sensitivity and backaction", Phys. Rev. Lett. **86**, 3376 (2001).

[19] A. Aassime, D. Gunnarsson, K. Bladh, P. Delsing and R.J. Schoelkopf (Radio-frequency single-electron transistor: toward the shot-noise limit", Appl. Phys. Lett. **79**, 4031 (2001).

[20] L. Roschier, P. Hakonen, K. Bladh, P. Delsing, K.W. Lenhert, L. Spietz and R.J. Schoelkopf "Noise performance of the radio-frequency single-electron transistor", Journ. Appl. Phys. **95**, 1274 (2004).

[21] W.W. Xue, B. Davis, Feng Pan, J. Stetteneheim, T.J. Gilheart and A.J. Rimberg "On-chip matching networks for radio-frequency single-electron transistors", arXiv:0708.1007v1 [cond-mat.mes-hall] 7 Aug. 2007.

[22] M.D. LaHaye, O. Buu, B. Camarota and K.C. Schwab "Approaching the quantum limit of a nanomechanical resonator", Nature **304**, 74 (2004).

[23] M.D. LaHaye "The radio-frequency single-electron transistor displacement detector", PhD Thesis, University of Maryland 2005.

[24] A. Naik "Near quantum limited measurement in nanoelectromechanical systems", PhD Thesis, University of Maryland 2006.

[25] A. Naik, O. Buu, M.D. LaHaye, A.D. Armour, A.A. Clerk, M.P. Blencowe and K.C. Schwab "Cooling a nanomechanical resonator with quantum back-action", Nature **443**, 193 (2006).

[26] M.-O. Andre', M. Muck, J. Clarke, J. Gail and C. Heiden "Radio-frequency amplifier with tenth-kelvin noise temperature based on a microstrip direct current superconducting quantum interference device", Appl. Phys. Lett. 75, 698 (1999).

[27] B.D. Josephson "Possible new effects in superconductive tunneling", Phys. Rev. Lett. **1**, 251 (1962).

[28] B.D. Josephson " Supercurrents through barriers", Adv. Phys. **14**, 419 (1965).

[29] F. London, *Superfluids*, (Wiley New York, 1950).

[30] J. Clarke and Alex I. Braginski (Eds.), *The SQUID Handbook - Vol. I, Fundamentals and Technology of SQUIDs and SQUID systems* (Wiley-VCG, 2006).

[31] M. Tinkham, *Introduction to superconductivity* 2nd edition, (McGraw-Hill Inc.).

[32] J. Clarke "SQUIDs: theory and practice" in H. Weinstock and R.W. Ralston (Eds) *The new Superconducting electronics*, (Kluwer Academic Publishers, 1993).

[33] F.C. Welstood, C. Urbina and J. Clarke "Hot-electron limitation to the sensitivity of the dc superconducting quantum interference device", Appl. Phys. Lett. **54**, 2599 (1989).

[34] F.C. Wellstood, C. Urbina and J. Clarke "Hot-electron effetc in metals", Phys. Rev. B **49**, 5942 (1994).

[35] M.L. Roukes, M.R. Freeman, R.S. Germain and R.C. Richardson "Hot electrons and energy transport in metals at millikelvin temperatures", Phys. Rev. Lett **55**, 422 (1985).

[36] J. Clarke and Alex I. Braginski (Eds.), *The SQUID Handbook - Vol. II, Application of SQUIDs and SQUID Systems* (Wiley-VCG, 2006).

[37] C. Hilbert and J. Clarke "Input impedance of an amplifier based on a dc superconducting quantum interference device", Appl. Phys. Lett. **45**, 799 (1984).

[38] C. Hilbert and J. Clarke "DC SQUID as a tuned radiofrequency amplifier", IEEE Trans. Mag. **MAG-21**, 1029 (1985).

[39] C. Hilbert and J. Clarke "Measurement of the dynamic input impedance of a DC SQUID", J. Low Temp. Phys. **61**, 237 (1985).

[40] C. Hilbert and J. Clarke "DC SQUIDS as radiofrequency amplifiers", J. Low Temp. Phys **61**, 263 (1985).

[41] J. Clarke, C. Tesche and R.P. Giffard "Optimization of dc SQUID voltmeter and magnetometer circuits", J. Low. Temp. Phis. **37**, 405 (1979).

[42] J.M. Martinis and J. Clarke "Signal and noise theory for a DC SQUID amplifier", J. Low Temp. Phys. **61**, 227 (1985).

[43] C.D. Tesche "Optimization of dc SQUID linear amplifiers and the quantum noise limit", Appl. Phys. Lett. **41**, 490 (1982).

[44] C.D. Tesche "Analysis of strong inductive coupling on SQUID systems", IEEE Trans. Mag. **MAG-19**, 458 (1983).

[45] L. Besser and R. Gilmore, *Practical RF Circuit Design for Modern Wireless Systems - Vol. I, Passive Circuits and Systems* (Artech House, Boston, 2003).

[46] R.L. Garwin, US Patent 3,184,674 (May 18, 1965).

[47] P.C. Arnett and D.J. Herrell, IEEE Trans. on Magnetics **MAG-15**, 554 (1979); P.C. Arnett, IEDM Tech. Dig. 485 (1979).

[48] F. Dettmann, W. Richter, G. Albrecht and W. Zahn, Phys. Stat. Sol. (a) **51** K 185 (1979).

[49] T. Ryhanen, H. Seppa and R. Cantor "Effect of parasitic capacitance and inductance on the dynamics and noise of dc superconducting quantum interference devices", J. Appl. Phys. **71**, 6150 (1992).

[50] T. Ryhanen, R. Cantor, D. Drung, H. Koch and H. Seppa "Effect of parasitic capacitance on dc SQUID performance", IEEE Trans. Magn. **27**, 3013 (1990).

[51] H. Seppa, M. Kiviranta, A. Satrapinski, L. Gronberg, J. Salmi and L. Sumi "A coupled dc SQUID with low 1/f noise", IEEE Trans. on Appl. Supercond. **3**, 1816 (1993).

[52] H. Seppa and T. Ryhanen "'Influence of the signal coil on the dc SQUID dynamics"', IEEE Trans. Mag. **MAG-23**, 1083 (1987).

[53] J. Knuutila, M. Kajola, H. Seppa, R. Mutikainen and J. Salmi "'Design, optimization and construction of a dc SQUID with complete flux transformer circuits"', J. Low Temp. Phys. **71**, 369 (1988).

[54] M. Ketchen, D.J. Pearson, K. Stawiatz, C.-K. Hu, A.W. Kleinsasser, T. Brunner, C. Cabral, V. Chandrashekhar, M. Jaso, M. Manny, K. Stein and M. Bhushan "Octagonal washer dc SQUIDs and integrated susceptometers fabricated in a planarized sub-μm Nb-AlO_x-Nb technology", IEEE Trans. on Appl. Supercond. **3**, 1795 (1993).

[55] M.B. Ketchen, K.G. Stawiasz, D.J. Pearson, T.A. Brunner, C.-K. Hu, M.A. Jaso, M.P. Manny, A.A. Parsons and K.J. Stein, "Sub-μm linewidth input coils for low T_c integrated thin-film dc superconducting quantum interference devices", Appl. Phys. Lett. **61**, 336 (1992).

[56] M.B. Ketchen 'Design considerations for DC SQUIDS fabricated in deep submicron technology', IEEE Trans. on Magnetics **27**, 2916 (1991).

[57] V. Foglietti, W.J. Gallagher, M.B. Ketchen, A.W. Kleinsasser, R.H. Koch and R.L. Sandstrom "Performance of dc SQUIDs with resistively shunted inductance", Appl. Phys. Lett. **55**, 1451 (1989).

[58] K. Enpuku, K. Yoshida and S. Kohjiro "Noise characteristics of a dc SQUID with a resistively shunted inductance. II. Optimum damping", J. Appl. Phys. **60**, 4218 (1986.

[59] J.M. Jaycox and M.B. Ketchen 'Planar coupling scheme for ultra low noise DC SQUIDS', IEEE Trans. on Magnetics **MAG-17**, 400 (1981).

[60] M.B. Ketchen and J.M. Jaycox 'Ultra-low-noise tunnel junction dc SQUID with a tightly coupled planar input coil', Appl. Phys. Lett.**40**, 736 (1982).

[61] M.B. Ketchen "DC SQUIDS 1980: the state of the art", IEEE Trans. on Magnetics **MAG-17**, 387 (1981).

[62] Janis model HE-3-SSV User's Manual.

[63] B. Camarota, F. Parage, F. Balestro, P. Delsing and O. Buisson "Experimental evidence of one-dimensional plasma modes in superconducting thin wires", Phys. Rev. Lett. **86**, 480 (2001).

[64] J.M. Martinis, M.H. Devoret, and J. Clarke "'Experimental tests for the quantum behavior of a macroscopic degree of freedom: the phase difference across a Josephson Junction", Phys. Rev. B **35**, 4682 (1987).

[65] W. Banzhaf, *Computer-aided circuit analysis using PSpice* 2nd edition, (Regents/Prentice Hall, 1992).

[66] R.S. Germain, M.L. Roukes, M.R. Freeman, R.C. Richardson and M.B. Ketchen, Physica **126B+C**, 203 (1984).

[67] T.A. Fulton, P.L. Gammel, D.J. Bishop and L.N. Dunkleberger "Observation of combined Josephson and charging effects in small tunnel junction circuits", Phys. Rev. Lett. **63** 1989.

[68] A. Maassen van den Brink, G. Schone and L.J. Geerligs "Combined single-electron and coherent-Cooper-pair tunneling in voltage-biased Josephson junctions", Phys. Rev. Lett. **67**, 3030 (1991).

[69] A.A. Clerk, S.M. Girvin, A.K. Nguyen and A.D. Stone "Resonant Cooper-pair tunneling: Quantum noise and measurement characteristics", Phys. Rev. Lett. **89**, 176804-1 (2002).